Doctoral Thesis

ESCUELA DE DOCTORADO DE LA UNIVERSIDAD DE CANTABRIA
Doctorado en Ingenierías Química de la Energía y de Procesos

Memoria de Tesis Doctoral para optar al título de
Doctora por la Universidad de Cantabria

DESIGN OF TiO_2-BASED MATERIALS FOR PHOTOCATALYTIC ENVIRONMENTAL APPLICATIONS

Diseño de materiales a base de TiO_2 para aplicaciones fotocatalíticas medioambientales

Presentada por:

Paula Ribao Martínez

Dirigida por:

Prof. Dra. Inmaculada Ortiz Uribe
Dra. María José Rivero Martínez

Santander, 2018

UNIVERSIDAD DE CANTABRIA

ESCUELA DE DOCTORADO DE LA UNIVERSIDAD DE CANTABRIA
DOCTORADO EN INGENIERÍAS QUÍMICA DE LA ENERGÍA Y DE PROCESOS

DESIGN OF TiO_2-BASED MATERIALS FOR PHOTOCATALYTIC ENVIRONMENTAL APPLICATIONS

Diseño de materiales a base de TiO_2 para aplicaciones fotocatalíticas medioambientales

Presentada por:

Paula Ribao Martínez

Dirigida por:

Prof. Dra. Inmaculada Ortiz Uribe

Dra. María José Rivero Martínez

Santander, 2018

This thesis was conducted at the Advanced Separation Processes Group in the Department of Chemical and Biomolecular Engineering at the University of Cantabria.

This research was financially supported by the Spanish Ministry of Economy and Competitiveness and the European Regional Development Fund through the projects: CTM2012-33917 “Advanced oxidation technologies for the improvement of landfill leachate treatment”, CTQ2012-31639 “New separation processes with kinetic control based on the use of functionalized materials”, CTM2015-69845-R “New developments in photocatalysis for environmental applications”, and CTQ2015-66078-R “Advanced separation applications. Modeling and experimental validation”. Paula Ribao has benefited from predoctoral research grant from University of Cantabria granted by resolution of January 11, 2016. Moreover, Paula Ribao has received a predoctoral mobility grant for short stays from University of Cantabria granted by resolution of April 27, 2017.

Due to all of these, a warm thanks towards these institutions is extended.

A mi familia

ACKNOLEDGMENTS

Esta Tesis Doctoral se ha llevado a cabo gracias a la inestimable dirección, coordinación y continuo apoyo y confianza de mis directoras de tesis, la Prof. Dra. Inmaculada Ortiz Uribe y la Dra. María José Rivero Martínez. ¡Muchas gracias!

A la Dra. Carmen M. Rangel, por haberme dado la oportunidad de trabajar en su grupo de investigación en el Laboratório Nacional de Energia e Geologia de Lisboa y por toda su dedicación y amabilidad. Obrigado!

Me gustaría agradecer la formación académica recibida por parte de todos los profesores del Departamento de Ingenierías Química y Biomolecular durante todos estos años. Así mismo, quiero dar las gracias al personal de administración y personal técnico del departamento por su continuada ayuda que, sin duda, ha facilitado mi trabajo.

A todos mis compañeros, que me han acompañado en esta etapa siempre animando y haciendo la experiencia más agradable. Especialmente a Ana y a estos 10 años que hemos disfrutado juntas desde que empezamos la carrera. A Gema, Andrés y Lucía porque ha sido una suerte encontrar en el camino amigos como ellos. Y, sin duda, gracias a todos los extraordinarios compañeros de despacho con los que he reído, compartido y disfrutado de cada momento en el laboratorio. Especialmente a Carlos, por nuestras interesantes charlas y divertidos bailes, y a Sara y Olaia, por tanto tiempo compartiendo alegrías.

A todos mis amigos de Ruiloba por ser tan divertidos, compartir tantos momentos y acompañarme desde que tengo recuerdo. A ellas, porque me han hecho aprender que la buena amistad está construida sobre una base sólida de sarcasmo, buen humor y demasiada confianza.

A Alberto, por ser la persona que más me hace reír, por apoyarme, por alegrar todos mis días y ser partícipe de cada uno de los pasos que he dado desde hace ya muchos años.

Finalmente, quiero dar las gracias a toda mi familia, especialmente a mis padres, sin duda los responsables de que esté escribiendo estas palabras. A mis hermanos, por enseñarme, apoyarme y molestarme a partes iguales. A Andrés y Paloma por hacer tan divertidas las comidas familiares. Y al pequeño Jesús que ha llegado para alegrar nuestros días.

A todos, ¡MUCHAS GRACIAS!

TABLE OF CONTENTS

ABSTRACT

Increasing demand and shortage of clean water sources and growing global energy demand have become crucial issues worldwide. Human activities are currently appropriating more than 61% of the proposed planetary boundary for freshwater consumption. In addition, currently the water pollution problem cannot be solved by the natural cleansing cycle or by conventional treatments. On the other hand, 90% of the world's energy supply is derived from fossil fuel, a limited energy source related to greenhouse effect. In this way, hydrogen is brought to the forefront as a potential energy carrier to overcome various issues related to carbon footprint. Therefore, there is urgent need to search for sustainable technologies to meet demands of human beings. Over the last decades, Advanced Oxidation Processes (AOPs) have been attracting a great interest due to their versatility and potential areas of application. Specifically, heterogeneous photocatalytic processes have appeared as a feasible alternative to conventional treatments operating at room temperature and under atmospheric pressure. This technology is defined as a reaction assisted by the presence of semiconductor photocatalyst and a potentially renewable light source. Until now, titanium dioxide (TiO_2) is one of the most promising photocatalyst due to it is highly photoreactive, chemically stable and cost-effective. However, some drawbacks hinder its wider commercial application. Much effort has been devoted to the development of TiO_2 visible-light harvesting photocatalysts with a low rate of charge carrier recombination. Among them, chemical modifications by incorporation of additional components in the TiO_2 will be under discussion within the present thesis, applying the newly synthetized TiO_2-based photocatalysts for dichloroacetic acid (DCA) remediation and hydrogen production.

The first chapter presents an overview of the problems related to water scarcity and pollution and energy crisis. Furthermore, fundamentals of

advanced oxidation process and specifically, heterogeneous photocatalysis are described. Special attention is invested within the chapter in highlighting the advantages and drawbacks of TiO_2 as photocatalyst and the strategies employed to overcome them through improved photocatalyst design within the addition of graphene oxide and noble metals as co-catalysts. Chapter 2 collects and describes chemical reagents, experimental set-ups and procedures, characterization techniques and analytical methods employed along this work. In the third chapter, the research is focused on the optimization of high-performance photocatalysts based on graphene oxide/titanium dioxide (GO/TiO_2) nanocomposites and their characterization for the effective degradation of DCA. In Chapter 4, noble metals (Ag and Pt) have been employed to improve the photocatalytic activity of TiO_2 against DCA oxidation. Moreover, the role of reactive oxygen species (ROS) using these photocatalysts is examined in order to clarify the degradation pathways. With the aim of extending the area of application of TiO_2-based photocatalysts, Chapter 5 collects the results of hydrogen production using synthetic and crude glycerol as feedstock and TiO_2/GO/Pt ternary photocatalysts.

RESUMEN

El aumento de la demanda y la escasez de fuentes de agua limpia junto con la creciente demanda energética se han convertido en un gran problema a nivel mundial. Actualmente las actividades humanas se apropian de más del 61% del agua dulce disponible para el consumo. Además, la problemática asociada a la contaminación de estas aguas no puede resolverse mediante el ciclo de limpieza natural o mediante los tratamientos convencionales. Por otro lado, el 90% del suministro de energía del mundo proviene de combustibles fósiles, una fuente de energía limitada y directamente relacionada con el efecto invernadero. En este sentido, el hidrógeno se presenta como un potencial vector energético con capacidad para superar los diversos problemas relacionados con la huella de carbono. Por lo tanto, existe una necesidad urgente de buscar tecnologías sostenibles para satisfacer las demandas de los seres humanos. En las últimas décadas, los procesos de oxidación avanzada (POAs) han atraído un gran interés debido a su versatilidad y sus amplias áreas de aplicación. Específicamente, la fotocatálisis heterogénea ha surgido como una alternativa factible ya que permite trabajar a temperatura ambiente y presión atmosférica. Esta tecnología se define como una reacción asistida por la presencia de un semiconductor y una fuente de luz potencialmente renovable. Hasta ahora, el dióxido de titanio (TiO_2) es uno de los fotocatalizadores más prometedores debido a que es altamente fotorreactivo, químicamente estable y económicamente rentable. Sin embargo, presenta algunos inconvenientes que dificultan su aplicación comercial. Se han dedicado muchos esfuerzos al desarrollo de fotocatalizadores capaces de trabajar bajo luz visible y con bajas tasas de recombinación de los portadores de carga. Bajo esta premisa, a lo largo de la presente tesis se discutirán diferentes modificaciones del TiO_2 mediante la incorporación de componentes adicionales para la degradación del ácido dicloroacético (DCA) y la producción de hidrógeno.

El primer capítulo aborda una visión general de los problemas relacionados con la escasez y contaminación de agua y la crisis energética. Además, se describen los fundamentos de los procesos de oxidación avanzada y, específicamente, de la fotocatálisis heterogénea. Se presta especial atención dentro del capítulo a las ventajas y desventajas del TiO_2 como fotocatalizador y a las estrategias empleadas para mejorar su actividad mediante el diseño de fotocatalizadores basados en TiO_2 dopado con óxido de grafeno y metales nobles. El Capítulo 2 recopila y describe reactivos químicos, configuraciones y procedimientos experimentales, técnicas de caracterización y métodos analíticos empleados. En el tercer capítulo, la investigación se centra en la optimización y caracterización de fotocatalizadores de alto rendimiento basados en dióxido de titanio/óxido de grafeno (TiO_2/GO) para la degradación efectiva de DCA. En el Capítulo 4, se emplean metales nobles (Ag y Pt) para mejorar la actividad fotocatalítica del TiO_2 en el proceso de oxidación del DCA. Además, se examina el papel de las especies oxigenadas reactivas para aclarar las vías de degradación en función del fotocatalizador empleado. Con el objetivo de ampliar el área de aplicación de los fotocatalizadores basados en TiO_2, el Capítulo 5 recopila los resultados de la producción fotocatalítica de hidrógeno utilizando glicerol sintético y bruto como materia prima y fotocatalizadores ternarios de TiO_2/GO/Pt.

CHAPTER 1

INTRODUCTION

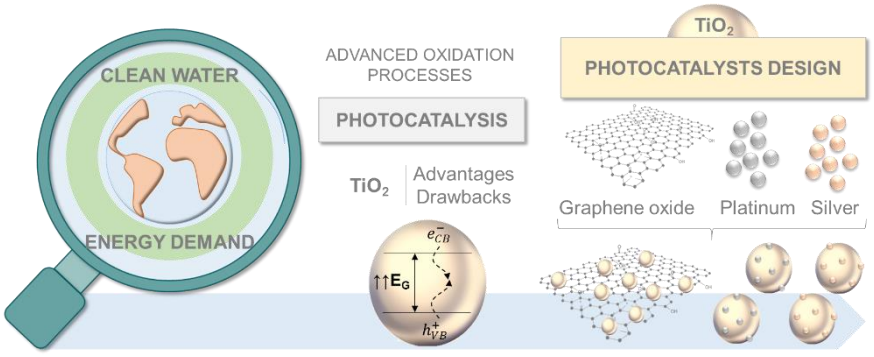

1.1. Water resources

Increasing demand and shortage of clean water sources due to the rapid development of industrialization, population growth, environmental pollution, depleted water resources, long-term droughts, global warming causing abnormal climate changes, and uncontrolled groundwater development have become an issue worldwide. Human activities are currently appropriating more than 61% of the proposed planetary boundary for freshwater consumption, referring to the determined value of water that can be appropriated within a safe operating space for humanity with respect to the functioning of the Earth's system, i.e. without reaching dangerous thresholds that can lead to irreversible damages on water-related ecosystem services. This value amounts around 2800 km^3 $year^{-1}$ of available surface and ground water (Quinteiro *et al*., 2018). Moreover, it is estimated that about 4 billion people worldwide have no or little access to clean and sanitized water supply, and millions of people die of severe waterborne diseases annually (Chong *et al*. 2010). The Intergovernmental Panel on Climate Change (IPCC) reported that unabated climate change has the potential to strongly impact freshwater resources with wide ranging consequences for societies and ecosystems. At present about two-thirds of the global population presently live in conditions of severe water scarcity for at least 1 month of the year and half a billion people face severe water scarcity all year round (Distefano and Kelly, 2017)

Many studies have confirmed that water scarcity will increase significantly over the coming decades and this will bring problems for food security, environmental sustainability, and economic development (Distefano and Kelly, 2017). The rapid development of manufacturing technology after the industrial revolution has improved the standards of living significantly but it is becoming a factor that is threatening human health and the environment. Pollutants are changing both quantitatively and qualitatively, and the number of chemicals currently in circulation can

be estimated in 38000 with more than 300 new materials being synthesized every year due to the diversification of industrial structures and high-tech industry. In line with national development, growth and policy, industrial wastewater is becoming more contaminated and difficult to process. The wide area of water pollution, diversification and non-biodegradability has become a problem that cannot be solved by the natural cleansing cycle (Lee and Park, 2013).

In this context, haloacetic acids (HAAs) have become a major concern for researchers and legislators across the globe as they are the second most important disinfection by-product (DBPs) found in chlorinated drinking waters, after trihalomethanes (Wang *et al*., 2009; Esclapez *et al*., 2012; Aslani *et al*., 2017). During water treatment, chlorine reacts with natural organic matter (NOM) that has not been removed, resulting in the formation of DBPs. Several studies have reported that DBPs may be associated with the occurrence of adverse health effects in humans, including cancer, growth retardation, spontaneous abortion, and congenital cardiac defects (Zhan *et al*., 2010). Among these HAAs, dichloroacetic acid (DCA) has been classified by the US EPA as a probable human carcinogen (group B2), and has a higher concentration in drinking water than other HAAs (Chu *et al*., 2009). Although in Europe the Drinking Water Directive 98/83/EC (DWD) does not currently propose any guideline values for HAAs in drinking water, US EPA drinking water regulations set a maximum contaminant level of 60 μg L^{-1} for five HAAs (trichloroacetic acid (TCAA), dichloroacetic acid (DCA), monochloroacetic acid (MCAA), monobromoacetic acid (MBAA), and dibromoacetic acid (DBAA)) (US EPA, 1998). In addition, Japan's drinking water standards for MCAA, DCA, and TCAA are 20, 40, and 200 μg L^{-1}, respectively (Sakai *et al*., 2013), while in Australia and New Zealand, the regulated limits for drinking water are 150 μg L^{-1} for MCAA, 100 μg L^{-1} for DCAA, and 100 μg L^{-1} for TCAA (Zhang *et al*., 2010).

1.2. Global energy demand

For centuries, humans have powered a growing world by extracting Earth's carbon-rich rocks, peat and liquids and burning them in ever greater amounts, but that trend is beginning to change. A report from the IPCC, suggests that an inevitable shift towards specialized energy crops, sunlight, wind and others renewable energy sources will mark the next four decades. This shift towards renewable energy could reduce cumulative greenhouse gas emissions by 220-560 gigatonnes of carbon dioxide, from a baseline estimate of 1530 gigatonnes (Tollefson, 2011).

Addressing growing global energy demand by environmentally benign and sustainable energy solutions is one of the major challenges of the 21st century. Currently, 90% of the world's energy supply is derived from fossil fuel, a limited energy source (Peng *et al*., 2015). Moreover, CO_2 release is a well-known disadvantage of carbon burning considering this gas the main culprit involved in greenhouse effect. Therefore, clean energy systems are needed to meet the increasing global energy demand with reduced fossil fuel dependence and associated environmental damage. With clean energy systems, it is possible to decrease emissions and waste by taking advantage of energy recovery. Overall, clean energy systems aim to reduce energy input requirements and emissions by taking advantage of sources that are renewable and have less environmental impact (Acar *et al*., 2016).

Hydrogen is brought to the forefront as a potential energy carrier, especially to overcome various issues related to carbon footprint. Hydrogen has the following advantages: (i) good energy conversion effectiveness; (ii) ability to be produced from water with zero emissions; (iii) abundance of sources; (iv) availability of different storage options; (v) transportation over long distances; (vi) high energy content, (vi) possibility to eliminate the environmental harm of the energy sector if hydrogen is produced from renewable energies and water; and (vii) absence of toxic

pollutants, particulates or greenhouse-responsible emissions during its combustion (Kondarides *et al*. 2008; Clarizia *et al*. 2014; Acar *et al*., 2016; Kumar *et al*. 2017). Considering production, storage and combustion, hydrogen fuel with a gross calorific value of 141.8 MJ Kg^{-1} (about 3 times of gasoline), has potential to meet the world's increasing energy demand (Pai *et al*., 2016).

The industrial hydrogen production processes can only start from substances which contain hydrogen since its presence on earth is in combination with other elements. Currently, 95% of hydrogen is obtained from fossil fuels by steam reforming of natural gas, coal or crude oil in an unsustainable process because they are energy intensive (high pressures and temperatures), are based on a non-renewable natural gas feedstock and have a significant carbon footprint (Bahruji *et al*., 2010; Chen *et al*., 2015; Cargnello *et al*., 2016). Only the remaining 5% comes from reforming of biofuels or from electrolysis. Processes involved in H_2 production require large amounts of external energy, since all the reactions producing H_2 (steam reforming, water splitting) are endothermic ($\Delta H > 0$) and endergonic processes ($\Delta G > 0$). Considering the policies of energy saving and emission reduction, hydrogen should be produced from renewable energy (Ma *et al*., 2015). Hence, sustainable H_2 production requires clean primary energy sources, e.g. solar energy, and cheap and available molecules from which the hydrogen is extracted (Beltran *et al*., 2016).

1.3. Advanced Oxidation Processes (AOPs)

Environmental pollution and energy crisis have become two main challenges of the near future. Therefore, there is urgent need to search for clean, renewable, cheap and sustainable technologies as viable alternatives to meet the demands of human beings. In this way, over the last decades, Advanced Oxidation Processes (AOPs) have attracted a great interest due to their success in water and wastewater treatment. The

versatility of AOPs is also enhanced by the fact that they comprise a range of similar but different chemical processes aimed at tackling pollution in water, air and soil, offering different possible processes for reactive oxygen species (ROS) generation, thus allowing a better compliance with the specific treatment requirements. Research concerning AOPs has been immense particularly for two reasons, namely (i) the diversity of technologies involved and (ii) the areas of potential application (Comninellis *et al*., 2008; Cheng *et al*., 2016).

ROS comprehend not only free radicals, such as hydroxyl radical (·OH), superoxide radical ($O_2^{\cdot-}$) and hydroperoxyl radical ($HO_2^{\cdot}$), but also non-radicals such as singlet oxygen ($^1O_2$) and hydrogen peroxide (H_2O_2) (Fernández-Castro *et al*., 2015). As it can be observed in Table 1.1, hydroxyl radical is the most reactive oxidizing agent in water treatment and it is still the specie most commonly tied to the effectiveness of AOPs, with an oxidation potential between 2.8 V (pH 0) and 1.95 V (pH 14). It is very nonselective in its behavior and rapidly reacts with numerous species with rate constants on the order of 10^6 - 10^{10} M^{-1} s^{-1}. Hydroxyl radicals attack organic pollutants through four basic pathways: radical addition, hydrogen abstraction, electron transfer, and radical combination (O'Shea and Dionysiou, 2012; Lee and Park, 2013; Deng and Zhao, 2015). Moreover, ROS have a very short lifetime (10^{-10} s for ·OH) and they are only in situ produced during application through different methods, including a combination of oxidizing agents, irradiation, and catalysts.

Table 1.1 Oxidation potential of some species used in wastewater treatment (Lee and Park, 2013).

Reactive specie	**Potential (eV)**
Hydroxyl radical	2.80
Ozone	2.07
Hydrogen peroxide	1.78
Perhydroxyl radical	1.70
Chlorine dioxide	1.57
Hypochlorous acid	1.49
Oxygen	1.20

AOPs include heterogeneous and homogeneous photocatalysis, Fenton and Fenton-like processes, ozonation, the use of ultrasound, microwaves and ɣ-irradiation, electrochemical processes, wet oxidation processes or even the combination of some of them (Ribeiro *et al*., 2015). One of their main advantages compared to conventional technologies is that they effectively degrade recalcitrant components at room temperature and under atmospheric pressure. In most cases, the formation of secondary waste stream is limited. (Mehmet and Jean-Jacques, 2014; Dewil *et al*., 2017). AOPs can be classified as non-photochemical processes and photochemical processes (Table 1.2).

Table 1.2 Classification of AOPs (Domènech *et al*., 2004).

Non-photochemical processes	**Photochemical processes**
Ozonization in alkaline medium	
Ozonization with H_2O_2	Vacuum-UV photolysis of water
Fenton and related processes	UV/H_2O_2
Electrochemical oxidation	UV/O_3
Radiolysis ɣ and electron beam	Photo-Fenton and related processes
Non-thermal plasma	Heterogeneous photocatalysis
Electrohydraulic discharge - Ultrasound	

Among these AOPs, heterogeneous photocatalysis has attracted increasing attention worldwide for wastewater treatment, air purification, and other applications in the field of environmental remediation, self-cleaning surfaces, green chemistry and green engineering and production of energy and alternative fuels (Dionysiou *et al*., 2016).

1.4. Heterogeneous photocatalysis

Heterogeneous photocatalysis is defined as a reaction assisted by photons in the presence of a semiconductor photocatalyst (Pawar and Lee, 2015). When a semiconductor is irradiated by light with energy matching or greater than its band gap energy (E_g), an electron in an electron-filled valence band (VB) is excited to a vacant conduction band (CB), leaving a positive hole in the VB. These photogenerated electrons and positive holes drive reduction and oxidation, respectively, of different compounds, not necessarily adsorbed on the surface of the photocatalyst. Valence band holes (h^+_{VB}) are powerful oxidants, whereas, conduction band electrons (e^-_{CB}) are reductants (Spasiano *et al*., 2015). The photonic excitation

leaves behind an unfilled valence band, thus creating the electron-hole pair. These charge carriers, with sufficient reductive/oxidative power, can react with the surrounding oxygen-containing species, such as dissolved oxygen (O_2) or H_2O (OH^-), to produce ROS (Figure 1.1) (Chong *et al*., 2010; Lee and Park, 2013; Schneider *et al*., 2014; Wen et al., 2015).

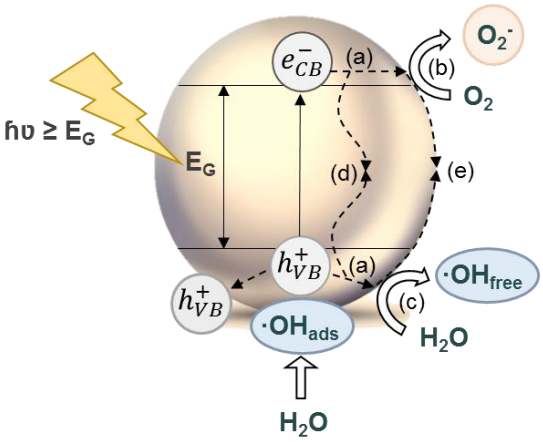

Figure 1.1 Photo-activation of a semiconductor and primary reactions. (a) charge transport in bulk; (b) surface reduction reactions; (c) surface oxidation reactions; (d) charge recombination in bulk, and (e) charge recombination on the surface.

Heterogeneous photocatalysis for wastewater remediation is carried out in presence of dissolved oxygen, generating superoxide radical ($O_2^{\cdot-}$) through the reaction between the surrounded O_2 and e^-_{CB} (1.1). Meanwhile, valence band holes can degrade directly the organic matter or can react with water generating hydroxyl radicals (·OH) that can oxidize the organic pollutants to its corresponding intermediates and further mineralization to carbon dioxide and water (1.2).

Conduction Band

$$e^-_{CB} + O_2 \rightarrow O_2^{\cdot-} \quad (1.1)$$

Valence Band

$$\text{Organic matter} + \left(h^+_{VB}, \cdot OH\right) \rightarrow CO_2 + H_2O \quad (1.2)$$

On the other hand, heterogeneous photocatalysis applied to photo-reforming of biomass to produce hydrogen takes place under unaerated conditions. Therefore, photogenerated electrons are free to reduce H^+ toward H_2 (1.3) and h^+_{VB} (or ·OH radicals) are employed to oxidize the organic compound (1.4).

Conduction Band

$$e^-_{CB} + 2H^+ \rightarrow H_2 \quad (1.3)$$

Valence Band

$$\text{Organic scavenger} + \left(h^+_{VB}, \cdot OH\right) \rightarrow \text{Intermediates} + H^+ \quad (1.4)$$

The electron transfer processes between the semiconductor and surrounding molecules depends on the position of the band gap and redox potential of that molecules. The redox potential of the acceptor molecule is thermodynamically required to be below the CB potential of the semiconductor to accept an electron. Similarly, the redox potential of a donor molecule needs to be above the VB position of the semiconductor in order to donate an electron to the vacant hole. The more positive the valence band, the more oxidizing the valence band holes (Simonsen, 2014). Therefore, photocatalytic reactions over semiconductor are strongly dependent on recombination, trapping, interfacial transfer of charge carriers, and band gap value and position. Selecting an adequate semiconductor is a key issue in photocatalytic processes.

Until now, among various photo-semiconductors (ZnO, WO_3, MoO_3, ZrO_2, SnO_2, etc.), titanium dioxide (TiO_2) is one of the most promising materials due to it is highly photoreactive and cost-effective. Moreover, it presents high chemical stability in a wide pH range, strong resistance to chemical breakdown and photo-corrosion and commercial availability (Chatterjee and Dasgupta, 2005; Kumar and Devi, 2011; Nakata and Fujishima, 2012; Byrne *et al*., 2017).

On the other hand, the possibility of using light as energy source for carrying out chemical reactions may render the process more sustainable due to the drastically increase of selectivity to the required products and the drastically decrease of energy consumption if solar light is employed (Van Gerven *et al*., 2007). The sun is recognized to be the major promising energy source for modern society because it is an inexhaustible natural source with an energy of $3.0 \cdot 10^{24}$ J $year^{-1}$. The world current energy consumption corresponds to about 0.01% of the solar energy reaching the earth's surface. Therefore, the solar energy that reaches the earth exceeds by far the need of the modern society (Nuraje *et al*., 2012).

1.5. Titanium dioxide as photocatalyst

Since Fujishima and co-workers (1972) reported for the first time the photoelectrochemical water splitting on a n-type TiO_2 electrode under ultraviolet (UV) light illumination in 1972, TiO_2 nanomaterials have been extensively applied in various areas. In 1977, titanium dioxide was first employed for environmental remediation reducing CN^- in water (Frank and Bard, 1977). Nanoparticles of TiO_2 were also employed in an efficient dye sensitized solar cell by O'Regan and Grätzel in 1991. Moreover, TiO_2 surfaces presented an excellent anti-fogging and self-cleaning abilities (Wang *et al*., 1997). This led to a dramatic increase in the TiO_2 photocatalysis research due to the potential for water and air purification using solar energy (Pelaez *et al*., 2012; Wen *et al*., 2015).

Titanium dioxide exists as three different polymorphs; anatase, rutile and brookite. In all three forms, titanium (Ti^{4+}) atoms are coordinated to six oxygen (O^{2-}) atoms, forming TiO_6 octahedra. Titanium dioxide is typically an n-type semiconductor due to oxygen deficiency. The band gap is 3.2 eV for anatase, 3.0 eV for rutile, and ~3.2 eV for brookite, being anatase and rutile the main polymorphs. Anatase is the low-temperature stable form and rutile is the dominant form in high temperature preparations. The reduced density of anatase as compared to rutile (3.89 g cm^{-3} versus 4.26 g cm^{-3}) leads to significant differences in many physical properties. The anatase form of titanium dioxide has the desirable properties of being chemically stable, readily available and active as photocatalyst for oxidation processes (Chatterjee and Dasgupta, 2012; Liu *et al*., 2017). The most commercial TiO_2 product is the Aeroxide® P25 (Evonik Industries). It is a nonporous solid with anatase to rutile ratio of 80:20 that absorbs light with wavelengths below 387 nm.

It is commonly agreed that the four-step tandem process must take place for achieving the final interfacial redox reactions of e^-_{CB} and h^+_{VB} over TiO_2: light harvesting, charge generation, charge separation and transport, and surface catalytic reactions. Hence, only the photogenerated charge carriers reaching the surface of TiO_2 can be involved in redox reactions. The possible photoinduced events inside and on the surface of a TiO_2 photocatalyst and the characteristic time for each elementary reaction can be represented by equations (1.5) to (1.11) (Carp *et al*., 2004; Gaya and Abdullah, 2008; Friedmann *et al*., 2010; Spasiano *et al*., 2015; Wen *et al*., 2015):

Charge carrier generation

$TiO_2 + h\upsilon \rightarrow e^-_{CB} + h^+_{VB}$ (fs) (1.5)

Charge-carrier trapping

$h^+_{VB} + >Ti^{IV}OH \rightarrow \{> Ti^{IV} \cdot OH\}^+$ (10 ns) (1.6)

$e^-_{CB} + >Ti^{IV}OH \rightarrow \{> Ti^{III}OH\}$ (100 ps) (1.7)

Charge-carrier recombination

$h^+_{VB} + >Ti^{III}OH \rightarrow >Ti^{IV}OH$ (10 ns) (1.8)

$e^-_{CB} + \{>Ti^{IV} \cdot OH\}^+ \rightarrow Ti^{IV}OH$ (100 ns) (1.9)

Interfacial charge transfer

$\{>Ti^{IV} \cdot OH\}^+ + e^-$ donor $\rightarrow >Ti^{IV}OH$ + Oxid. product (100 ns) (1.10)

$O_2 + \{>Ti^{III}OH\} \rightarrow Ti^{IV}OH + O_2^-$ (ms) (1.11)

The $\{>Ti^{IV} \cdot OH\}^+$ and $\{>Ti^{III}OH\}$ represent the surface-trapped valence band electron and surface-trapped conduction band electrons, respectively (Gaya and Abdullah, 2008).

Therefore, photocatalytic reactions over TiO_2 are strongly dependent on its surface and interfacial properties with recombination, trapping, and interfacial transfer of charge carriers being very fast processes. However, the rate of interfacial charge transfer to surrounding oxygenated species is much slower than the rate of charge recombination in the bulk and on the surface of the catalyst. Therefore, if the interfacial charge transfer rates are not greatly improved, the recombination of interfacial charges proceeds rapidly. In this way, improving the surface reaction kinetics is essential for suppressing the fast surface recombination of charge carriers (Wen *et al*., 2015). Accordingly, charge carrier movements and the photocatalytic activity of TiO_2 can be improved by employing strategies that prevent bulk

and surface charge recombination and enhance charge transport to the surface sites of TiO_2.

Another drawback of TiO_2, which currently limits its wider commercial application, is that it only absorbs in the ultraviolet region, which represents only about 4-8% of the solar energy reaching the earth's surface (Gómez-Pastora *et al*., 2016). Much effort has been devoted to the development of TiO_2 visible-light harvesting photocatalysts to increase the amount of visible sunlight which TiO_2 can absorb.

Some strategies can be adhered to overcome these problems: decreasing the defect sites in the bulk and on the surface, increasing the accessible surface area, loading a co-catalyst, and constructing heterojunctions and nanostructured photocatalysts.

1.6. TiO_2-based photocatalysts

Various strategies have been adopted for improving the photocatalytic efficiency of TiO_2. They can be summarized as either morphological modifications, such as increasing surface area and porosity, or as surface modifications, such as loading co-catalysts, construction of heterojunctions or dye sensitization (Kumar and Devi, 2011; Daghrir *et al*., 2012; Marschall, 2014; Fang *et al*., 2017).

Many studies have focused on modifying the morphology of TiO_2 in order to improve its photocatalytic activity. TiO_2 can exist in a range of morphologies: zero-dimensional spheres, one-dimensional fibers and tubes, two-dimensional nanosheets and three-dimensional with interconnected architectures. Advantages of such structures is their tailored morphology, controlled porosity and low recombination grain boundaries. On the other hand, optimizing the size and shape of TiO_2 particles can maximize the photocatalytic activity, increasing the active surface area (Pelaez *et al*., 2012; Lee and Park, 2013). Finally, it has been

demonstrated that modifications in crystal structure of TiO_2 can play a significant role in charge separation during photocatalytic processes (Chen *et al*., 2010).

Surface modifications are often necessary to enhance charge carrier separation and visible light absorption to improve the photocatalytic activity. Based on the photocatalytic mechanism, several surface modifications strategies can be proposed to design high activity TiO_2 photocatalysts: non-metal doping, metal deposition, dye sensitization, semiconductors coupling and carbon-based structuring.

Non-metal doping of TiO_2 has shown to be a great alternative for photocatalytic environmental applications, being nitrogen the most promising dopant. Moreover, the doping of other non-metal species, such as F, S, P, B and C has also been widely investigated to further increase the activity and stability of TiO_2 nanomaterials. Fluorine doping does not shift the TiO_2 band gap; however it improves the charge separation. Carbon, phosphorous and sulphur as dopants have also shown positive results for visible light activity in TiO_2 and for increasing the lifetime of photogenerated charges.

Regarding to modifications of TiO_2 by metal deposition, transition metals such as Cr, Co, V and Fe have well extended the spectral response of TiO_2 into the visible region also improving the photocatalytic activity. However, transition metals have also been found to cause possible limitations due to photocorrosion, charge recombination at metal sites, and block reaction sites by metals remaining on the TiO_2 surface.

Another very interesting strategy for improving the TiO_2 photocatalytic activity is to deposit noble metals nanoparticles, such as Ag, Au, Pt and Pd on the surface of TiO_2. They have been reported to greatly enhance photocatalytic efficiency, even under visible light, by acting as an electron trap, promoting interfacial charge transfer and therefore delaying recombination of the electron-hole pair.

Dye photosensitization has been also reported as a possible way to extend the photoresponse of TiO_2 into the visible region. The mechanism of the dye sensitized photo-degradation of pollutants is based on the absorption of visible light for exciting an electron of a dye. Subsequently, electrons are transferred into the conduction band of TiO_2 that acts only as a mediator for transferring electrons, remaining the valence band unaffected.

The semiconductor combination approach has been shown to be another effective method for improving TiO_2 photocatalytic activity through better photogenerated charge separation with a formation of a heterojunction structure.

Finally, the junctions between TiO_2 and nanocarbon materials have attracted much attention owing to their superior photocatalytic performance. For instance, composites based on TiO_2 and conductive carbon nanotubes (CNT), carbon nanofibers, fullerene, graphene, and activated carbon have been extensively fabricated to efficiently enhance the photocatalytic activity for various applications. Carbon materials are considered to be suitable as support for TiO_2 owing to their excellent thermal, optical, mechanical and electrical characteristics, resulting in rapid charge transfer on hybrid TiO_2/carbon composites (Chen *et al*., 2010; Leary and Westwood, 2011; Pelaez *et al*., 2012; Lee and Park, 2013; Marschall, 2014; Wen *et al*., 2015).

In this work, due to the high availability and cost-effective properties of commercial TiO_2 (Aeroxide® P25), it was selected as starting material for further developments in the photocatalytic field. Two interesting strategies for the extraction of photoexcited electrons from the TiO_2 to reduce charge carrier recombination probability and extend the excitation wavelength to visible light range are the synthesis of composites with graphene oxide-based nanoassemblies, and the decoration of TiO_2 with noble metal nanoparticles.

1.6.1. Graphene oxide-based TiO_2

Ever since its discovery in 2004, graphene has been making a profound impact in many areas of science and technology due to its remarkable physicochemical properties. They include a high specific surface area (theoretically 2630 m^2 g^{-1} for single-layer graphene), extraordinary electronic properties and electron transport capabilities, unprecedented pliability and impermeability, strong mechanical strength and excellent thermal and electrical conductivities (Chen *et al*., 2012; Julkapli and Bagheri, 2015).

Graphene oxide (GO) has recently emerged as one of the most promising candidates for the development of photo-efficient composite photocatalysts. It is a single-atom-thick sheet arranged by localized sp^3 defects within the sp^2-bonded carbon atoms in a hexagonal lattice with two-dimensional planar sheets (Jiang *et al*., 2013). On a simple level, GO can be considered as consisting of individual sheets of graphene decorated with oxygen functional groups on both the basal planes and edges (Chen *et al*., 2012). GO can be prepared from natural graphite by the modified Hummers' method (Hummer and Hoffeman, 1954) that is the most suitable method for low-cost and large-scale production. The oxygen is bound to the carbon in the form of hydroxyl, epoxy and some carbonyl functional groups in GO nanosheets, which allows for easy dispersion of GO in water and various organic solvents (Zhang *et al*., 2012). This makes GO a useful material for many applications. It is used as adsorbent for wastewater treatment (Kyzas *et al*., 2014), fabrication of microcircuits and sensors and biomedical applications such as drug delivery or tissue engineering and can be also used for therapeutic applications (Perrozzi *et al*., 2015). Furthermore, GO/reduced GO (rGO) systems are used as supercapacitors and/or ultracapacitors. Therefore, graphene and GO have multiple applications in different sectors ranging from conductive ink to chemical

sensors, light emitting devices, composites, energy, touch panels and high frequency electronics (Ferrari *et al*., 2015).

GO was found to be amenable to additional functionalization, and could easily react with TiO_2 and be reduced to conductive graphene (Ng *et al*., 2011). According to the literature, composites of TiO_2 with graphene-based nanosheets can be prepared by different methods: simple mixing and/or sonication, sol-gel process, liquid-phase deposition, hydrothermal and solvothermal methods (Morales-Torres *et al*., 2012). The coupling of TiO_2 and GO nanosheets presumably presents four advantages in terms of photocatalytic activity: (i) GO can trap and move charge carriers, thus avoiding recombination of the electron-hole pairs; (ii) the composite can be easily recovered from aqueous solution due to the large GO sheets; (iii) the new composite provides an adequate quality and quantity of active sites, and (iv) band-gap tuning and/or extension of the excitation wavelength can be achieved (Leary and Westwood, 2011). This last point may be due to the creation of a hybrid orbital just below the conduction band of TiO_2 that enhances the utilization of visible light (Jia *et al*., 2016).

1.6.2. Noble metals-doped TiO_2

Noble metal (NM) nanoparticles, such as Pt and Ag, are usually used as co-catalyst over the TiO_2, promoting the activity by the separation of charge pairs due to the Schotky barrier formation and the localized surface plasmon resonance (LSPR) effect (Fang *et al*., 2017; Bai *et al*., 2015).

Thus far, use of a Schottky junction has been recognized as the most well established strategy for steering the flow of the carriers that are photogenerated in semiconductor (Figure 1.2). It is well known that noble metals can serve as a sink for the photogenerated electrons when forming a Schottky junction with TiO_2 (Bai *et al*., 2015). When the TiO_2 and noble metal nanoparticles are in contact, the photogenerated electrons are

distributed between TiO_2 and metal nanoparticles. The transfer of electrons from the semiconductor to the metal continues until the semiconductor-metal system attains equilibrium. The electron accumulation on the metal deposits shifts the Fermi level of the metal to more negative potentials, and the resultant Fermi level of the composite shifts closer to the CB of the TiO_2. The negative shift in the Fermi level is an indication of better charge separation and more reductive power of the composite system (Kumar and Devi, 2011). The Schottky barrier can serve as an effective electron trap where the electron is unable to flow back to the semiconductor. This makes the metal act as an electron sink for the photo-induced electron. As Schottky barrier prevents the recombination of the electron-hole, it prolongs the lifetime of the electron-hole pair for the photoreactions (Khan *et al*., 2015).

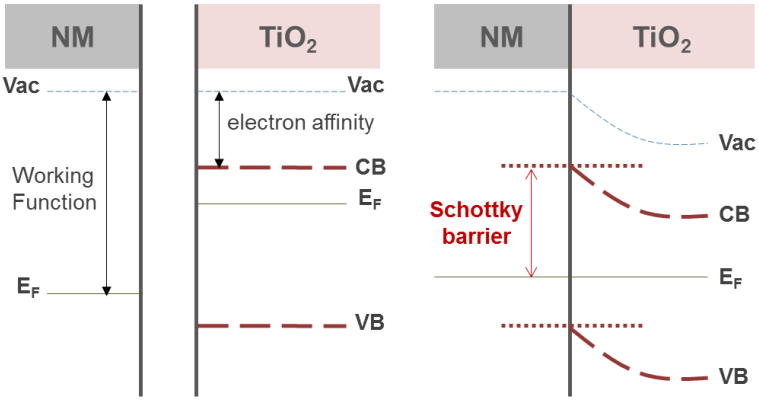

Figure 1.2 Schottky barrier formation between TiO_2 and noble metal (NM).

LSPR refers to the coherent collective oscillation of free electrons in plasmonic metal nanoparticles in response to an external oscillating electric field, such as solar irradiation in the case of photocatalysis. Specifically, the electron cloud tends to be distributed asymmetrically in the proximity of plasmonic nanoparticles within an external oscillating electric field. Consequently, an electric field, which is in the opposite direction to the external electric field, is also created owing to the redistribution of the

charge density. Such oscillations and the established electric field are referred to as localized surface plasmons (Hou and Cronin, 2013; Zhang *et al*., 2015). There are three primary mechanisms that have been identified so far, on how this resonance can help in the photoreaction: (i) the scattering of resonant photons by the metal; (ii) the existence of an intense oscillating electric field around the metal, called Plasmon Resonance Energy Transfer (PRET), and (iii) the production of hot electron-holes in the metal (Figure 1.3). When light is illuminated onto the plasmonic nanometal, the metal is able to spread out incident resonant photons, causing the photons to have longer optical path lengths to travel around the semiconductor and leading to a higher rate of formation of charge carriers in the semiconductor. PRET is another mechanism used to explain the photoreaction via the existence of the intense oscillating electric field around the metal. According to PRET, the energy is transferred from the plasmon to the TiO_2 via the electric field and this electric field will promote the rate of formation of electrons and holes. The third mechanism is the production of hot electron-holes on the metal. According to this mechanism, the noble metal is able to supply the electron to TiO_2 conduction band for further reactions (Khan *et al*., 2015; Zhang *et al*., 2015).

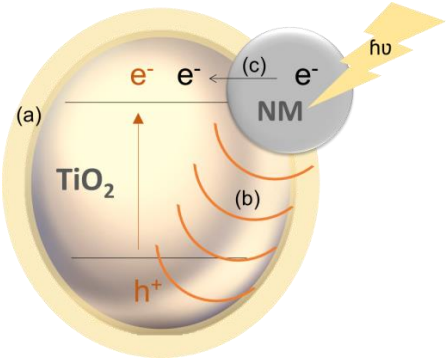

Figure 1.3 Schematic illustration of the three mechanisms for the enhancement effect of plasmonic materials: (a) photon scattering; (b) PRET effect, and (c) hot-electron transfer.

Summary, graphene is selected as a two-dimensional material due to its high electron mobility (15000 $m^2 V^{-1} s^{-1}$) at room temperature, meaning that it acts as an ideal electron sink and electron transfer bridge. Moreover, TiO_2/GO photocatalysts can extend the absorption wavelength to the visible region due to Ti-O-C bonds. On the other hand, platinum and silver nanoparticles have been selected for deepening in their role as TiO_2 dopants. Deposition of Pt on TiO_2 surface is thought to enhance charge carrier separation since Pt serves as an electron trap forming a charge-transfer complex between Pt and TiO_2. Furthermore, Ag noble metal nanoparticles are presented as promising candidates due to the high optical activity manifested in the light-induced excitation of localized surface plasmon resonance (LSPR).

1.7. Framework and objective of the thesis

This work focuses on the design, synthesis and characterization of TiO_2-based materials for DCA aqueous solutions removal and hydrogen production from a renewable source. With this aim, two materials have been selected for improving the limited photocatalytic activity of commercial TiO_2 (P25) i) graphene oxide and ii) noble metals nanoparticles (Pt and Ag) (Figure 1.4).

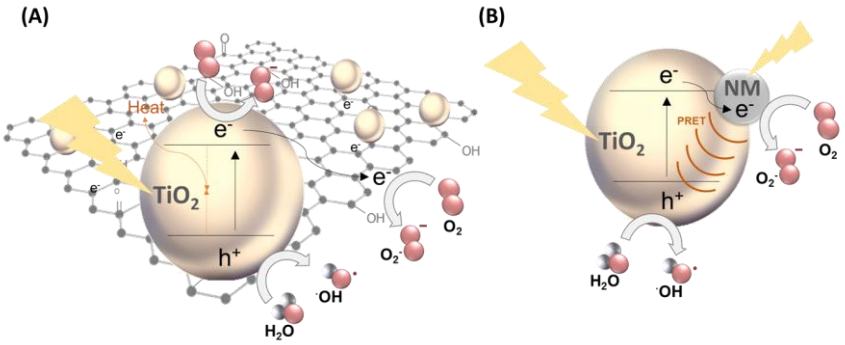

Figure 1.4 Strategies for avoiding electron-hole pair recombination and harvesting visible light incorporating (A) graphene oxide and (B) noble metals.

In this context, three scenarios have been assessed for the development of new photocatalysts:

- Graphene oxide nanosheets can improve the photocatalytic activity of TiO_2 due to its ability to trap and move charge carriers and extend the light absorption to visible range of the solar spectrum.
- Noble metals promoting the photocatalytic activity by the separation of electron-hole pairs due to the Schotky barrier formation and the possibility of interact with solar light due to the localized surface plasmon resonance (LSPR) effect.
- Ternary photocatalysts based on TiO_2, graphene oxide and noble metals present a synergetic effect between the positive characteristics of each component, promoting the transitive property of electrons so as to inhibit the recombination of photogenerated electron-hole pair.

1.8. References

Acar, C., Dincer, I., Naterer, G.F. (2016) Review of photocatalytic water-splitting methods for sustainable hydrogen production. International Journal of Energy Research 40:1449-1473.

Aslani, H., Nasseri, S., Nabizadeh, R., Mesdaghinia, A., Alimohammadi, M., Nazmara, S. (2017) Haloacetic acids degradation by an efficient Ferrate/UV process: Byproduct analysis, kinetic study, and application of response surface methodology for modeling and optimization. Journal of Environmental Management 203:218-228.

Bahruji, H., Bowker, M., Davies, P.R., Al-Mazroai, L.S., Dickinson,A., Greaves, J., James, D., Millard, L., Pedrono, F. (2010) Sustainable H_2 gas production by photocatalysis. Journal of Photochemistry and Photobiology A: Chemistry 216:115-118.

Bai, S., Li, X., Kong, Q., Long, R., Wang, C., Jiang, J., Xiong, Y. (2017) Toward enhanced photocatalytic oxygen evolution: synergetic utilization of plasmonic effect and schottky junction via interfacing facet selection. Advanced Materials 27:3444-3452.

Beltran, A., Romero-Ocaña, I., Delgado Jaen, J.J., Montini, T., Fornasiero, P. (2016) Photocatalytic valorization of ethanol and glycerol over TiO_2 polymorphs for sustainable hydrogen production. Applied Catalysis A: General 518:167-175.

Byrne, C., Subramanian, G., Pillai, S.C (2017) Recent advances in photocatalysis for environmental applications. Journal of Environmental Chemical Engineering. Article in press. Doi: 10.1016/j.jece.2017.07.080.

Cargnello M., Montini,T., Smolin, S.Y., Priebe, J.B., Delgado Jaén, J.J., Doan-Nguyen, V.V.T., McKay, I.S., Schwalbe, J.A., Pohl, M.M., Gordon, T.R., Lu, Y., Baxter, J.B., Brückner, A., Fornasiero, P., Murray, C.B. (2016) Engineering titania nanostructure to tune and improve its photocatalytic activity. Proceedings of the National Academy of Sciences 113:3966-3971.

Carp, O., Huisman, C.L., Reller, A. (2004) Photoinduced reactivity of titanium dioxide. Progress in Solid State Chemistry 32:33-177.

Chatterjee, D., Dasgupta, S. (2005) Visible light induced photocatalytic degradation of organic pollutants. Journal of Photochemistry and Photobiology C: Photochemistry Reviews 6:186-205.

Chen, D., Feng, H., Li, J. (2012) Graphene oxide: preparation, functionalization, and electrochemical applications. Chemical Reviews 112: 6027-6053.

Chen, W.T., Chan, A., Al-Azri, Z.H.N., Dosado, A.G., Nadeem, N.A., Sun-Waterhouse, D., Idriss, H., Waterhouse, G.I.N. (2015) Effect of TiO_2 polymorph and alcohol sacrificial agent on the activity of Au/TiO_2 photocatalysts for H_2 production in alcohol-water mixtures. Journal of Catalysis 329:499-513.

Chen, X., Shen, S., Guo, L., Mao S.S. (2010) Semiconductor-based photocatalytic hydrogen generation. Chemical Reviews 110:6503-6570.

Cheng, M., Zeng, G., Huang, D., Lai, C., Xu, P., Zhang, C., Liu, Y. (2016) Hydroxyl radicals based advanced oxidation processes (AOPs) for remediation of soils contaminated with organic compounds: A review. Chemical Engineering Journal 284:582-598.

Chong, M.N., Jin, B., Chow, C.W.K., Saint, C. (2010) Recent developments in photocatalytic water treatment technology: a review. Water Research 44:2997−3027.

Chu, W., Gao, N.Y., Deng, Y. (2009) Performance of A Combination Process of UV/H_2O_2/Micro-Aeration for Oxidation of Dichloroacetic Acid in Drinking Water. Clean 37(3):233-238.

Clarizia, L., Spasiano, D., Di Somma, I., Marotta, R., Andreozzi, R., Dionysiou, D.D. (2014) Copper modified TiO_2 catalysts for hydrogen generation through photoreforming of organics. A short review. International Journal of Hydrogen Energy 39:16812-16831.

Comninellis, C., Kapalka, A., Malato, S., Parsons, S.A., Poulios, I., Mantzavinos, D. (2008) Perspective advanced oxidation processes for water treatment: advances and trends for R&D. Journal of Chemical Technology and Biotechnology 83:769-776.

Daghrir, R., Drogui, P., Robert, D. (2012) Modified TiO_2 for environmental photocatalytic applications: A review. Industrial and Engineering Chemistry Research 52:3581-3599.

Deng, Y., Zhao, R. (2015) Advanced oxidation processes (AOP) in wastewater treatment. Current Pollution Reports 1:167-176.

Dewil, R., Mantzavinos, D., Poulios, I., Rodrigo, M.A. (2017) New perspectives for advanced oxidation processes. Journal of Environmental Management 195:93-99.

Dionysiou, D.D., Li Puma, G., Ye, J., Schneider, J., Bahnemann, D. (2016) Photocatalysis: Applications. Cambridge: The Royal Society of Chemistry.

Distefano, T., Kelly, S. (2017) Are we in deep water? Water scarcity and its limits to economic growth. Ecological Economics 142:130-147.

Domènech, X., Jardim, W.F., Litter, M.I. (2004) Procesos avanzados de oxidación para la eliminación de contaminantes. Eliminación de contaminantes por fotocatálisis heterogénea, 3−26. Blesa, M. A., Sánchez, B., CIEMAT, Madrid, Spain.

Esclapez, M.D., Tudela, I., Díez-García, M.I., Sáez, V., Rehorek, A., Bonete, P., González-García, J. (2012) Towards the complete dechlorination of chloroacetic acids in water by sonoelectrochemical methods: Effect of the anodic material on the degradation of trichloroacetic acid and its by-products. Chemical Engineering Journal 197:231-241.

Fang, W., Xing, M., Zhang, J. (2017) Modifications on reduced titanium dioxide photocatalysts: A review. Journal of Photochemistry and Photobiology C: Photochemistry Reviews 32:21-39.

Fernández-Castro, P., Vallejo, M., San Román, M.F., Ortiz, I. (2015) Insight on the fundamentals of advanced oxidation processes. Role and review of the determination methods of reactive oxygen species. Journal of Chemical Technology and Biotechnology 90:796-820.

Ferrari, A.C., Bonaccorso, F., Falko, V., Novoselov, K.S., Roche, S., Boggild, P., *et al*. (2015) Science and technology roadmap for graphene, related two-dimensional crystals, and hybrid systems. Nanoscale 7:4598-4810.

Frank, S.N., Bard, A.J. (1977) Journal of the American Chemical Society 99:303-304.

Friedmann, D., Mendive, C., Bahnemann, D. (2010) TiO_2 for water treatment: Parameters affecting the kinetics and mechanisms of photocatalysis Applied Catalysis B: Environmental 99:398-406.

Fujishima, A., Honda, K. (1972) Electrochemical photolysis of water at a semiconductor electrode. Nature 328:37-38.

Gaya, U.I., Abdullah, A.H. (2008) Heterogeneous photocatalytic degradation of organic contaminants over titanium dioxide: A review of fundamentals, progress and problems. Journal of Photochemistry and Photobiology C: Photochemistry Reviews 9:1-12.

Gómez-Pastora J, Dominguez S, Bringas E, Rivero MJ, Ortiz I, Dionysiou DD (2016) Review and perspectives on the use of magnetic nanophotocatalysts (MNPCs) in water treatment. Chemical Engineering Journal 310:407-427.

Hou, W., Cronin, S.B. (2013) A review of surface plasmon resonance-enhanced photocatalysis. Advanced Functional Materials 23:1612-1619.

Hummer, W.S., Hoffeman, R.E. (1958) Preparation of graphitic oxide. Journal of the American Chemical Society 8:1339.

Jia, J., Li, D., Wan, J., Yu, X. (2016) Characterization and mechanism analysis of graphite/C-doped TiO_2 composite for enhanced photocatalytic performance. Journal of Industrial and Engineering Chemistry 33:162-169.

Jiang, X., Nisar, J., Pathak, B., Zhao, J., Ahija, R. (2013) Graphene oxide as a chemically tunable 2-D material for visible-light photocatalyst applications. Journal of Catalysis 299:204-209.

Julkapli, N.M., Bagheri, S. (2015) Graphene supported heterogeneous catalysts: an overview. International Journal of Hydrogen Energy 40:948-979.

Khan M.R., Chuan T.W., Yousuf A., Chowdhury M.N.K, Cheng C.K. (2015) Schottky barrier and surface plasmonic resonance phenomena towards the photocatalytic reaction: study of their mechanisms to enhance photocatalytic activity. Catalysis Science & Technology 5:2522-2531.

Kondarides, D.I., Daskalaki, V.M., Patsoura, A., Xenophon, E.V. (2008) Hydrogen production by photo-induced reforming of biomass components and derivatives at ambient conditions. Catalysis Letters 122:26-32.

Kumar, D.P., Kumari, V.D., Karthik, R., Sathish, R., Shankar, M.V. (2017) Shape dependence structural, optical and photocatalytic properties of TiO_2 nanocrystals for enhanced hydrogen production via glycerol reforming. Solar Energy Materials & Solar Cells 163:113-119.

Kumar, S.G., Devi, L.G. (2011) Review on Modified TiO_2 Photocatalysis under UV/Visible Light: Selected Results and Related Mechanisms on Interfacial Charge Carrier Transfer Dynamics. The Journal of Physical Chemistry A 115:13211-13241.

Kyzas, G.Z., Deliyanni, E.A., Matis, K.A. (2014) Graphene oxide and its application as and adsorbent for wastewater treatment Journal of Chemical Technology and Biotechnology 89:196-205.

Leary, R.; Westwood, A. (2011) Carbonaceous nanomaterials for the enhancement of TiO_2 photocatalysis. Carbon 49:741-772.

Lee, S-Y., Park, S-J. (2013) TiO_2 photocatalyst for water treatment applications. Journal of Industrial and Engineering Chemistry 19:1761-1769.

Liu, Y., Li, Z., Green, M., Just, M., Li, Y.Y., Chen, X. (2017) Titanium dioxide nanomaterials for photocatalysis. Journal of Physics D: Applied Physics 50:193003.

Ma, C., Li, Y., Zhang, H., Chen, Y., Lu, C., Wang, J. (2015) Photocatalytic hydrogen evolution with simultaneous photocatalytic reforming of biomass by Er^{3+}:$YAlO_3$/Pt–TiO_2 membranes under visible light driving. Chemical Engineering Journal 273:277-285.

Marschall, R. (2014) Semiconductor composites: strategies for enhancing charge carrier separation to Improve photocatalytic activity. Advanced Functional Materials 24: 2421-2440.

Mehmet A.O., Jean-Jacques, A. (2014) Advanced Oxidation Processes in Water/Wastewater Treatment: Principles and Applications. A Review. Critical Reviews in Environmental Science and Technology, 44:2577-2641.

Morales-Torres, S., Pastrana-Martínez, L.M, Figueiredo, J.L., Faria, J.L., Silva, A.M.T. (2012) Design of graphene-based TiO_2 photocatalysts-A review. Environmental Science and Pollution Research 19:3676-3687.

Nakata, K., Fujishima, A. (2012) TiO_2 photocatalysis: Design and applications. Journal of Photochemistry and Photobiology C: Photochemistry Reviews 13:169-189.

Ng, Y.H., Iwase, A., Bell, N.J., Kudo, A., Amal, R. (2011) Semiconductor/reduced graphene oxide nanocomposites derived from photocatalytic reactions. Catalysis Today 164:353-357.

Nuraje, N., Asmatulu, R., Kudaibergenov, S. (2012) Metal oxide-based functional materials for solar energy conversion: A review. Current Inorganic Chemistry 2:124-146.

O'Regan, B., Grätzel, M. (1991) A low-cost, high-efficiency solar cell based on dye-sensitized colloidal TiO_2 films. Nature 353:737-739.

O'Shea, K.E., Dionysiou, D.D. (2012) Advanced oxidation processes for water treatment. The Journal of Physical Chemistry Letters 3:2112-2113.

Pai, M.R., Banerjee, A.M., Rawool, S.A., Singhal A., Nayak, C., Ehrman, S.H., Tripathi A.K., Bharadwaj, S.R. (2016) A comprehensive study on sunlight driven photocatalytic hydrogen generation using low cost nanocrystalline Cu-Ti oxides. Solar Energy Materials & Solar Cells 154:104-120.

Pawar, R.C., Lee, C.S. (2015) Heterogeneous nanocomposite-photocatalysis for water purification. Oxford: Elsevier Inc.

Pelaez, M., Nolan, N.T., Pillai, S.C., Seery, M.K., Falaras, P., Kontos, A.G., Dunlope, P.S.M., Hamilton, J.W.J., Byrne, J.A., O'Shea, K., Entezari, M.H., Dionysiou, D.D. (2012) A review on the visible light active titanium dioxide photocatalysts for environmental applications. Applied Catalysis B: Environmental 125:331- 349.

Peng, S., Ding, M., Yi, T., Zhan, Z., Li, Y. (2015) Photocatalytic hydrogen evolution and decomposition of glycerol over $Cd_{0.5}Zn_{0.5}S$ solid solution under visible light irradiation. Environmental Progress & Sustainable Energy 35:141-148.

Perrozzi, F., Prezioso, S., Ottaviano, L. (2015) Graphene oxide: from fundamentals to applications. Journal of Physics: Condensed Matter 27:013002.

Quinteiro, P., Ridoutt, B.G., Arroja, L., Dias, A.C. (2018) Identification of methodological challenges remaining in the assessment of a water scarcity footprint: a review. The International Journal of Life Cycle Assessment 23:164-180.

Ribeiro, A.R., Nunes, O.C., Pereira, M.F.R., Silva, A.M.T. (2015) An overview on the advanced oxidation processes applied for the treatment of water pollutants defined in the recently launched Directive 2013/39/EU. Environment International 75:33-51.

Sakai, H., O. Autin, O., Parson, S. (2013) Change in haloacetic acid formation potential during UV and UV/H_2O_2 treatment of model organic compounds. Chemosphere 92:647-651.

Schneider, J., Matsuoka, M., Takeuchi, M., Zhang, J., Horiuchi, Y., Anpo, M., Bahnemann, D.W. (2014) Understanding TiO_2 Photocatalysis: Mechanisms and Materials. Chemical Reviews 114 (19):9919-9986.

Simonsen, M.E. (2014) Chapter 4: Heterogeneous photocatalysis. The Netherlands: Elsevier Inc.

Spasiano, D., Marotta, R., Malato, S., Fernandez-Ibañez, P., Di Somma, I. (2015) Solar photocatalysis: Materials, reactors, some commercial, and pre-industrialized applications. A comprehensive approach, Applied Catalysis B: Environmental 170-171:90-123.

Tollefson, J. (2011) How green is my future?. Nature 473:135.

Van Gerven, T., Mul, G., Moulijn, J., Stankiewicz, A. (2007) A review of intensification of photocatalytic processes. Chemical Engineering and Processing 46:781-789.

Wang, K., Guo, J., Yang, M., Junji, H., Deng, R. (2009) Decomposition of two haloacetic acids in water using UV radiation, ozone and advanced oxidation processes. Journal of Hazardous Materials 162:1243-1248.

Wang, R., Hashimoto, K., Fujishima, A. (1997) Light-induced amphiphilic surfaces. Nature 388:431-432.

Wen, J., Li, X., Liu, W., Fang, Y., Xie, J., Xu, Y. (2015) Photocatalysis fundamentals and surface modification of TiO_2 nanomaterials. Chinese Journal of Catalysis 36:2049-2070.

Zhang, P., Wang, T., Gong, J. (2015) Mechanistic understanding of the plasmonic enhancement for solar water splitting. Advanced Materials 27:5328-5342.

Zhang, Y., Collins, C., Graham, N., Templeton, M.R., Huang, J., Nieuwenhuijsen, M. (2010) Speciation and variation in the occurrence of haloacetic acids in three water supply systems in England. Water and Environment Journal 24:237-245.

Zhang, Z., Yang, W., Zou, Z., Xu, F., Wang, X., Zhang, B., Tang, J. (2012) One-pot, solvothermal synthesis of TiO_2-graphene compositenanocheets. Journal of Colloid and Interface Science 386:198-204.

CHAPTER 2

MATERIALS AND METHODS

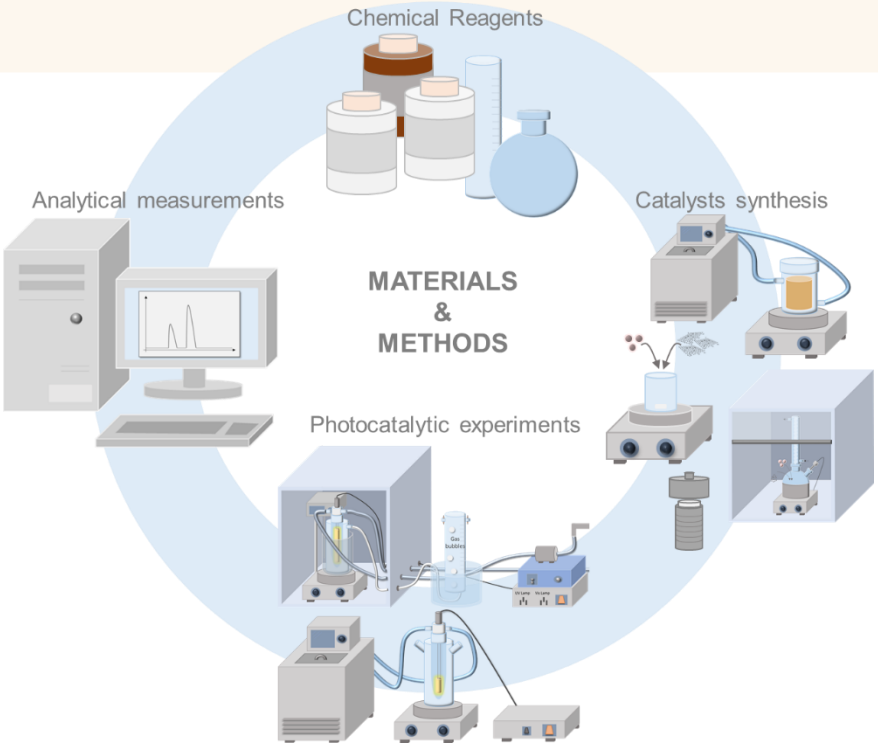

This chapter includes the characteristics of the chemicals employed in the experimental part of present thesis, specifies the procedure used to synthesize the photocatalysts, explains the methodology followed during the photocatalytic experiments and, describes the analytical methods.

2.1. Chemical reagents

All the reagents and standards used in this thesis are detailed in Table 2.1.

Table 2.1 List of chemicals used in the experimental work

Reagent	Formula	Supplier	Use
2,4-Dinitrophenylhydrazine (DNPH)	$C_6H_6N_4O_4$	Sigma-Aldrich	·OH measurement
Acetic acid	$C_2H_4O_2$	Panreac	Liquid phase intermediates
Acetone	C_3H_6O	Merck	Liquid phase intermediates
Acetonitrile	C_2H_3N	Fisher Chemical	·OH measurement
Benzoquinone	$C_6H_4O_2$	Sigma-Aldrich	Trapping molecule
Buffer solution pH 4	H_3PO_4-NaH_2PO_4	Panreac	·OH measurement
Copper (II) sulfate 5-hydrate	$CuSO_4 \cdot 5H_2O$	Panreac	Cooling bath

Table 2.1 List of chemical used in the experimental work (continuation)

Reagent	Formula	Supplier	Use
Crude glycerol	$C_3H_8O_3$	Solartia (Biodiesel Plant)	H_2 production
Dichloroacetic acid (DCA)	$C_2H_2Cl_2O_2$	Sigma-Aldrich	Target pollutant
Dimethyl sulfoxide (DMSO)	C_2H_6SO	Scharlau	·OH measurement
Ethanol	C_2H_6O	Panreac	Liquid phase intermediates
Ethylene glycol (EG)	$C_2H_6O_2$	Panreac	Photocatalyst synthesis and liquid phase intermediates
Formaldehyde	CH_2O	Panreac	$^{\bullet}OH$ measurement
Formic acid (FA)	CH_2O_2	Panreac	Trapping molecule and liquid phase intermediates
Glyceraldehyde	$C_3H_6O_3$	Acros Organics	Liquid phase intermediates
Glycerol	$C_3H_8O_3$	Honeywell	H_2 production
Graphene oxide (GO)	C:O	Nanoinnova	H_2 production
Graphite	C	Acros Organics	GO synthesis
Hexacloroplatinic (IV) acid hexahydrate	$H_2PtCl_6{\cdot}6H_2O$	Sigma-Aldrich	Photocatalysts synthesis
Hydrochloric acid	HCl	Panreac	GO synthesis

Table 2.1 List of chemical used in the experimental work (continuation)

Reagent	Formula	Supplier	Use
Hydrogen peroxide	H_2O_2	Scharlau	GO synthesis
Hydroxyacetone	$C_3H_6O_2$	Acros Organics	Liquid phase intermediates
Inorganic carbon (IC) standard	Na_2CO_3 + $NaHCO_3$	Panreac	Dissolved organic carbon (DOC) measurement
Methanol	CH_4O	Panreac	Liquid phase intermediates
Potasium permanganate	$KMnO_4$	Panreac	GO synthesis
Silver nitrate	$AgNO_3$	Sigma-Aldrich	Photocatalysts synthesis
Sodium nitrate	$NaNO_3$	Panreac	GO synthesis
Sulfuric acid	H_2SO_4	Panreac	GO synthesis
Tert-butyl alcohol (t-BuOH)	$C_4H_{10}O$	Sigma-Aldrich	Trapping molecule
Titanium dioxide Aeroxide® P25	TiO_2	Evonik industries	Photocatalyst
TOC Standard	$C_8H_5O_4K$	Panreac	DOC measurement

According to Solartia's specifications analysis, crude glycerol residue contains 78% of glycerol, 18% of water, 3% of salts/ashes, 0.5% of methane and 0.5% of non-glycerol organic matter and it has a golden brown color. The density is 1.263 g mL^{-1} and presents a natural pH of 5.

2.2. Synthesis of the photocatalysts

2.2.1. Synthesis of graphene oxide nanosheets

To synthesize graphene oxide (GO), natural graphite was oxidized according to the modified Hummers' method (Hummer and Hoffeman, 1958) (Figure 2.1). Graphite powder (3 g) and sodium nitrate (1.5 g) were added to concentrated sulfuric acid (70 mL) under stirring at 0 ºC inside a cooling bath. Potassium permanganate (9 g) was added slowly to maintain a suspension temperature of less than 20 ºC under vigorous stirring. Next, the reaction was heated to 35 ºC for 30 min. Then, 50 mL of deionized water were added, and the temperature was increased to 98 ºC. This temperature was maintained for 15 min under stirring. Additional 170 mL of deionized water were added, followed by 4 mL of H_2O_2 (30 vol%). A purification step was then performed in which the mixture was centrifuged (11000 rpm, 5 minutes) (Centrifuge 5810, Eppendorf) and washed with 200 mL of deionized water and HCl aqueous solution (10 vol%, 80 mL) to remove metal ions. The remaining solid was sonicated at 20 kHz and 20% of amplitude during 30 minutes (VCX 750, Sonics Vibra-cell) to obtain exfoliated graphene oxide nanosheets, the sample was centrifuged again at 11000 rpm for 60 minutes, and the supernatant was collected and dried in an oven at 50 ºC overnight (Conterm, Selecta).

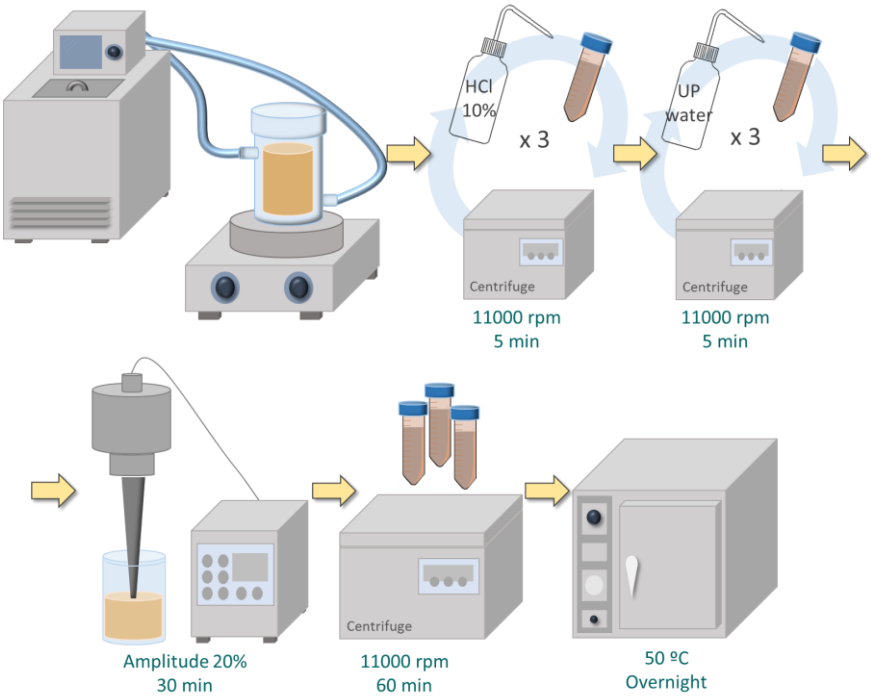

Figure 2.1 Methodology scheme for the preparation of GO nanosheets.

2.2.2. Synthesis of TiO_2/GO photocatalysts

Three types of TiO_2/GO composites were synthesized via different synthesis methods (Figure 2.2). In the mechanical method (M), TiO_2/GO composites were prepared by mechanical mixing and sonication. Briefly, TiO_2 (P25) was added to a GO aqueous dispersion under vigorous stirring for 1 h. The obtained suspension was sonicated for 1 h, yielding an homogeneous gray suspension. The sample was then centrifuged (2000 rpm, 2 minutes), washed with ultrapure water and dried overnight at 50 ºC.

The TiO_2/GO composite was also obtained via a hydrothermal method (H). In brief, TiO_2 was added to the GO dispersion. After stirring for 2 h, the solution was transferred to a 200-mL Teflon-lined stainless steel autoclave and maintained at 120 ºC for 3 h. The resulting composite was recovered

by centrifugation (2000 rpm, 2 minutes), rinsed with ultrapure water (UP) three times and fully dried at 50 ºC overnight.

Finally, TiO_2/GO composites were also prepared via a solvothermal method (S). In a typical synthesis, GO and P25 were mixed in ethylene glycol (100 mL) and stirred for 2 h. After this time, the reaction solution was transferred to a 200-mL Teflon-lined stainless steel autoclave and incubated in an oven at 120 ºC for 3 h. The composite was recovered by centrifugation (2000 rpm, 2 minutes) and washed three times with UP water. Finally, the composite was left to dry overnight at 50 ºC.

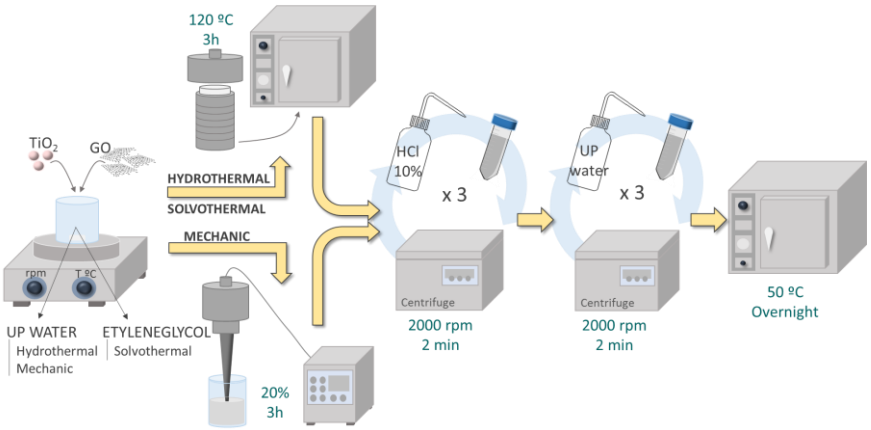

Figure 2.2 Methodology scheme for the preparation of the TiO_2/GO photocatalysts.

The TiO_2/GO photocatalysts are denoted hereafter as H, S or M referring to their preparation method and 1, 5 or 10% stand for wt% of GO used in the preparation (Table 2.2).

Table 2.2 TiO_2/GO photocatalysts nomenclature

Catalysts	Preparation method	GO (wt%)
M1%	Mechanical	1%
M5%		5%
M10%		10%
H1%	Hydrothermal	1%
H5%		5%
H10%		10%
S1%	Solvothermal	1%
S5%		5%
S10%		10%

2.2.3. Synthesis of TiO_2/NM and TiO_2/GO/NM photocatalysts via the polyol process

The noble metal (NM) binary photocatalyst TiO_2/NM and TiO_2/GO/NM ternary photocatalysts were synthesized via the polyol process (Figure 2.3). For the Ag-doped TiO_2 and Ag-doped TiO_2/GO (TiO_2/GO/Ag) photocatalysts, TiO_2 and TiO_2/GO (with 5 wt% of GO) were suspended in ethylene glycol (EG), respectively. Then, different amounts of the Ag precursor ($AgNO_3$) dissolved in EG were added slowly under magnetic stirring. The mixed solution was refluxed in a two-necked round-bottom flask fitted in a heating mantle under magnetic stirring at 140 ºC for 2 h. Lastly, the solid was washed with UP water several times and recovered by centrifugation (11000 rpm, 30 minutes). Solids with 1, 5 and 10 wt% of

Ag content were synthesized. TiO_2 and TiO_2/GO (with 5 wt% of GO) coupled with Pt nanoparticles were prepared similarly using $H_2PtCl_6 \cdot 6H_2O$ as precursor. Finally, composites with 0.2, 0.5 and 1 wt% of Pt load were obtained.

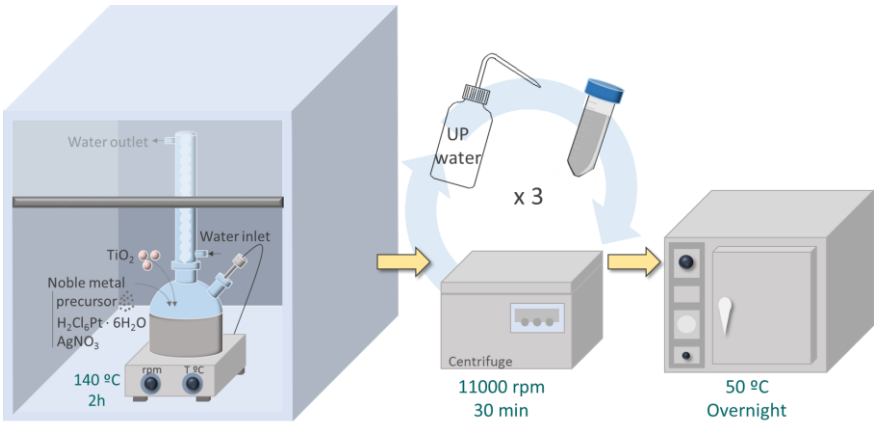

Figure 2.3 Methodology scheme for the preparation of the TiO_2/NM and TiO_2/GO/NM photocatalysts via the polyol process.

2.2.4. Synthesis of TiO_2/Pt and TiO_2/GO/Pt photocatalysts via photodeposition

A simple two-step process was used in the preparation of a series of composite photocatalysts TiO_2/GO(x)/Pt(y) (x=0-5 wt%; y=0-3.8 wt%) (Figure 2.4). In the initial step, TiO_2/GO composites were synthesized by a thermal method in which GO (Nanoinnova Technologies) was dispersed by ultrasonication in a solution of ethanol/water prior to the addition of TiO_2. This mixture was then transferred to a Teflon-sealed stainless steel autoclave and stirred at 125 ºC for 4 h. The product was recovered by centrifugation, washed with UP water and ethanol and dried under vacuum at 50 ºC overnight. In the final step, a photodeposition method was carried out in the presence of the TiO_2 or TiO_2/GO photocatalysts and

$H_2PtCl_6 \cdot 6H_2O$ in a 10 vol% methanol aqueous solution at ambient temperature. The platinum deposition was achieved under UV irradiation, for 3 h, using a 450 W mercury-vapor lamp (ACE-HANOVIA). The products were isolated by the procedure described above for the TiO_2/GO photocatalyst.

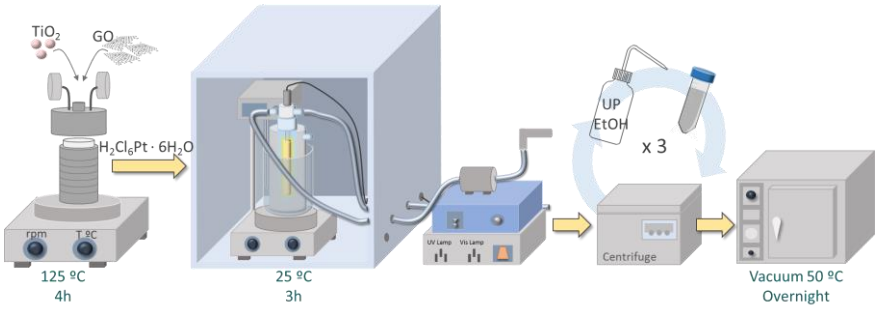

Figure 2.4 Methodology scheme for the preparation of the TiO_2/Pt and TiO_2/GO/Pt photocatalysts via photodeposition.

2.3. Characterization of the photocatalysts

2.3.1. Atomic force microscopy (AFM)

Atomic force microscopy is a very-high-resolution type of scanning probe microscopy (SPM), with demonstrated resolution on the order of fractions of a nanometer, more than 1000 times better than the optical diffraction limit. SPM is a powerful technique to image solid surfaces directly on the atomic scale. The SPM instrument differs from conventional microscopes, such as optical or electron microscopes, in that it has no lens to magnify a specimen's image. Instead, SPM utilizes an atomically sharp probe tip to measure a local topography or chemical/physical property of a sample surface. AFM instrument typically consists on a cantilever, support for cantilever, piezoelectric element, probe tip, detector of deflection and motion of the cantilever, xyz drive and, sample stage. AFM can operate in either a static or dynamic mode. In the static mode, the AFM tip is always

in contact with the sample surface during scanning. The repulsive force exerted on the tip from the sample is measured by the deflection of the cantilever and recorded to map out the topography of the sample surface. In the dynamic mode, the AFM cantilever is periodically oscillated near the sample surface. The tip-sample interaction modulates the amplitude, phase, and resonant frequency of the cantilever oscillation. Hence the force can be measured from the changes in these oscillation parameters (Che and Védrine, 2012). In this work, AFM images were obtained with a Park Systems XE-100 microscope in true non-contact mode with a plastic substrate.

2.3.2. Transmission electron microscopy (TEM)

Electron microscopes (EM) are used to obtain accurate data on the morphology, size, and spatial distribution of small particles on supports. Transmission electron microscopes are complex optical systems that produce high-magnification images of thin specimens. These microscopes use a high-energy electron beam to probe the specimen and collect electrons that have been scattered in the forward direction, that is, they operate in transmission. The magnification in electron microscopes can be tuned between 10^3 and 10^6, to resolve distances down to 1.5-1.8 Å. They are essential in the study of crystallography, defects, surfaces, and interfaces in a wide variety of solids. Transmission electron microscope (TEM) instrument generally consists of an electron gun, probe-forming lenses and apertures, specimen holder, image-forming lenses and apertures, electron detectors and, vacuum system (Che and Védrine, 2012). In TEM, a highly focused electron probe is scanned across the material and various types of scattering are collected as a function of position. The transmitted electrons at a high scattering angle form high-resolution images (Singh, 2016). In the present thesis, transmission

electron microscopy observations were performed on a JEOL JEM-2100 electron microscope.

2.3.3. Energy dispersive X-ray spectroscopy (EDX)

Energy dispersive X-ray spectroscopy (EDX) is a chemical microanalysis technique used in conjunction with electron microscopy instruments. The EDX technique detects x-rays emitted from the sample during bombardment by an electron beam to characterize the elemental composition of the analyzed volume. Features or phases as small as 1 µm or less can be analyzed. When the sample is bombarded by the electron beam, electrons are ejected from the atoms comprising the sample's surface. The resulting electron vacancies are filled by electrons from a higher state, and an x-ray is emitted to balance the energy difference between the two electrons' states. The x-ray energy is characteristic of the element from which it was emitted. The EDX detector measures the relative abundance of emitted x-rays versus their energy. When an incident x-ray strikes the detector, it creates a charge pulse that is proportional to the energy of the x-ray. The charge pulse is converted to a voltage pulse by a charge-sensitive preamplifier. The signal is then sent to a multichannel analyzer where the pulses are sorted by voltage. The energy, as determined from the voltage measurement, for each incident x-ray is sent to a computer for display and further data evaluation. The spectrum of x-ray energy versus counts is evaluated to determine the elemental composition of the sampled volume. An EDX microanalysis system (OXFORD Instruments) installed on a JEOL JEM-2100 electron microscope was employed in this thesis for EDX analyses.

2.3.4. Nitrogen adsorption-desorption for specific surface area calculation

The adsorption-desorption isotherm of N_2 consists on the adsorption of nitrogen in gas phase on the surface of the solid at a fixed temperature as a function of pressure. This technique provides information on the surface area and the porous structure of the solid. The process is generally carried out by introducing successive loads of gas on the adsorbent being each point of the isotherm the point of equilibrium between the volume of gas adsorbed and the relative pressure of the gas (P/P_0). For each solid, the shape and the hysteresis cycle are related to the different interactions between the N_2 and the surface of the solid. In this sense, six different types of isotherms (I-VI) can be found in the literature according to the IUPAC classification. Moreover, a classification of six hysteresis loops was reported by IUPAC and each of these six characteristic types is fairly closely related to particular features of the pore structure and underlying adsorption mechanism (Thommes *et al*., 2015).

For the determination of the surface area, the method developed by Brunauer, Emmet and Teller (BET) has been used. This method relates the gas adsorbed at a certain relative pressure to the volume adsorbed in a gas monolayer in the solid according to the following equation:

$$\frac{P}{V(P_0-P)} = \frac{1+(c-1)}{V_m c}\frac{P}{P_0} \qquad (2.1)$$

where P is the equilibrium pressure, P_0 the vapor saturation pressure, V the volume of gas adsorbed at a relative pressure P/P_0, V_m the volume adsorbed by the monolayer and “c” is a constant related to the heat of adsorption. The BET method is applied to the range of relative pressures that fit a line in the representation of $P/V(P_0-P)$ versus P/P_0. Once the volume of the monolayer (V_m) has been calculated, it is possible to calculate the specific surface from the following equation:

$$S_{BET} = \frac{V_m A_m N_A}{V_{mol}} \quad (2.2)$$

where S_{BET} is the specific surface, V_{mol} is the molar volume of the gas under normal conditions, A_m is the section occupied by the adsorbed molecule and N_A the Avogadro number. The specific surface area of the solids was measured by the BET method from nitrogen adsorption-desorption data with an adsorption apparatus (Micromeritics, ASAP 2000).

2.3.5. Fourier transform infrared (FT-IR) spectroscopy

Fourier-transform infrared spectroscopy is a technique used to obtain an infrared spectrum of absorption or emission of a solid, liquid or gas. FTIR spectrometer simultaneously collects high-spectral-resolution data over a wide spectral range. The term Fourier-transform infrared spectroscopy originates from the fact that a Fourier transform is required to convert the raw data into the desired spectrum. When exposed to infrared radiation, sample molecules selectively absorb radiation of specific wavelengths which causes the change of dipole moment. Consequently, the vibrational energy levels of sample molecules transfer from the ground state to the excited state. The resulting spectrum represents the molecular absorption and transmission, creating a molecular fingerprint of the sample. A common FTIR spectrometer consists of a source, interferometer, sample compartment, detector, amplifier, A/D convertor, and a computer. The source generates radiation which passes the sample through the interferometer and reaches the detector. Then the signal is amplified and converted to digital signal by the amplifier and analog-to-digital converter, respectively. Finally, the signal is transferred to a computer in which Fourier transform is carried out.

Attenuated total reflection (ATR) is a sampling technique that operates by measuring the changes that occur in a totally internally reflected infrared

beam when the beam comes into contact with a sample. An infrared beam is directed onto an optically dense crystal with a high refractive index at a certain angle. This internal reflectance creates an evanescent wave that extends beyond the surface of the crystal into the sample held in contact with the crystal. In regions of the infrared spectrum where the sample absorbs energy, the evanescent wave will be attenuated or altered. The attenuated energy from each evanescent wave is passed back to the IR beam, which then exits the opposite end of the crystal and is passed to the detector in the IR spectrometer. The system then generates an infrared spectrum. In this work, FT-IR spectra were recorded on a Spectrum Two spectrometer (Perkin Elmer) equipped with an attenuated total reflection (ATR) accessory.

2.3.6. Raman spectroscopy

Raman spectroscopy is a technique used to observe vibrational, rotational, and other low-frequency modes in a system, providing a structural fingerprint. This technique is based on inelastic scattering of monochromatic light, usually from a laser source. Inelastic scattering means that the frequency of photons in monochromatic light changes upon interaction with a sample (Gardiner and Graves, 1989). Photons of the laser light are absorbed by the sample and then reemitted. Frequency of the reemitted photons is shifted up or down in comparison with original monochromatic frequency, which is called the Raman Effect. This shift provides information about vibrational, rotational and other low frequency transitions in molecules. A Raman system typically consists of an excitation source (laser), sample illumination system and light collection optics, wavelength selector (filter or spectrophotometer) and, detector (photodiode array, charge coupled device (CCD) or photomultiplier tube (PMT)). A sample is normally illuminated with a laser beam in the ultraviolet (UV), visible (Vis) or near infrared (NIR) range. Scattered light is collected

with a lens and is sent through interference filter or spectrophotometer to obtain the Raman spectrum of a sample. The Raman spectra of the photocatalysts synthesized in the present work were recorded by a T64000 Triple Raman Spectrometer (HORIBA) with a 514-nm laser.

2.3.7. X-ray diffraction (XRD)

X-ray diffraction is a powerful nondestructive technique for characterizing crystalline materials. It provides information on crystal structure, phase, preferred crystal orientation, and other structural parameters, such as average grain size, crystallinity, strain, and crystal defects. X-ray diffractometers consist of three basic elements: an X-ray tube, a sample holder, and an X-ray detector. XRD is based on constructive interference of monochromatic X-rays and electrons in a crystalline (or powder) sample. When a beam of X-ray photons collides with electrons of an atom, some photons undergo elastic (no energy transfer)/inelastic (energy transfer) scattering according to Bragg's law:

$$n\lambda=2d\sin\theta \qquad (2.3)$$

where d is an inner-plane distance in a given set of lattice and θ is certain degree of incidence angle. The elastically scattered X-ray photons carry information about the electron distribution in nanoparticles; therefore, elastic electrons are measured in diffraction experiments. The scattered waves from different atoms can interfere with each other, and the resultant intensity depends upon whether the waves are in phase (which are additive) or out of phase (which are substractive). Measuring the diffraction pattern therefore allows to deduce the distribution of atoms in a material. Consequently, the X-ray diffraction pattern is the fingerprint of the periodic atomic arrangements in a given material. X-Ray diffraction analysis was performed on a Bruker D8 Advance diffractometer equipped with Cu Kα radiation (λ=1.5418 Angstroms).

2.3.8. X-ray photoelectron spectroscopy (XPS)

X-ray photoelectron spectroscopy (XPS), also known as electron spectroscopy for chemical analysis (ESCA), is a technique for analyzing the surface chemistry of a material. XPS can measure the elemental composition, empirical formula, chemical state and electronic state of the elements within a material. XPS spectra are obtained by irradiating a solid surface with a beam of X-rays while simultaneously measuring the kinetic energy and electrons that are emitted from the top 1-10 nm of the material being analyzed. A photoelectron spectrum is recorded by counting ejected electrons over a range of electron kinetic energies. Peaks appear in the spectrum from atoms emitting electrons of a particular characteristic energy. The energies and intensities of the photoelectron peaks enable identification and quantification of all surface elements. When an atom or molecule absorbs an X-ray photon, an electron can be ejected. The kinetic energy (KE) of the electron depends upon the photon energy ($\hbar\upsilon$) and the binding energy (BE) of the electron.

$$KE=h\upsilon-BE-e_{\varphi} \quad (2.4)$$

where e_{φ} is the working function, which is small and almost constant. By measuring the kinetic energy of the emitted electrons, it is possible to determine which elements are near a material's surface, their chemical states and the binding energy of the electron. The binding energy depends upon a number of factors, including the element from which the electron is emitted, the orbital from which the electron is ejected and the chemical environment of the atom from which the electron was emitted (Venezia, 2003). X-ray photoelectron spectroscopy (XPS) measurements were performed using a SPECS Phoibos 100 MCD5 system with Mg Kα radiation ($\hbar\upsilon$= 1253.6 eV). Photocatalysts were subjected to a low resolution general scan between 1200 and 1 eV with an interval of 1 eV

and a step energy of 90 eV. Subsequently, a high resolution analysis was made in the area of maximum sensitivity using an interval of 0.1 eV.

2.3.9. Thermogravimetric analysis (TGA)

Thermogravimetric analysis (TGA) determines endothermic and exothermic weight loss upon heating, cooling, etc. in solids. TGAs use heat to force reactions and physical changes in materials. Therefore, TGAs are used primarily to determine the composition of materials and to predict their thermal stability. The technique can characterize materials that exhibit weight loss or gain due to sorption/desorption of volatiles, decomposition, oxidation and reduction. Thermogravimetric curves characterize specific compounds due to the unique sequence from physicochemical reactions occurring over specific temperature ranges.

A thermogravimetric analyzer consists of a crucible connected to a balance and inserted into a furnace with control over the atmosphere. The sample is heated following a temperature program and control over the atmosphere; the weight can be recorded versus time or temperature (Che and Védrine, 2012; Singh, 2016). Thermogravimetric analyses of photocatalysts were performed in a Shimadzu DTG-60H Differential Thermal Gravimetric Analyzer by heating the sample in nitrogen flow from 25 ºC to 910 ºC at 20 ºC min^{-1}.

2.3.10. Inductively Coupled Plasma Mass Spectrometry (ICP-MS)

ICP-MS is a sensitive method for analysis and confirmation of metal ions with a high linear dynamic range. Specimens are introduced into an argon plasma consisting of electrons and positively charged argon ions. In the plasma, the material splits into individual atoms that lose electrons and become positively charged ions.

The positive ion beam enters a mass analyzer where the ions are separated according to their mass/charge (m/z) ratio. After passing, the ions hit a special mass detector that detects ions at the higher and lower range (Singh, 2016). In the present thesis, the platinum amount present in the photocatalysts was analyzed on a Perkin Elmer Optima 4300 DV at CACTI. The samples were prepared by calcination and digested with *aqua regia* (HNO_3 + HCl) and hydrofluoric acid (HF), necessary to attack the titanium. This pretreatment was developed in a closed Teflon glass at 120ºC.

2.3.11. UV/Vis diffuse reflectance spectroscopy

UV/Vis diffuse reflectance spectrophotometry is a type of spectroscopy where the diffuse reflection of radiation in the ultraviolet to visible range by a sample is measured. When the beam enters the sample, it can either be reflected off the surface of a particle or be transmitted through a particle. The energy reflecting off the surface is typically lost. The beam that passes through a particle can either reflect off the next particle or be transmitted through the next particle. This transmission-reflectance event can occur many times in the sample, which increases the path length. Finally, such scattered energy is collected by a spherical mirror that is focused onto the detector. The detected light is partially absorbed by particles of the sample, bringing the sample information. In a diffuse reflectance spectrum, the absorbed wavenumber positions are the same as the transmission spectrum. However, the relative intensity between peaks differs from the transmission spectrum because the weak peaks in the transmission spectrum become comparatively stronger in the diffuse reflectance spectrum. The so-called K-M function (F(R)) derived by Kubelka-Munk is used for comparison to transmission spectra or quantitative analysis. In this work, the band gap of the samples was calculated by UV/Vis diffuse reflectance spectroscopy using a Cary 5000 UV-vis-NIR

spectrophotometer (Agilent Technologies) equipped with a sphere diffuse reflectance accessory model 5000.

2.3.12. Photocurrent response

Photocurrent response of photocatalysts allows to study the charges generated by light excitation in semiconductor devices. For the photocurrent analysis, powder samples were compressed under a loading of 10 tons to obtain suitable pellets of 5-mm diameter and 0.5-mm thickness. Two copper leads of 0.2 mm in diameter were fixed to one of the circular surfaces with silver electrodes. The photocurrent was measured with a Keithley 616 Digital Electrometer, by using an Ocean Optics HL2000 tungsten halogen lamp to provide an illumination power of 45 mW on the pellet surface. Photocurrents in the nA range were measured in light OFF-light ON intervals. The photocurrent parameter is defined as P = (ON - OFF) / ON.

2.3.13. Extinction coefficient quantification

The extinction coefficient was determined following the methodology proposed by Cabrera and co-workers (1996) using an UV-1800 spectrophotometer (Shimadzu). With the aim of maximizing out-scattering losses in the radiation detector, the sample cell (optical length, 1 cm) was placed as far as possible from the detector position to facilitate the escape of out-scattered rays (in the forward direction) from the detector view angle. Moreover, a narrow vertical slit was placed before the detector chamber, coinciding exactly with the radiation beam coming out of an empty sample cell. Since out scattering is maximized, the total extinction coefficient was measured.

Experiments from 345 to 455 nm were performed at different catalyst concentrations within the linear range of the extinction *versus*

concentration plots (one for each wavelength). With a linear regression program, enforcing a zero intercept, the specific (per unit mass concentration) extinction coefficient was obtained.

2.4. Photocatalytic degradation of dichloroacetic acid (DCA)

2.4.1. Experimental setup

Figure 2.5 depicts the photoreactor employed for DCA degradation. It was integrated by a 1.00 L Pyrex reaction vessel (Heraeus Laboratory UV Reactor, Heraeus Noblelight GmbH, d = 8.50 cm, h = 25.0 cm) and a medium pressure mercury (Hg) lamp (TQ 150 Z1, Heraeus Noblelight GmbH) immersed in a quartz sleeve in the center of the photoreactor. The working volume was 800 mL. The lamp emitted between 200 and 600 nm, it had maximum emission at 370 nm and it required 150 W. An aqueous solution of copper sulfate (0.05 mol L^{-1}) was circulated to prevent overheating of the suspension and cut off the radiation below 300 nm. The radiation emitted in the UVA, UVB, UVC, and visible spectra was 229.20, 258.90, 27.54, and 961.30 W m^{-2}, respectively.

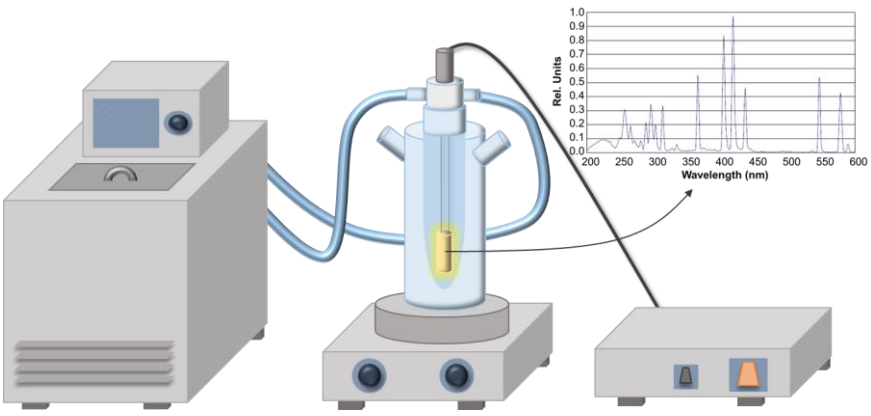

Figure 2.5 Photoreactor Hg-Lamp scheme for DCA degradation.

2.4.2. Methodology

2.4.2.1. Photocatalytic procedure

Preliminary adsorption experiments were performed by mixing 0.8 L of 1000 mg L^{-1} DCA solution and the catalyst under no radiation for 24 h. The source of light was switched on and stabilized during 30 minutes and subsequently, the synthesized photocatalysts were tested by mixing 0.8 L of 1000 mg L^{-1} DCA solution with 0.3 g L^{-1} photocatalysts. Once the photocatalytic degradation had begun, samples were collected at different time intervals and filtered through a 0.45-µm syringe filter (Teknokroma). The photocatalysts reuse study was performed in three successive photocatalytic cycles, and the photocatalysts were recovered via centrifugation.

2.4.2.2. Analysis of DCA and mineralization degree

The DCA and chloride concentration were determined via ion chromatography. It was used an ICS-1100 (Dionex) ion chromatograph with an AS9-HC column using a solution of Na_2CO_3 (9 mM) as the eluent at a flow rate of 1 mL min^{-1} and a pressure of approximately 2000 psi. The equipment was provided with an automatic sampler model AS 40 (Dionex) and the sample injection volume was 25 µL. A conductivity cell (DS6 Heated Conductivity Cell) measured the electrical conductance of the sample ions and produced a signal based on a chemical or physical property of the analyte. Then, the signal was collected in the work station (*software Peaknet*) where it was translated to concentration units by pre-calibrating the different compounds identified.

The measurement of the mineralization of the DCA solutions was followed by means of the dissolved organic carbon (DOC) removal. First, samples were filtered and then they were analyzed in the TOC-VCPH analyzer with auto-sampler ASI-V (Shimadzu). The DOC was calculated

from the substraction of the inorganic carbon (IC) to the total carbon (TC) according to the Standard Methods 5310B (American Public Health Association, 1998). For the analysis of the TC, 50.0 µL of the sample were introduced into the TC combustion tube, burned at 680 ºC in a furnace and transformed to carbon dioxide (CO_2). Then the sample was transported by means of a carrier gas with a flow rate of 150 mL min^{-1} to an electronic dehumidifier where it was dried and, finally, it was transported to the cell of a non-dispersive infrared (NDIR) gas analyzer, where the CO_2 formed was determined. The NDIR generated a signal and the software of the equipment registered a peak with a given area that was proportional to the amount of carbon present in the sample analyzed. In the case of the TIC analysis the sample was cooled down and acidified with phosphoric acid (25.0%). Then, the decomposition of the carbonates and bicarbonates of the sample generates CO_2 which was detected in the NDIR. Afterwards, the procedure is the same that the one for TC. It has to be remarked that the analyzer performed three measurements and an average DOC concentration was calculated. However, if the standard deviation was higher than 0.20 (a.u.), it carried out two additional measurements and then chose the three values with the lowest deviation. The calibration curves were made with a solution of 500 mg L^{-1} total organic carbon (TOC) and a standard solution of 50.0 mg L^{-1} IC.

2.4.2.3. Free hydroxyl radicals quantification

The method employed in this work to determine the $\cdot OH_{free}$ generation was initially proposed by Tai and co-workers (2004), and was based on the reaction between $\cdot OH_{free}$ and dimethyl sulfoxide (DMSO) to produce formaldehyde, which reacted with 2,4-dinitrophenylhydrazine (DNPH) to form the corresponding hydrazone ($DNPH_o$) (2.5) – (2.8).

$$\cdot OH_{free} + (CH_3)_2SO \rightarrow CH_3SO_2H + \cdot CH_3 \quad (2.5)$$

$$\cdot CH_3 + O_2 \rightarrow CH_3OO\cdot \quad (2.6)$$

$$2CH_3OO\cdot \rightarrow HCHO + CH_3OH + O_2 \quad (2.7)$$

$$HCHO + C_6H_3(NO_2)_2NHNH_2 \rightarrow C_6H_3(NO_2)_2NHNCH_2 + H_2O \quad (2.8)$$

Therefore, the $\cdot OH_{free}$ was quantified by determining the formaldehyde concentration when the DNPHo was analyzed through high-performance liquid chromatography (HPLC).

During the experiments, 0.8 L of 1000 mg L^{-1} DCA solution were mixed with 0.3 g L^{-1} of the synthesized photocatalysts and then the photocatalytic process was initiated. At various time intervals, 2 mL of suspension was sampled and filtered through a 0.45 µm syringe filter (Teknokroma). Afterwards, 2.5 mL of pH 4.0 H_3PO_4-NaH_2PO_4 buffer solution, 0.2 mL of 6 mM DNPH solution dissolved in acetonitrile, and 0.3 mL of ultrapure water were added. The mixture was maintained at room temperature for 30 minutes and analyzed using a Waters 2690 HPLC equipped with a Waters 996 Photodiode Array detector and a X-Bridge C18 (5 µm, 4.6x250 mm) analytical column. With a flow rate of 0.6 mL min^{-1}, the mobile phase used was a mixture of methanol and ultrapure water (60/40 v/v) and the detection wavelength was 355 nm. The signal detected was converted to concentration using a calibration curve previously obtained with formaldehyde standards in a range of concentrations between 0.1 and 15 mg L^{-1}. The preparation of the standards was carried out through the derivatization of formaldehyde solutions with known concentration as it was already described.

2.4.2.4. Hydrogen peroxide quantification

H_2O_2 measurements were carried out employing a hydrogen peroxide analytical test kit (photometric method 0.015 - 6.00 mg L^{-1} H_2O_2

Spectroquant) provided by Merck KGaA. In the presence of a phenanthroline derivative hydrogen peroxide reduced copper (II) ions to copper (I) ions. In the process an orange-colored complex was formed and it was determined photometrically.

2.5. Photocatalytic hydrogen production from glycerol

2.5.1. Experimental setup

Figure 2.6 depicts the photoreactor used for hydrogen generation. It was integrated by a 0.3 L sealed cylindrical reactor placed inside a temperature control bath and mounted on a magnetic stirring plate. The light source was immersed in a quartz sleeve placed in the center of the reactor. Two light sources were employed, a 450 W mercury-vapor lamp (ACE-HANOVIA), with a radiation energy in the UV-vis portion of the spectrum, and light emitting diodes (LED) (230 W) emitting in the visible region.

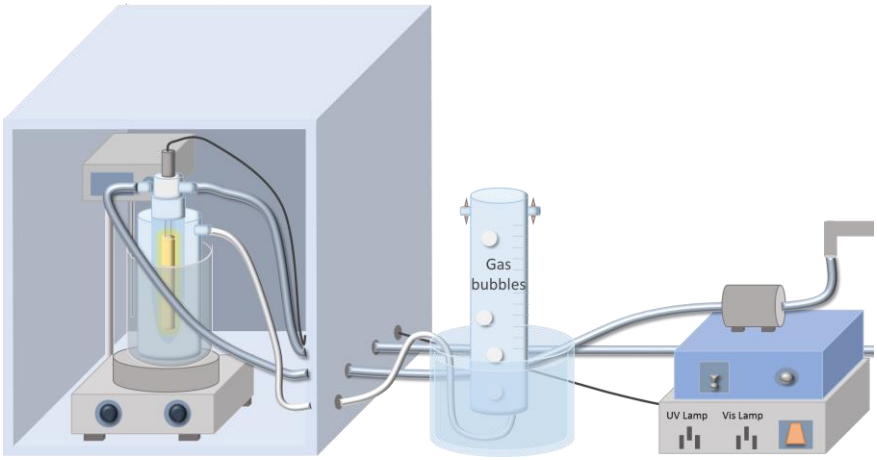

Figure 2.6 Photoreactor for hydrogen production.

2.5.2. Methodology

2.5.2.1. Photocatalytic procedure

For photocatalytic hydrogen generation experiments, 0.3 L of glycerol solution were mixed with TiO_2/GO(x)/Pt(y) photocatalyst and ultrasonicated for 15 minutes; subsequently, the suspension was transferred to the photocatalytic reactor and de-aerated with nitrogen (N 5.0) during 15 minutes before irradiation. The volume of gas generated was collected in an inverted glass graduated tube filled with water and the volume per unit of time was calculated by quantifying the displaced liquid by the gas. The initial concentration of glycerol varied from 5 to 80 vol% for synthetic solutions and from 0.5 to 20% in the case of crude solutions. The catalyst concentration varied from 0.25 to 1 g L^{-1} and initial pH ranged from 3 to 11. In addition, the GO and Pt loading (%wt) were optimized in the catalysts using synthetic glycerol and the optimal conditions were used for the hydrogen production from crude glycerol. Finally, the photocatalytic hydrogen production was carried out at two temperatures, 30 and 40 ºC. The Table 2.3 details the working parameters studied for each type of glycerol.

Table 2.3 Working parameters for hydrogen generation experiments

	Glycerol nature	
	Synthetic	**Crude**
[Glycerol] (%vol)	5-20-50-80	0.5-1-5-20
pH	5-7-11	5-7-11
[Catalyst] (g L^{-1})	0.1-0.25-0.5-0.75-1.0	0.25-0.5-1.0
GO loading (%wt)	1-2-3-5	3
Pt loading (%wt)	1.5-2.5-3.8	3.8
T (ºC)	30-40	30

2.5.2.2. Analysis of gas phase composition

The gas produced was analyzed by gas chromatography using a Micro GC 3000 from Agilent Technologies. The gas composition was analyzed and translated to concentration units by pre-calibrating the different compounds (H_2, O_2, N_2, CO, CH_4, CO_2, C_2H_4, and C_2H_6). Two columns were employed for quantifying these compounds: column A for H_2, O_2, N_2, CO, and CH_4 and column B for CO_2, C_2H_4, and C_2H_6. The carrier gas was argon for column A (molecular sieve) and helium for column B (Polymer Plot U). Moreover, two methods were employed for analyzing the gas composition; the first for H_2 analysis, and the second one for analyzing the rest of compounds. The specifications of the methods used for the measurements are collected in Table 2.4.

Table 2.4 Working conditions of gas chromatograph GC 3000

Analytical methods		
	Method 1	
	Column A	**Column B**
Injection temperature	100 ºC	100 ºC
Column temperature	110 ºC	100 ºC
Injection time	10 ms	20 ms
Run time	150 s	150 s
	Method 2	
	Column A	**Column B**
Injection temperature	90 ºC	90 ºC
Column temperature	100 ºC	60 ºC
Injection time	200 ms	200 ms
Run time	180 s	150 s

2.5.2.3. Analysis of the liquid phase composition

The analysis of the liquid phase composition was carried out using a GC-2010 Plus high-end gas chromatograph (Shimadzu) with a flame ionization detector (FID) and an automatic AOC-5000 injector. First, samples were filtered and then they were analyzed and translated to concentration units by pre-calibrating the different compounds. The injection volume was 2 μL. The characteristics of the analytical method employed for the analysis of the liquid phase are collected in Table 2.5.

Table 2.5 Working conditions of GC-2010 gas chromatograph

Analytical method	
Injector Port	
Temperature	250 ºC
Carrier Gas	Helium
Pressure	182.2 kPa
Split ratio	5
Column Oven	
Initial temperature	40 ºC
Final temperature	230 ºC
Temperature rate	15 ºC min^{-1}
Detector Chanel	
Temperature	250 ºC
Makeup gas	Helium
Makeup flow	30 mL min^{-1}
H_2 flow	40 mL min^{-1}
Air flow	400 mL min^{-1}

2.6. References

American Public Health Association (APHA), 1998. Standard methods for examination of water and wastewater, 20th ed. American Public Health Association, Washington DC, USA.

Cabrera, M.I., Alfano, O.M., Cassano, A.E. (1996) Absorption and scattering coefficients of titanium dioxide particulate suspensions in water, Journal of Physical Chemistry 100:20043-20050.

Che, M., Védrine, J.C. (2012) Characterization of solid materials and heterogeneous catalysts: from structure to surface Reactivity. Wiley-VCH Verlag GmbH & Co. KGaA.

Gardiner, D.J., Graves, P.R. (1989) Practical Raman Spectroscopy. Springer-Verlag Berlin Heidelberg.

Hummer, W.S., Hoffeman, R.E. (1958) Preparation of graphitic oxide. Journal of the American Chemical Society 8:1339.

Singh, A.K. (2016) Engineered Nanoparticles. Structure, properties and mechanism of toxicity. Elsevier Inc.

Tai, C., Peng, J-F., Liu, J-F., Jiang, G-B., Zou, H. (2004) Determination of hydroxyl radicals in advanced oxidation processes with dimethyl sulfoxide trapping and liquid chromatography. Analytica Chimica Acta 527:73-80.

Thommes, M., Kaneko, K., Neimark, A.V., Olivier, J.P., Rodriguez-Reinoso, F., Rouquerol, J., Sing, K.S.W. (2015) Physisorption of gases, with special reference to the evaluation of surface area and pore size distribution (IUPAC Technical Report). Pure and Applied Chemistry.

Venezia, A.M. (2003) X-ray photoelectron spectroscopy (XPS) for catalysts characterization. Catalysis Today 77:359-370.

CHAPTER 3

ROLE OF GO IN TiO_2/GO CATALYSTS FOR DCA DEGRADATION

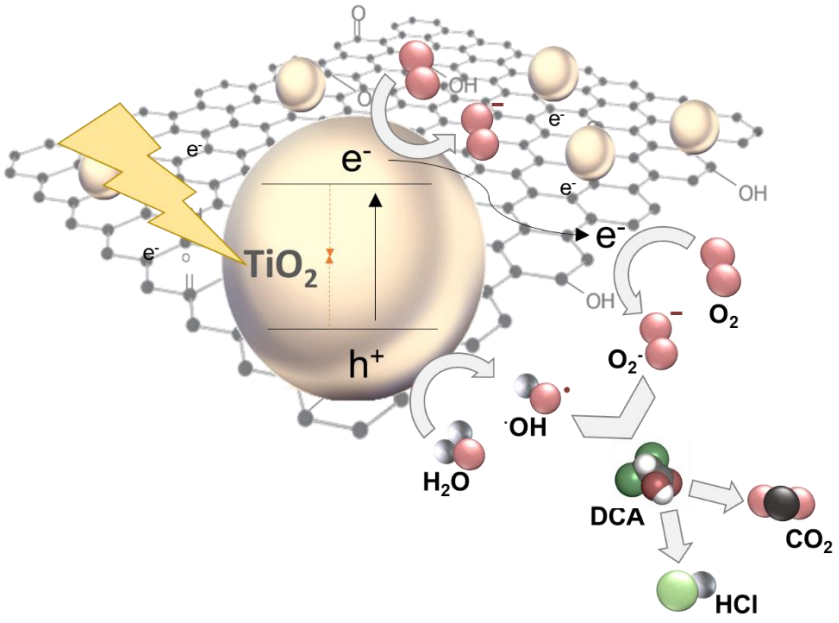

The increasing interest in clean photocatalysis to mitigate water environmental problems, particularly by organic contaminants, has created high demand for TiO_2-based photocatalysts. The photocatalytic activity of this solid remains limited by some disadvantages. Due to the relatively wide band gap energy of 3.2 eV, TiO_2 only absorbs radiation in the ultraviolet region (Rodríguez-Chueca *et al.,* 2015), which represents 4% to 8% of the solar spectrum (Adán *et al.,* 2015). In addition, a large fraction (90%) of electron-hole pairs recombines within nanoseconds after their generation, and only a few are able to migrate to the semiconductor surface for the production of reactive species (Friedman *et al.,* 2010).

In this way, graphene and its derivatives, as graphene oxide (GO), have recently emerged as one very promising candidates for the development of photo-efficient composite catalysts (Cruz *et al.,* 2017). GO can easily react with TiO_2 and be transformed to reduced GO (rGO). Throughout the introductory chapter of this thesis the advantages of the coupling of these materials were described in terms of photocatalytic activity and they can be summarized as follows (Leary and Westwood, 2011):

- GO can act as an electron trapping, avoiding electron-hole pairs recombination.
- The excitation wavelength can be extended to visible region
- The composite can be easily recovered because of the relatively large GO nanosheets.
- The composite can provide quality active sites for reduction/oxidation reactions.

This chapter focuses on the synthesis and characterization of photocatalysts based on TiO_2/GO composites; their performance in the degradation of DCA has been compared to the most widely used form of TiO_2 (P25). Moreover, the influence of the preparation method and the TiO_2/GO weight ratio on the composite performance has been also studied.

Hereafter, in this chapter, the TiO_2/GO photocatalysts will be referred to following the notation described in Table 2.2 of Chapter 2.

3.1. Photocatalysts characterization

Dilute suspensions of H10% and H5% were dropped onto freshly cleaved mica and then analyzed using AFM; the results are shown in Figure 3.1. The mica substrate was covered with GO sheets coupled to TiO_2 nanoparticles. The interaction between GO and TiO_2 can occur via carboxylic acid functional groups or simple physisorption (Wang *et al*., 2012). The height profiles showed an average of 4-nm-thick GO nanoplatelets decorated with TiO_2 nanoparticles for H10% composite. Stankovich and co-workers (2007) reported that the thickness of a single sheet of GO is typically 0.6-1.3 nm, indicating that the GO obtained might be a trilayer sheet. However, the H5% composite showed 2-nm-thick GO nanoplatelets. This fact indicates that in the case of H5%, GO is formed by the stacking of only two sheets, leading to the conclusion that a better exfoliation of GO was indeed achieved under these conditions.

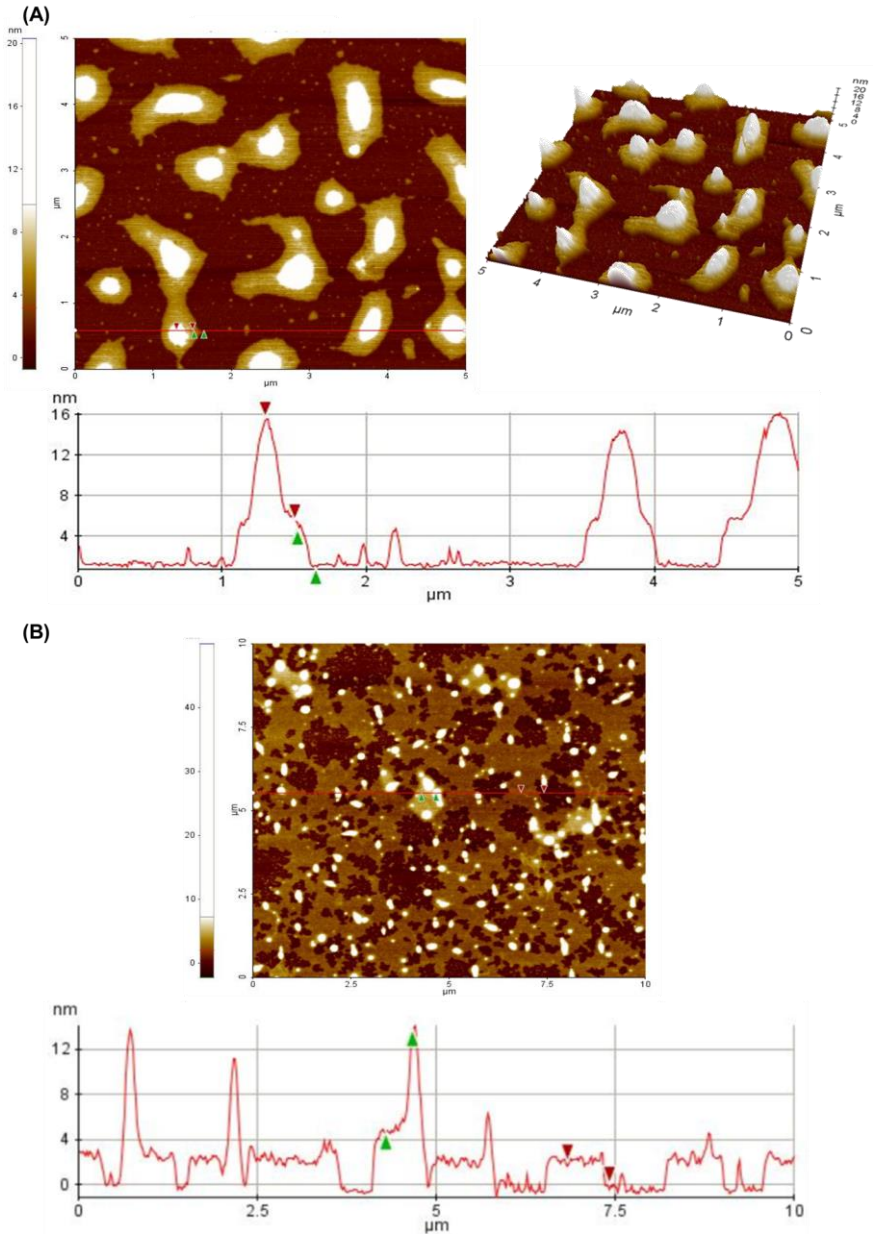

Figure 3.1 AFM image of H10% (A), and H5% (B) photocatalysts and depth profile of the line of interest on the TiO_2/GO solid. Courtesy of Centro Tecnológico de Componentes (CTC).

TiO_2/GO photocatalysts were further examined using transmission electron microscopy. Figure 3.2-A shows the TEM image of the solid H5%; the TiO_2 nanoparticles were dispersed on the GO plane, which exhibited a flake-like structure with some wrinkles. Figures 3.2-B, 3.2-C and 3.2-D present EDX spectra collected from areas S1, S2 and S3 in Figure 3.2-A. The composition of the GO sheets (S1) was carbon with a minor proportion of oxygen. The S2 area exhibited a composition of titanium and oxygen, evidencing the presence of TiO_2 on the GO nanosheets. Finally, no elements were detected in the area S3, demonstrating that the TiO_2 was only found coupled to GO nanosheets. The copper signal is attributable to the sample support.

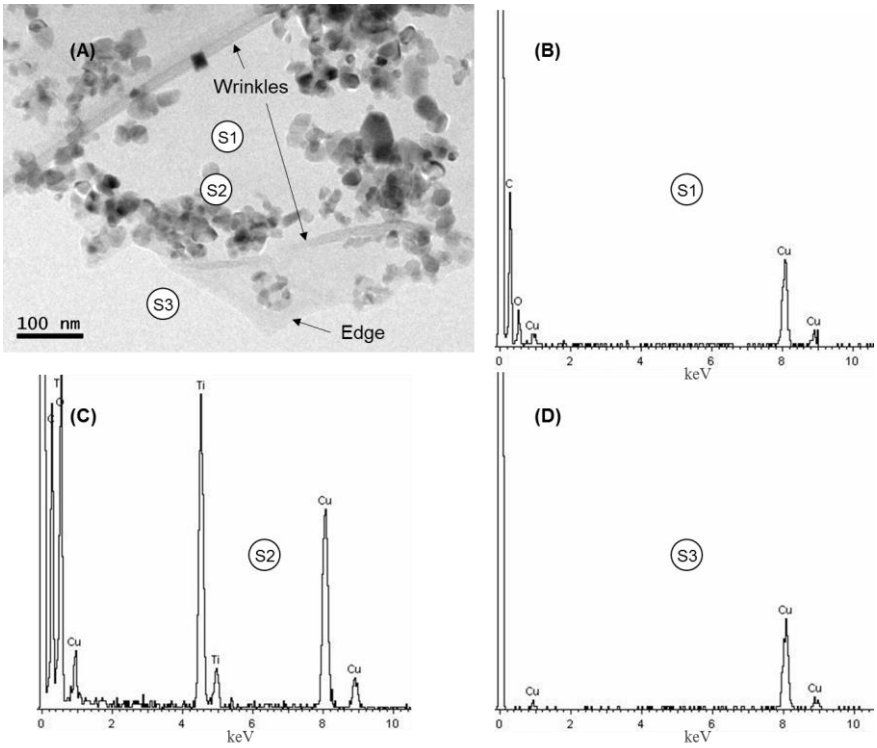

Figure 3.2 TEM image of the photocatalyst H5% (A) and EDX scanning corresponding to zones S1 (B), S2 (C), and S3 (D) in the image.

Figure 3.3 shows the FTIR spectra of the samples TiO_2, GO, H5%, S5% and M5%. The GO spectrum showed many strong absorption peaks corresponding to various oxygen functional groups. The peaks at 3400 cm^{-1} and 1620 cm^{-1} were ascribed to the stretching vibration of water hydroxyl groups and the skeletal vibration of C=C, respectively. The other peaks at 1732, 1380, 1220, and 1055 cm^{-1} were assigned to carboxylate C=O stretching, alcoholic C-O-H, epoxide C-O-C or phenolic C-O-H, and alkoxy C-O, respectively (Zhang *et al.,* 2012; Liang *et al.,* 2014). In the H5% and S5% spectra, the intensity of all absorption peaks corresponding to oxygen functional groups presented a significant decrease compared to the spectrum of bare GO, implying that GO was significantly reduced to rGO during thermal treatment. For M5%, the spectrum showed that the composite retained peaks corresponding to oxygen groups, indicating that GO had not been successfully reduced to rGO. Therefore, the ability of the solid M5% to transport electrons is expected to be lower than those of H5% and S5%. In addition, all composites presented high peaks at 500-900 cm^{-1} that were attributed to the stretching vibrations of Ti-O-Ti and Ti-O-C bonds. Therefore, the above results confirmed the successful preparation of TiO_2/GO composites via hydrothermal and solvothermal treatments; however, the composites synthesized using the mechanical method are not expected to exhibit high photocatalytic activity because reduction of GO was not observed.

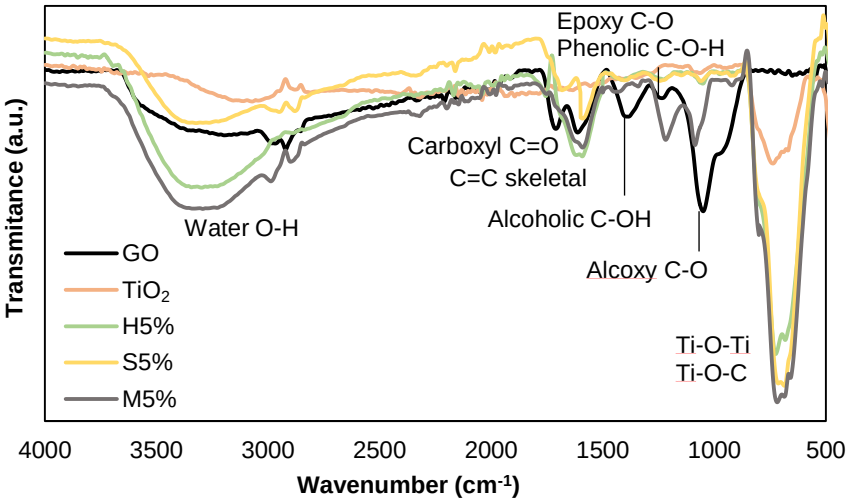

Figure 3.3 FTIR spectra of GO, TiO_2, H5%, S5%, and M5% photocatalysts.

The presence of GO and TiO_2 in the composites was further confirmed by Raman spectroscopy (Figure 3.4). The spectra of the composites presented four peaks in the region below 800 cm^{-1}, with three modes of vibration matching to symmetry B_{1G}, A_{1g} and E_g, corresponding to the crystalline phase anatase. In addition, two extra peaks were observed at 1353 cm^{-1} (D peak) and 1576 cm^{-1} (G peak), confirming the presence of GO in the samples. The composites presented an increased area under the D curve relative to the GO sample (Table 3.1), suggesting the formation of more sp^3 defects in carbon. The defects in the GO sheets were clearly not well repaired during the synthesis step and remained after the removal of oxygen groups. The increased sp^3 defects might be attributable to the strong interaction (Ti-O-C bonds) at the interface of the TiO_2 nanoparticles and GO nanosheets (Wang *et al.,* 2013).

Furthermore, the catalyst M5% presented the highest area under D curve and hence exhibited the highest concentration of sp^3 aggregates. This may be due to the incomplete reduction of GO during the preparation step, which led to the persistence of some oxygen groups on the GO

surface. In the Raman spectrum of H5%, a systematic variation of the frequency of D and G to lower wavelengths and a significant increase in the full width at half maximum (FWHM) of the same bands were also observed (Table 3.1). These features are associated with charge transfer processes in GO. When the frequency moves to lower wavelength, charge transfer occurs due to electron mobility. In the case of S5%, the charge transfer process was less clear. Therefore, lower photocatalytic activity could be expected.

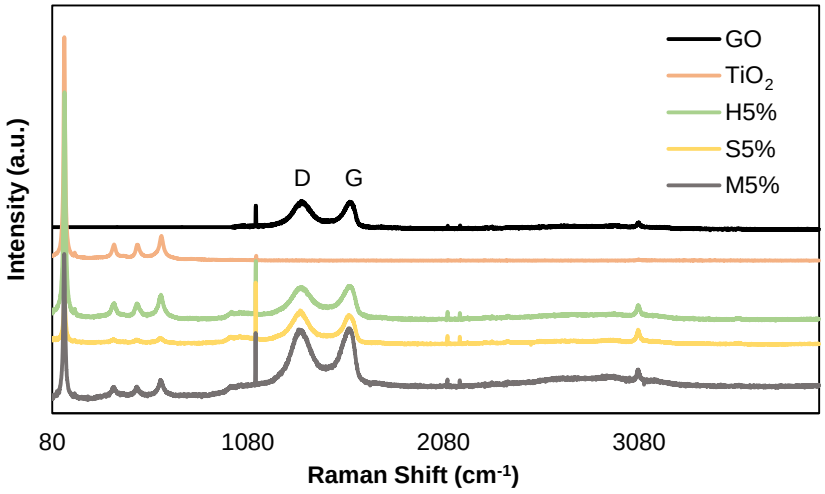

Figure 3.4 Raman spectroscopy of GO, TiO_2, H5%, S5%, and M5% photocatalysts.

Table 3.1 Values of specific parameters of Raman spectra (Figure 3.4).

Sample	D Area	Frequency		FWHM	
		D peak	G peak	D peak	G peak
GO	91311	1356	1584	116	65
H5%	146484	1353	1576	158	105
S5%	117599	1347	1583	122	76
M5%	248818	1350	1573	219	136

Thermal gravimetric analysis of TiO_2, GO, H1%, H5% and H10% in a N_2 atmosphere is shown in Figure 3.5. The thermogravimetric curve of GO presented three differentiated steps of mass loss with temperature in the range from ambient temperature to 900 ºC. The first step corresponds to desorption of physically absorbed water below 100 ºC. Between 200 ºC and 250 ºC, the mass loss is attributable to the removal of oxygen-containing groups. Finally, the third mass loss step observed around 500 ºC is due to the destruction of the carbon skeleton (carbonyl/double bond) of GO (Li *et al*., 2013; Xu *et al*., 2014). The catalysts H1%, H5% and H10% exhibited weight loss roughly parallel to that of GO across the temperature range examined. Subsequent determination of the content of GO in the photocatalysts by TG analysis revealed that 3.87%, 7.27%, 10.95%, 5.62% and 5.59% GO was present in H1%, H5%, H10%, S5% and M5%, respectively.

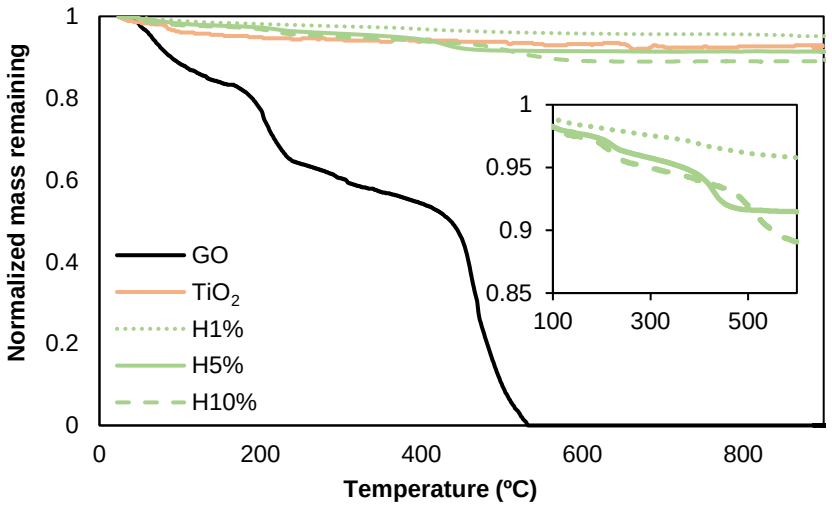

Figure 3.5 Thermal gravimetric analysis of GO, TiO_2, H1%, H5%, and H10% photocatalysts.

To determine the specific surface area of the composite nanomaterial, N_2 adsorption/desorption measurements and the Brunauer-Emmet-Teller (BET) analysis method were used. All composites showed an increment in surface area values compared with TiO_2. The specific area increased with increasing TiO_2/GO weight ratio, reaching specific areas up to 66.71, 68.24 and 62.37 m^2 g^{-1} for H10%, S10% and M10%, respectively (Table 3.2). These observations are in agreement with other works reporting an increment of up to 20% in the specific area values (Wang *et al*., 2012; Morales-Torres *et al*., 2013). The synthesis method did not lead to significant variations in surface areas.

Table 3.2 Specific area and band gap values of photocatalysts

Photocatalyst	Specific area (m^2 g^{-1})	Band gap (eV)
TiO_2	50.0	3.25
H1%	50.6	2.95
H5%	62.2	2.94
H10%	66.7	2.82
S1%	52.0	2.95
S10%	68.2	2.84
M1%	57.3	2.98
M10%	62.3	2.88

XRD analyses were performed to study the crystal phases of the photocatalysts. The results for pristine TiO_2 and H5% are shown in Figure 3.6. Both of them presented the same characteristic crystal planes of anatase and rutile phases corresponding to commercial TiO_2 (P25). This means that TiO_2 structure was not modified by the addition of GO nanosheets. A diffraction peak at 2θ value around 11.3º was observed in the GO curve, indicating the possible existence of trapped water between the layers of hydrophilic GO. This peak is not observed in H5% composite because during the synthesis step the regular stacking of the GO was destroyed by the intercalation of TiO_2 (Liu *et al*., 2013).

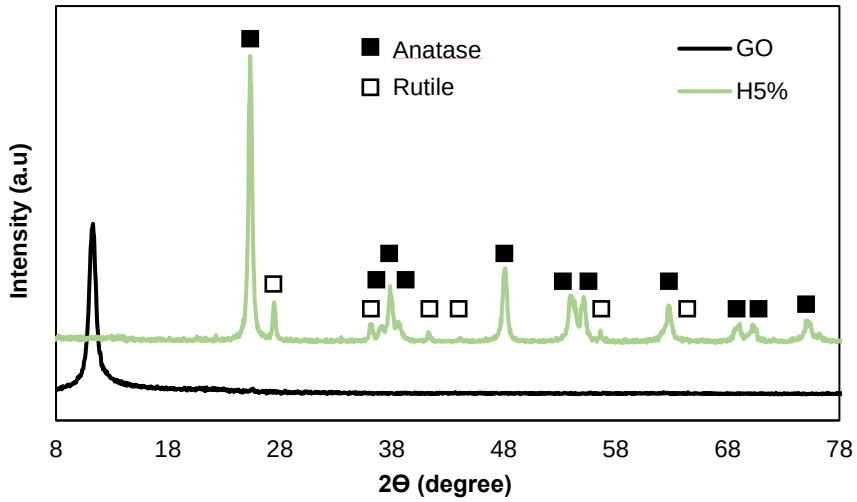

Figure 3.6 XRD patterns of GO, and H5% photocatalyst.

The band gaps of the TiO_2 and TiO_2/GO photocatalysts were estimated from the plots of $[F(R)\hbar\upsilon]^{1/2}$ versus $\hbar\upsilon$. The Kubelka Munk function F(R) is proportional to the equivalent absorption coefficient and is obtained by converting the reflectance according to equation (3.1):

$$F(R)= \frac{(1-R)^2}{2R} \qquad (3.1)$$

Figure 3.7 shows that the band gap of commercial TiO_2 (P25) was 3.25 eV, whereas the band gaps of the composites were significantly reduced (Table 3.2). The value of the band gap decreased after anchoring TiO_2 onto the GO nanosheet, resulting in composites able to absorb visible light up to 440 nm. This phenomenon is the result of the different interaction intensities of C-O and C-Ti during the synthesis process. In the thermal process, Ti and O atoms interact more actively with GO than in the mechanical procedure. Functional groups on the GO surface disappear when GO is reduced during the TiO_2/GO synthesis, as confirmed by FTIR analysis, and the π electrons of the C atom cannot bind with others to form

a delocalized large π bond. Consequently, the remaining unpaired π electrons are bound with more free Ti and O atoms on the surface of TiO_2. This interaction should result in the significant reduction of the band gap of the composites (Lee and Park, 2012; Ni *et al*., 2014).

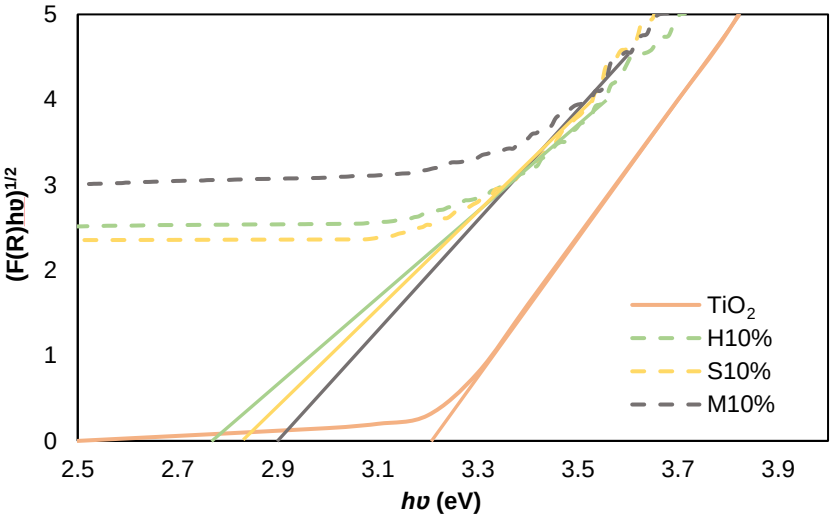

Figure 3.7 Estimated band gaps of TiO_2, H10%, S10%, and M10% photocatalysts.

XPS analysis of the H5% photocatalyst surface was performed. Figure 3.8 shows the section of the high resolution XPS spectrum of H5% photocatalyst. The typical zones of Ti-2p, C-1s, and O-1s were recorded. The Ti $2p_{3/2}$ and Ti $2p_{1/2}$ double signal at 458.6 and 464.2 eV (Figure 3.8-A) corresponded to the binding energy of Ti^{4+} in TiO_2 nanoparticles. The observed spin-orbit splitting between the Ti $2p_{3/2}$ and Ti $2p_{1/2}$ were 5.8 eV. This is in good agreement with binding energies given in the literature for the titanium of Ti^{4+} state in TiO_2 (Hsieh *et al*., 2015). Regarding the C-1s region (Figure 3.8-B), the main peak at 284.2 eV, which is due to he nonoxygenated ring C, and the signals at 286.3 and 288.9 eV of the C in C–O bonds and and the carboxylate C (C=O), were assigned to the partially reduced GO nanosheets in the H5% photocatalyst (Abulizi *et al*., 2014). Finlaly, the typical zone of O-1s signals showed two peaks (Figure

3.8-C), one at 529.6 eV of the oxygen as oxide and another at 531.2 eV of the hydroxyl groups.

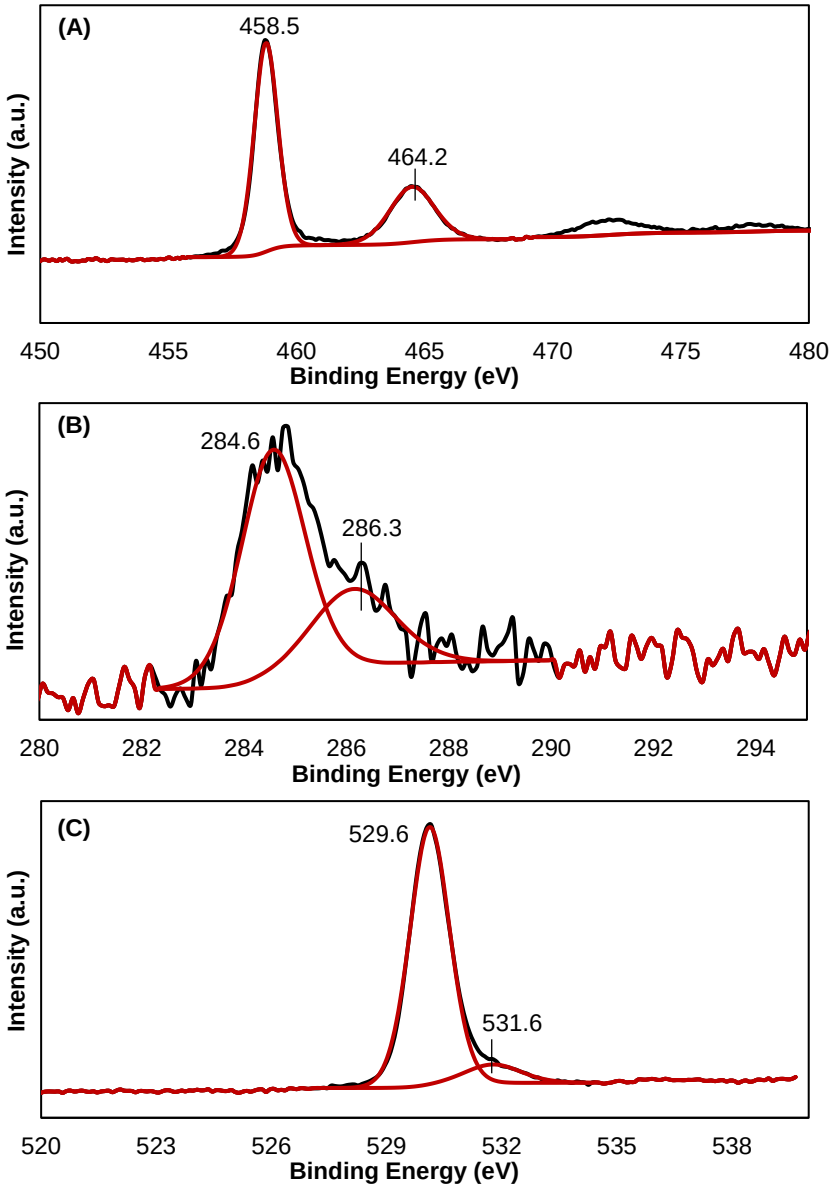

Figure 3.8 High-resolution XPS spectra of H5%: Ti 2p core-level (A), C 1s core-level (B) and O 1s core-level (C).

Thus, the results of the characterization revealed significant differences between the newly synthesized TiO_2/GO photocatalysts that were related both to the synthesis method used and the GO content employed.

3.2. Photocatalytic performance of TiO_2/GO photocatalysts

The photocatalytic degradation of DCA with the novel photocatalysts was measured under UV-Vis light. It is remarkable that the experimental error was determined to be less than 2%. Preliminary experiments of dark adsorption of the target compound onto the catalyst showed that after 24 hours of contact there was no significant adsorption of DCA on TiO_2 or on any of the composites.

The experimental data of DCA degradation were fitted to a zero-th order kinetic model in all cases except in the study without catalyst or when only GO was employed. Figure 3.9 shows the DCA degradation percentage and kinetic constants for eight hours of treatment. It can be observed that DCA cannot be degraded by pure GO. Commercial TiO_2 exhibited lower photocatalytic activity than the novel composites in all cases. After coupling between GO and TiO_2, the photocatalytic degradation in the studied time was improved from 35.37% to 87.10%; the maximum value corresponds to the H5% photocatalyst, increasing the degradation rate 2.6 times. Moreover, for a given TiO_2/GO weight ratio, there was a significant influence of the synthesis method on the photocatalytic activity, especially in the case of composites with a TiO_2/GO weight ratio of 5%.

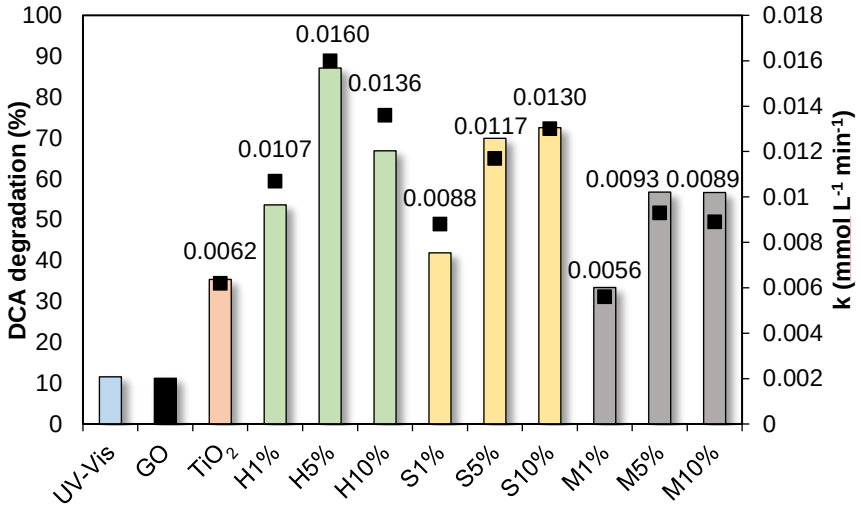

Figure 3.9 DCA degradation percentages after 8 hours of irradiation time and kinetic constants values for each photocatalyst. Conditions: UV-Vis light, $[DCA]_0$ = 1000 mg L^{-1}, [Catalyst] = 0.3 g L^{-1}, T = 20ºC.

The catalysts H5% and S5% reached a photocatalytic DCA degradation after 8 hours of 87.10% and 69.89%, respectively. By contrast, the catalyst M5% only achieved 56.74% of DCA degradation after eight hours of treatment.

Within the use of 1 wt% of GO no significant improvement in the photocatalytic degradation of DCA was attained, regardless of the synthesis method. The catalyst H5%, which was synthesized via the hydrothermal method with a TiO_2/GO weight ratio of 5%, presented the optimal photocatalytic activity and exhibited the highest performance among all prepared materials. These superior results may be due to the charge transfer process observed in the Raman spectra of the hydrothermal composites, which was not so clearly observed for the catalyst S5%. The composite M5% exhibited worse behavior because the coupling between GO and TiO_2 was not adequate and the GO was not completely reduced during synthesis, as confirmed by the FTIR spectra.

Further increasing the TiO_2/GO weight ratio to 10% to obtain the solids H10% and M10% led to a decrease in the degradation rate compared to the catalysts H5% and M5%, although the degradation rate remained higher than that obtained with TiO_2 and with the composites H1% and M1%. Therefore, a high GO load may act as a shield that increases opacity, resulting in a decrease in the irradiation that passes through the suspension (Wang *et al*., 2013). However, the solid S10% exhibited higher photocatalytic activity than the solid S5% as well as slightly higher photocatalytic activity than the catalyst H10%. This higher activity may be due to the greater dispersion of large amounts of GO in ethylene glycol than in water during the synthesis step, which provided a greater contact area between TiO_2 and GO.

Therefore, the results obtained for DCA photocatalytic oxidation revealed a coupled influence of the composite preparation method and GO loading, with promising results compared to the limited activity of conventional TiO_2. Furthermore, the analysis of DCA mineralization based on changes in DOC revealed that the measured values matched undegraded DCA (Figure 3.10). This fact is related to the absence of reaction intermediates during DCA degradation, only phosgene could be formed, that is immediately hydrolyzed in water solution and therefore, it cannot be detected.

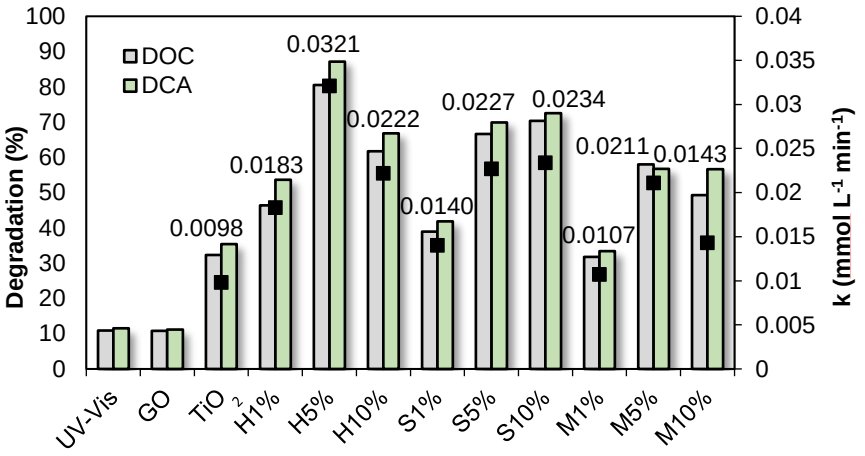

Figure 3.10 DCA and DOC removal after 480 minutes of irradiation time and DOC kinetic constants values for each photocatalyst. Conditions: UV-Vis light, $[DCA]_0$ = 1000 mg L^{-1}, $[DOC]_0$ = 148 mg L^{-1}, [Catalyst] = 0.3 g L^{-1}, T = 20ºC.

Some papers focused on the enhancement of the photocatalytic activity using TiO_2/GO composites can be found in the available literature. However, no clear conclusions have been obtained so far. Perera and co-workers (2012) demonstrated that GO does not work as an independent photocatalyst, but Krishnamoorthy and co-workers (2011) found evidences of photocatalytic activity when graphene oxide was used as catalyst. Szabó and co-workers (2013) and Wojtoniszak and co-workers (2012) reported better photocatalytic activity of the TiO_2 than the composite. On the other hand, Li and co-workers (2013) and Liang and co-workers (2014) found photocatalytic improvement using the composite. The above mentioned authors followed different experimental methods to synthesize the TiO_2/GO composites, which could influence the properties of the catalyst. Another important parameter is the influence of the TiO_2/GO weight ratio in the photocatalytic activity because different results have been reported so far. Morales-Torres and co-workers (2013) synthesized GO/TiO_2 composites with different amounts of GO in relation to TiO_2 ranging from 1% to 6%, finding the best photocatalytic degradation of

methyl orange with a GO/TiO_2 weight ratio of 1.4%. However, composites with a GO/TiO_2 weight ratio of 5% provided the best photoactivity under visible light in degradation of methylene blue according to the work developed by Liu and co-workers (2013). Nguyen-Phan and co-workers (2011) conducted the analysis of the influence of the GO/TiO_2 weight ratio in the range between 1% and 10% in the oxidation of methylene blue under visible irradiation and they concluded that the high graphene content provided the best photocatalytic activity. Therefore, the scattering and the somehow contradictory results reported so far makes it necessary to deeply analyze the potential photocatalytic enhancement of TiO_2/GO composites.

To confirm the performance stability and reusability of the composites, the photocatalytic oxidation of DCA was analyzed in three different cycles using the photocatalyst H5%. The results are shown in Figure 3.11. The catalyst maintained stable and effective photocatalytic activity, with a total photocatalytic activity loss of 4.3% after the third cycle.

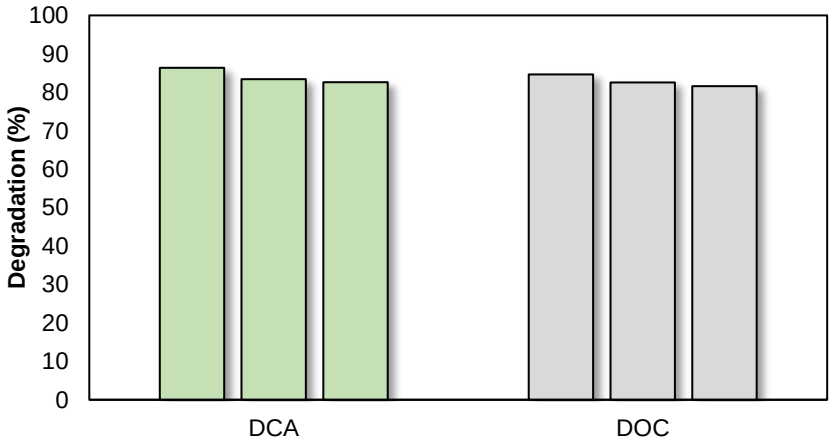

Figure 3.11 DCA degradation and mineralization over the photocatalyst H5% for three successive photocatalytic runs after 480 minutes. Conditions: UV-Vis light, $[DCA]_0$ = 1000 mg L^{-1}, [Catalyst] = 0.3 g L^{-1}, T = 20ºC.

Figure 3.12 shows the proposed reaction scheme of the photocatalytic process using TiO_2/GO as photocatalyst. Under UV-Vis light irradiation, the electron in the valence band is promoted to the conduction band of TiO_2, and the photogenerated electron on the conduction band can effectively reduce oxygen via the GO nanosheets to form superoxide radicals ($O_2^{\cdot-}$). In this case, the GO nanosheets function as co-catalyst for the rapid transfer of the photogenerated electrons from TiO_2, which results in a lower recombination rate and enhanced photocatalytic activity. $O_2^{\cdot-}$ radicals can induce the generation of free hydroxyl radicals ($\cdot OH_{free}$) through an intermediate peroxide process.

On the other hand, the hole in the valence band generates hydroxyl radicals through water oxidation. Finally, two possible reaction pathways can take place in the photocatalytic degradation of the DCA: (i) hydroxyl radicals attack DCA ions at the dichloromethyl group by hydrogen abstraction (3.2)-(3.5), and (ii) hydroxyl radicals can also react oxidizing the negatively charged carboxyl group according to reactions (3.6)–(3.9). (Zalazar *et al.,* 2007; Lovato *et al.,* 2011):

Option 1:

$$CCl_2HCOO^- + \cdot OH \rightarrow \cdot CCl_2COO^- + H_2O \quad (3.2)$$

$$\cdot CCl_2COO^- + O_2 \rightarrow \cdot OOCCl_2COO^- \quad (3.3)$$

$$2 \cdot OOCCl_2COO^- \rightarrow 2COCl_2 + 2CO_2 + O_2 \quad (3.4)$$

$$COCl_2 + H_2O \rightarrow CO_2 + 2HCl \quad (3.5)$$

Option 2:

$$CCl_2HCOO^- + \cdot OH \rightarrow CCl_2HCOO\cdot + {}^{-}OH \quad (3.6)$$

$$CCl_2HCOO\cdot \rightarrow \cdot CHCl_2 + CO_2 \quad (3.7)$$

$$\cdot CHCl_2 + O_2 \rightarrow Cl_2HCOO\cdot \quad (3.8)$$

$$2Cl_2HCOO\cdot \rightarrow 2COCl_2 + H_2O_2 \quad (3.9)$$

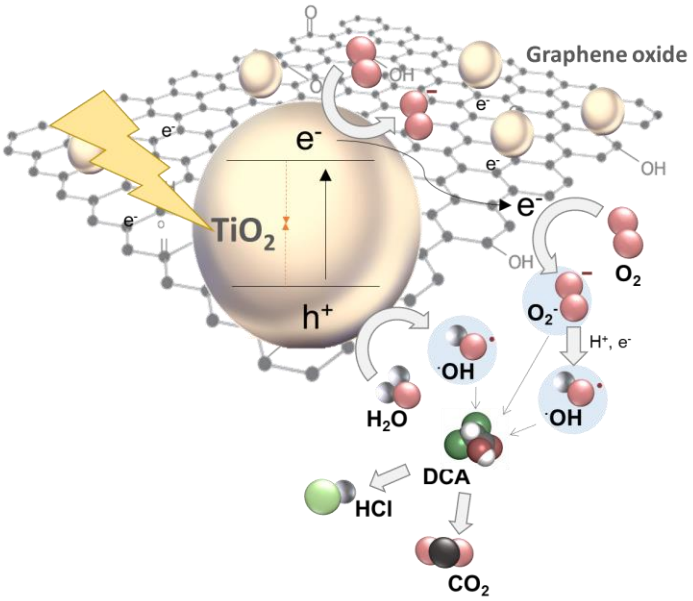

Figure 3.12 Proposed reaction scheme of DCA oxidation over TiO_2/GO photocatalysts.

3.3. Final remarks

Environmental photocatalytic applications of TiO_2/GO nanocomposites have evoked great interest due to the improved performance of these nanocomposites compared to conventional TiO_2 particles. In this chapter, nine novel composites were synthesized by varying the TiO_2/GO weight ratio in the range of 1% to 10% and following three different preparation methods, hydrothermal, solvothermal and mechanical, to obtain an optimized TiO_2/GO photocatalyst. The performance was assessed based on the degradation of DCA, a disinfection by-product, which revealed an improved degradation rate for the new composites compared with bare TiO_2. Photocatalysts with a mass weight ratio of 1% provided the worst results among the newly synthesized catalysts, probably due to an insufficient GO load. For the rest of the composites, the DCA degradation

effectiveness followed the trend H5% > S10% > S5% > H10% > M5% > M10%. Therefore, the composite H5% provided the best photocatalytic activity among all synthesized composites, with a degradation yield of 87.1% after eight hours of treatment and a degradation rate 2.6 times higher than bare TiO_2. High GO content improved the photocatalytic activity of the catalyst S10% due to the best dispersion of large GO loads in ethylene glycol. The composites M5% and M10% displayed the worst behavior due to inadequate coupling between GO and TiO_2 and incomplete reduction of GO during the synthesis process, as confirmed by FTIR spectra. Although the results for DCA degradation showed a coupled influence of the composite preparation method and composition, promising results were achieved. In summary, the novel optimized photocatalyst represents a successful alternative for DCA degradation compared to the limited activity of conventional TiO_2 due to the ability of GO sheets to avoid electron-hole recombination. These results increase the potential application of photocatalysis for the remediation of polluted water and wastewaters.

3.4. References

Abulizi, A., Yang, G.H., Zhu, J.J. (2014) One-step simple sonochemical fabrication and photocatalytic properties of Cu_2O-rGO composites. Ultrasonics Sonochemistry 21:129-135.

Adán, C., Marugán, J., Obregón, S., Colón, G. (2015) Photocatalytic activity of bismuth vanadates under UV-A and visible light irradiation: Inactivation of Escherichia coli vs oxidation of methanol. Catal Today 240:93-99.

Cruz, M., Gómez, C., Duran-Valle, C.J., Pastrana-Martínez, L.M., Faria, J.L.,Silva A.M.T., Faraldos, M., Bahamonde, A. (2017) Bare TiO_2 and graphene oxide TiO_2 photocatalysts on the degradation of selected

pesticides and influence of the water matrix. Applied Surface Science 416:1013-1021.

Friedman, D., Mendive, C., Bahneman, D. (2010) TiO_2 for water treatment: Parameters affecting the kinetics and mechanisms of photocatalysis. Applied Catalysis B: Environmental 99:398-406.

Hsieh, S.H., Chen, W.J., Wu, C.T. (2015) Pt-TiO_2/graphene photocatalysts for degradation of AO7 dye under visible light. Applied Surface Science 340:9-17.

Krishnamoorthy, K., Mohan, R., Kim, S.L. (2011) Graphene oxide as photocatalytic material. Applied Physics Letters 98:244101.

Leary, R., Westwood, A. (2011) Carbonaceous nanomaterials for the enhancement of TiO_2 photocatalysis. Carbon 49:741-772.

Lee, J.K., You, K.H, Park, C.B. (2012) Highly photoactive, low bandgap TiO_2 nanoparticles wrapped by graphene. Advanced Materials 24:1084-1088.

Li, J., Zhou, S.L., Hong, G-B., Chang, C-T. (2013) Hydrothermal preparation of P25-graphene composite with enhanced adsorption and photocatalytic degradation of dyes. Chemical Engineering Journal 219:486-491.

Liang, D., Cui, C., Hu, H., Wang, Y., Xu, S., Ying, B., Li, P., Lu, B., Shen, H. (2014) One-step hydrothermal synthesis of anatase TiO_2/reduced graphene oxide nanocomposites with enhanced photocatalytic activity. Journal of Alloys and Compounds 582:236-240.

Liu L., Bai H., Liu J., Sun D.D. (2013) Multifunctional graphene oxide-TiO_2-Ag nanocomposites for high performance water disinfection and decontamination under solar irradiation. Journal of Hazardous Materials 261:214-223.

Liu, S., Sun, H., Liu, H., Wang, S. (2013) Graphene facilitated visible light photodegradation of methylene blue over titanium dioxide photocatalysts. Chemical Engineering Journal 214:298-303.

Lovato, M.E., Martín C.A., Cassano A.E. (2011) A reaction–reactor model for O_3 and UVC radiation degradation of dichloroacetic acid: The kinetics of three parallel reactions. Chemical Engineering Journal 171:474-489.

Morales-Torres, S., Pastrana-Martínez, L.M, Figueiredo, J.L., Faria, J.L. (2013) Graphene oxide-P25 photocatalysts for degradation of diphenhydramine pharmaceutical and methyl orange dye. Applied Surface Science 275:361-368.

Nguyen-Phan, T.D., Pham, V.H., Shin, E.W., Phan, H.D., Kim, S., Chung, J.S., Kim, E.J., Hur, S.H. (2011) The role of graphene oxide content on the adsorption-enhanced photocatalysis of titanium dioxide/graphene oxide composites. Chemical Engineering Journal 170:226-232.

Ni, Y., Wang, W., Huang, W., Lu, C., Xu, Z. (2014) Graphene strongly wrapped TiO_2 for high-reactive photocatalyst: A new sight for significant application of graphene. Journal of Colloid and Interface Science 428:162-169.

Perera, S.D., Mariano, R.G., Vum K., Nour, N., Seitz, O., Chabal, Y., Balkus, K.J. (2013) Hydrothermal Synthesis of Graphene-TiO_2 Nanotube Composites with Enhanced Photocatalytic Activity. ACS Catalysis 2:949-956.

Rodríguez-Chueca, J., Ferreira, L.C., Fernandes, J.R., Tavares, P.B., Lucas, M.S., (2015) Photocatalytic discolouration of Reactive Black 5 by UV-A LEDs and solar radiation Journal of Environmental Chemical Engineering 3:2948-2956.

Szabó, T., Veres, A., Cho, E., Khim, J., Varga, N., Dekany, I. (2013) Photocatalyst separation from aqueous dispersion using graphene

oxide/TiO_2 nanocomposites. Colloids and surfaces A: Physicochemical and Engineering Aspects 433:230-239.

Stankovich, S., Dikin, D.A., Piner, R.D., Kohlhaas, K.A., Kleinhammes, A., Jia, Y., Wu, Y., Nguyen, S.T., Ruoff, R. (2007) Synthesis of graphene-based nanosheets via chemical reduction of exfoliated graphite oxide. Carbon 45:1558-1565.

Wang, D., Li, X., Chen, J., Tao, X. (2012) Enhanced photoelectrocatalytic activity of reduced graphene oxide/TiO_2 composite films for dye degradation. Chemical Engineering Journal 198-199:547-554.

Wang, P., Wang, J., Wang, X., Yu, H., Yu, J., Lei, M., Wang, Y. (2013) One-step synthesis of easy-recycling TiO_2-rGO nanocomposite photocatalysts with enhanced photocatalytic activity. Applied Catalysis B: Environmental 132-133:452-459.

Wojtoniszak, M., Zielinska, B., Chen, X., Kalenczuk, R.J., Borowiak-Palen, E. (2012) Synthesis and photocatalytic performance of TiO_2 nanospheres–graphene nanocomposite under visible and UV light irradiation. Journal of Materials Science 47:3185-3190.

Xu, X., Xu, Y., Zhu, J. (2014) Photocatalytic antifouling graphene oxide-mediated hierarchical filtration membranes with potential applications on water purification. ACS Applied Materials & Interfaces 6:16117-16123.

Zalazar C.S., Lovato M.E., Labas M.D., Brandi R.J., Cassano A.E. (2007) Intrinsic kinetics of the oxidative reaction of dichloroacetic acid employing hydrogen peroxide and ultraviolet radiation. Chemical Engineering Science 62:5840-5853.

Zhang, Z., Yang, W., Zou, Z., Xu, F., Wang, X., Zhang, B., Tang, J. (2012) One-pot, solvothermal synthesis of TiO_2-graphene composite nanosheets. Journal of Colloid and Interface Science 386:198-204.

CHAPTER 4

ROLE OF NOBLE METALS AS TiO_2 CO-CATALYSTS FOR DCA DEGRADATION

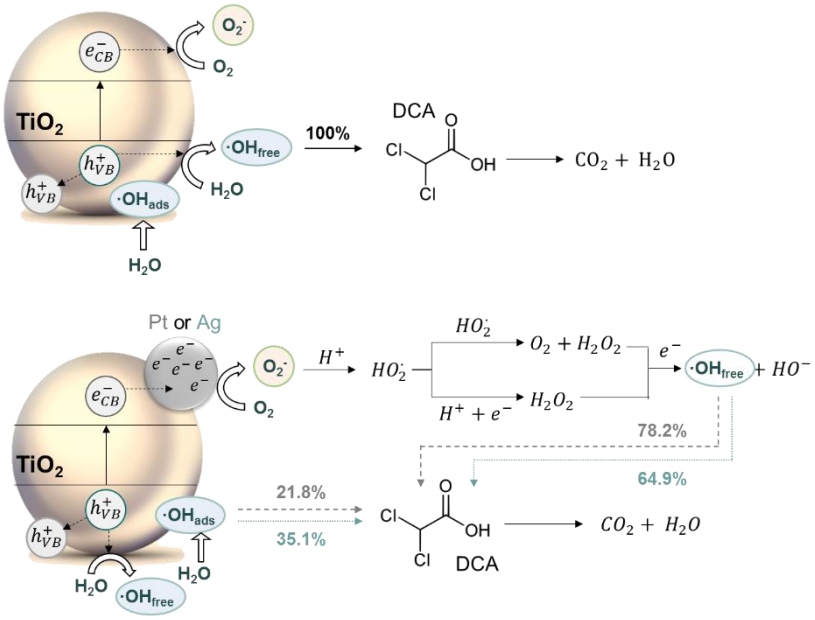

As it was highlighted in Chapter 3, there is an increasing demand for TiO_2-based photocatalysts due to the growing need to mitigate environmental problems related to organic water pollution.

The photocatalytic mechanism of TiO_2 involves absorbing a photon with energy equal or greater to its band gap (3.2 eV) and exciting an electron from the valence band (h^+_{VB}) to the empty conduction band (e^-_{CB}). The photonic excitation leaves behind an unfilled valence band, thus creating the electron-hole pair. These charge carriers, with sufficient reductive/oxidative power, can react with the surrounding oxygen-containing species, such as dissolved oxygen or H_2O (OH^-), to produce reactive oxygen species (ROS) (4.1) - (4.7) (Chong *et al.*, 2010; Lee and Park, 2013; Liao *et al*., 2013; Schneider *et al*., 2014; Marinho *et al*., 2017).

Photoexcitation: $TiO_2 + h\upsilon \rightarrow e^-_{CB} + h^+_{VB}$ (4.1)

Charge-carrier trapping of e^-: $e^-_{CB} \rightarrow e^-_{TR}$ (4.2)

Charge-carrier trapping of h^+: $h^+_{VB} \rightarrow h^+_{TR}$ (4.3)

Electron-hole recombination: $e^-_{TR} + h^+_{VB}\left(h^+_{TR}\right) \rightarrow$ heat (4.4)

Photoexcited e^- scavenging: $e^-_{CB} + O_2 \rightarrow O_2^{\cdot-}$ (4.5)

Oxidation of hydroxyls: $h^+_{VB} + OH^-_{ads} \rightarrow \cdot OH_{ads}$ (4.6)

Oxidation of water: $h^+_{VB} + H_2O \rightarrow \cdot OH_{free}$ (4.7)

Superoxide radicals ($O_2^{\cdot-}$), hydroxyl radicals ($\cdot OH_{free}$ and $\cdot OH_{ads}$), and valence band holes (h^+_{VB}) are the main reactive species involved in organic pollutant degradation. However, the mechanistic implication of these species in photocatalytic processes is still under discussion.

Photocatalytic reactions over TiO_2 are strongly dependent on its surface and interfacial properties with recombination, trapping, and interfacial transfer of charge carriers being very fast processes. However, the rate of interfacial charge transfer to surrounding oxygenated species is much slower than the rate of charge recombination in the bulk, and on the surface of the catalyst. Therefore, if the interfacial charge transfer rates are not greatly improved, the recombination of interfacial loads proceeds rapidly. Charge carrier movements and the photocatalytic activity of TiO_2 can be improved by employing strategies that prevent bulk and surface charge recombination and enhance charge transport to the surface sites of TiO_2. These include decreasing the defect sites in the bulk and on the surface, increasing the accessible surface area, loading a co-catalyst, and constructing heterojunctions and nanostructured photocatalysts (Wen *et al.*, 2015).

Apart from the use of GO to improve the performance of TiO_2, applying noble metal-TiO_2 nanocomposite structures is under discussion.

As it was remarked in Chapter 1, noble metal (NM) clusters improve the photocatalytic activity owing to Fermi level equilibration, which results in Schottky barrier formation (Ziylan-Navas *et al*., 2015). This barrier serves as an effective trap where electrons are unable to flow back to the semiconductor (Khan *et al*., 2015). Furthermore, noble metal nanoparticles show localized surface plasmon resonance (LSPR) effect (Verbruggen *et al*., 2014; Gou *et al*., 2015). Metal nanoparticles can enhance the photoactivity of nearby semiconductors transferring charge carriers from the photoexcited metal to the semiconductor, increasing the rates of electron-hole pair formation in the semiconductor due to plasmon resonance energy transfer effect (PRET), and scattering of resonant photons (Ingram *et al*., 2011; Khan *et al*., 2015; Zhang *et al*., 2015; Devi and Kavitha, 2016). Considering the suitable photocatalytic activity of TiO_2/GO composites demonstrated in Chapter 3, GO nanosheets coupled

with nanoparticles of TiO_2 and noble metals are expected to provide enhanced photocatalytic properties due to the ability of GO to carry charges. Moreover, the addition of a third co-catalyst in TiO_2/NM photocatalysts could reduce the amount of noble metal and, therefore, its cost while maintaining the positive characteristics. GO nanosheets could contribute to the photogenerated electron movements and noble metals could act as electron sink; therefore, a reduction in electron-hole pair recombination process, and thus an enhanced photocatalytic activity, could be expected.

This chapter explores novel TiO_2-based photocatalyst materials using silver and platinum as co-catalysts. The influence of the noble metal loading on the TiO_2 and TiO_2/GO and the ability of GO nanosheets to improve the photocatalytic activity were studied. The performance of the novel photocatalysts was evaluated against DCA degradation as a model compound. Moreover, the design of novel materials and an in-depth analysis of reaction mechanisms are among the scientific challenges that should be addressed before the full deployment of DCA photocatalytic degradation. This work therefore explores the role of ROS under UV-Vis light activated TiO_2 catalysts doped with silver and platinum using selected chemical scavengers with the aim of gaining insight into the degradation pathways attributed to different properties of photocatalysts.

4.1. Photocatalysts characterization

The previous chapter of this thesis stated that doping TiO_2 with 5 wt% of GO via the hydrothermal method (H5%) resulted in the best photocatalytic performance against DCA degradation among the studied procedures. For this reason, in this chapter the GO-based photocatalysts present 5 wt% of GO respect to total mass of TiO_2/GO and they have been prepared via the hydrothermal method.

TEM images of TiO_2/Pt 0.5%, TiO_2/Ag 10%, TiO_2/GO/Pt 0.5%, and TiO_2/GO/Ag 10% photocatalysts are shown in Figure 4.1. Figure 4.1-A1 and Figure 4.1-A3 show small dark noble metal nanoparticles of Pt dispersed on the surface of the TiO_2 and TiO_2/GO surfaces, respectively. The lighter areas correspond to TiO_2 nanoparticles, and the darker ones correspond to the noble metal. In the case of the composites with Ag nanoparticles (Figure 4.1-A2 and Figure 4.1-A4), the presence of this noble metal in the solid structures is not easily identified. This may be because silver is unstable over time, and therefore, its detection is difficult via TEM and EDX analysis. The presence of platinum nanoparticles in the binary and ternary composites was further evidenced by EDX measurements (Figure 4.1-B1 and Figure 4.1-B3). Ag-doped composites also presented metallic Ag peaks in the EDX spectra (Figure 4.1-B2 and Figure 4.1-B4); however, silver was not as well dispersed as platinum in the correspondent composites.

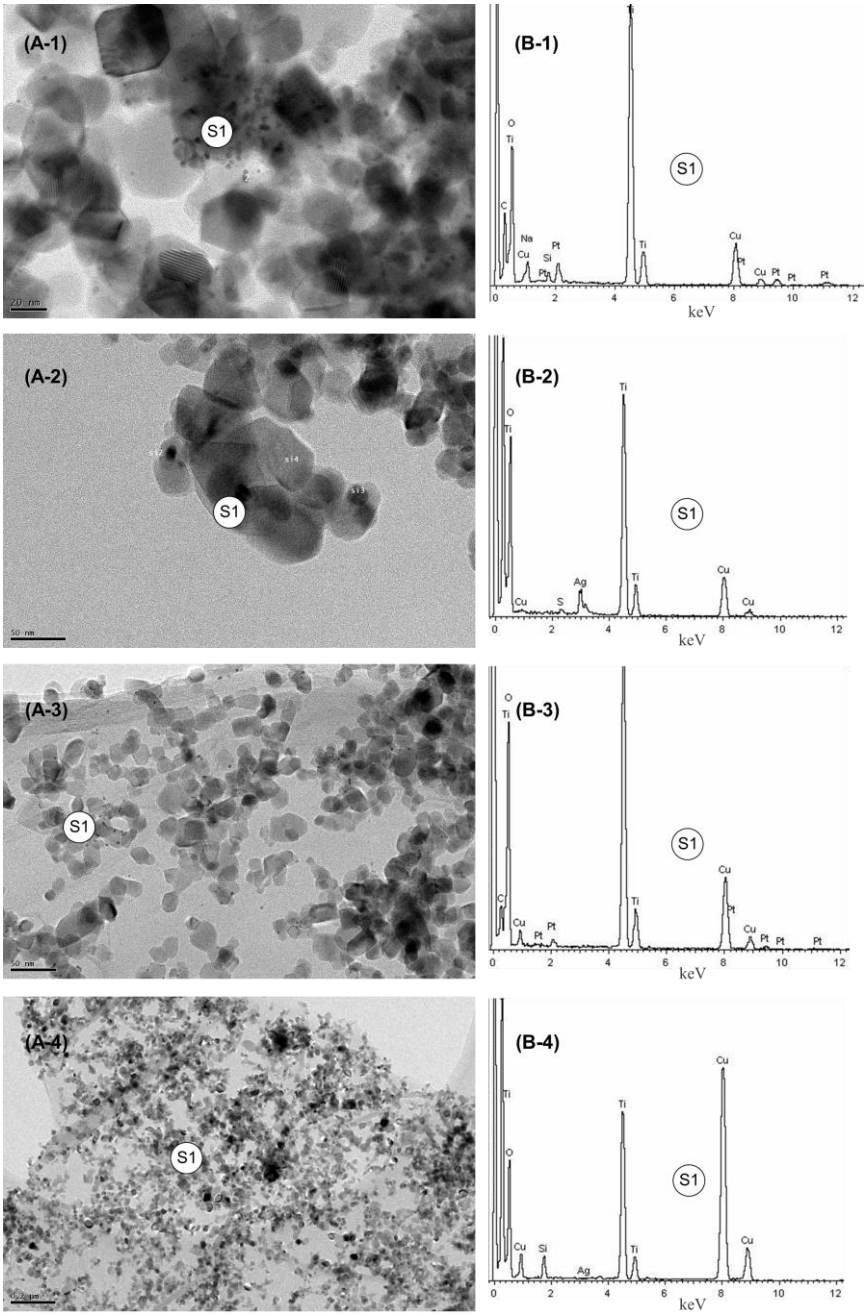

Figure 4.1 TEM images (A) and EDX analysis (B) of TiO_2/Pt 0.5% (1), TiO_2/Ag 10% (2), TiO_2/GO/Pt 0.5% (3), and TiO_2/GO/Ag 10% (4).

Figure 4.2 shows the FTIR spectra of the TiO_2, GO, TiO_2/GO/Pt 0.5%, and TiO_2/GO/Ag 10% samples. The GO spectrum shows many strong absorption peaks that are related to various oxygen functional groups as already explained in Figure 3.3. In the TiO_2/GO/Pt and TiO_2/GO/Ag spectra, the intensity of all absorption peaks corresponding to oxygen functional groups presented a significant decrease compared to those in the GO spectra, implying that GO was significantly reduced during the synthesis step. In addition, the broad bands between 500-900 cm^{-1} are related to Ti-O-Ti and Ti-O-C stretching vibration. Therefore, the above results confirmed the successful preparation of TiO_2/GO composites via thermal treatment and the stability of GO nanosheets after the polyol synthesis process. FTIR spectra of TiO_2/GO/Ag and TiO_2/GO/Pt composites do not show any band corresponding to the noble metals due to the low loading of the deposited metals.

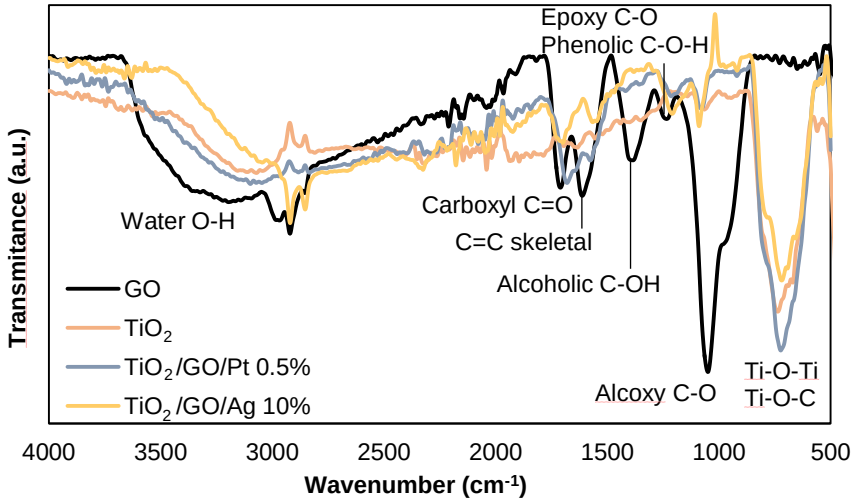

Figure 4.2 FTIR spectra of GO, TiO_2, TiO_2/GO/Pt 0.5%, and TiO_2/GO/Ag 10% photocatalysts.

The presence of GO and TiO_2 in the synthesized composites was further proven by Raman spectroscopy (Figure 4.3). Four peaks, which

correspond to the anatase crystalline phase were observed in ternary photocatalysts. In addition, two extra peaks were observed at 1353 cm^{-1} (D peak) and 1576 cm^{-1} (G peak), confirming the presence of GO in the samples. The area under the D curve increased relative to the pristine GO sample as observed in the TiO_2/GO spectrum (Table 4.1), suggesting the formation of more sp^3 defects in the carbon structure. However, in TiO_2/GO/Pt and TiO_2/GO/Ag photocatalysts the area under the D curve decreased (Table 4.1). The possible reason for the decreased sp^3 defects in ternary photocatalysts can be attributed to the reduction caused by the polyol synthesis method that removes the remaining oxygen groups on the GO surface. Noble metals deposited on TiO_2/GO structures did not provide a specific signal in the Raman analysis.

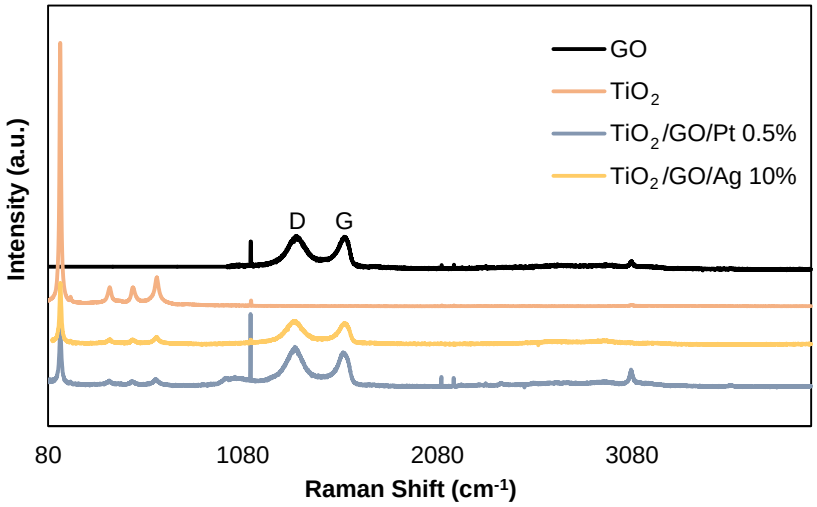

Figure 4.3 Raman spectroscopy of GO, TiO_2, TiO_2/GO/Pt 0.5%, and TiO_2/GO/Ag 10% photocatalysts.

Table 4.1 Values of specific parameters of Raman spectra (Figure 4.3).

Sample	D Area	Frequency		FWHM	
		D peak	G peak	D peak	G peak
GO	91311	1356	1584	116	65
TiO_2/GO	146484	1353	1576	158	105
TiO_2/GO/Pt	8134	1347	1601	112	65
TiO_2/GO/Ag	66599	1345	1599	115	61

XRD analyses were performed to analyze the crystal phases of the GO, TiO_2/GO, TiO_2/Ag, and TiO_2/Pt solids (Figure 4.4). A diffraction peak at a 2Θ value of approximately 11.3º was observed in the GO curve, indicating the possible existence of trapped water between the layers of the hydrophilic GO. No diffraction peaks of GO were observed in the TiO_2/GO composites because the regular stacking of the GO was destroyed by the intercalation of TiO_2 (Liu *et al*. 2013). All composites presented the characteristic crystal planes of anatase and rutile phases. This means that the TiO_2 structure was not substantially modified by the addition of noble metals or GO nanosheets. Moreover, two diffraction peaks corresponding to the (111) and (200) facets of platinum (JCPDS 65-2868) were observed in the TiO_2/Pt curve, supporting the presence of this noble metal in the composite. In the case of the TiO_2/Ag curves, several diffraction peaks were observed. These peaks correspond to Ag_3O_4, indicating that the metallic form is not the most relevant for Ag. This fact agrees with the TEM images, where metallic Ag was hardly observed.

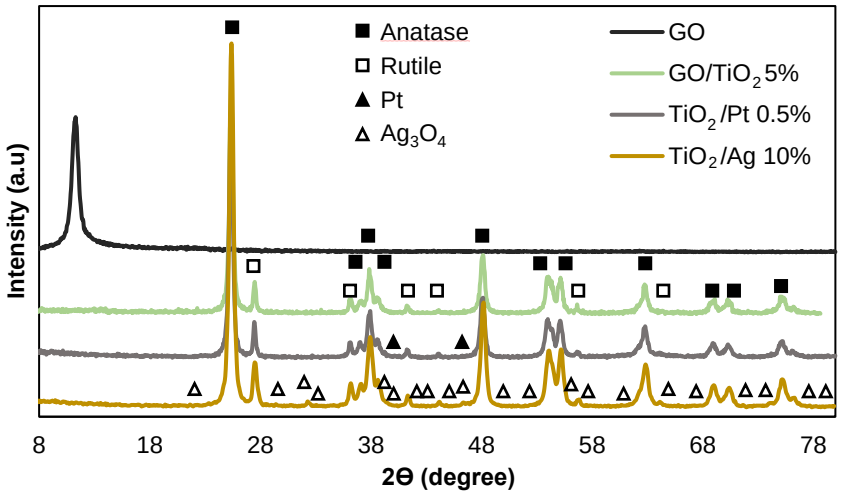

Figure 4.4 XRD patterns of GO, TiO_2/GO 5%, TiO_2/Pt 0.5% and TiO_2/Ag 10%.

The surface compositions and elemental chemical states of TiO_2, TiO_2/Pt and TiO_2/Ag were characterized using XPS. Figure 4.5-A shows two XPS peaks of Ti $2p_{3/2}$ and Ti $2p_{1/2}$ of Ti at 458.9 eV and 464.5 eV, respectively, in accordance with the binding energy of Ti^{4+} in TiO_2. Apart from the two peaks corresponding to Ti^{4+}, the TiO_2/Pt photocatalyst presented two peaks of Pt $4f_{7/2}$ and Pt $4f_{5/2}$ at 70.5 and 73.8 eV, respectively, with a splitting energy of 3.3 eV (Figure 4.5-B), indicating the existence of metallic Pt (Wang *et al.*, 2015). Moreover, two additional peaks were observed at 72.1 and 75.4 eV attributed to Pt $4f_{7/2}$ and Pt $4f_{5/2}$ related to Pt^{2+} states. This fact might be attributed to the formation of Pt-O bond on the TiO_2 surface, or metallic Pt atoms thermally diffusing into the TiO_2 crystal lattice and oxidized to Pt^{2+} to substitute Ti^{4+} or form the interstitial ions (Hsieh *et al*., 2015). The XPS spectrum of TiO_2/Ag (Figure 4.5-C) exhibits Ag 3d states in the catalyst surface. Specifically, peaks located at 364.65 eV and 370.29 eV correspond to the binding energy of Ag $3d_{5/2}$ and Ag $3d_{3/2}$, respectively. This typical deviation (6 eV) of the binding energy between Ag $3d_{5/2}$ and $3d_{3/2}$ is characteristic of silver (Gao

et al., 2015). However, these values are lower than the binding energies of metallic Ag (367.9 and 373.9 eV for Ag $3d_{5/2}$ and Ag $3d_{3/2}$, respectively) and thus, they can be attributed to Ag^{1+}. Therefore, the Ag metallic form is not the predominant one, as already verified by TEM and XRD analysis.

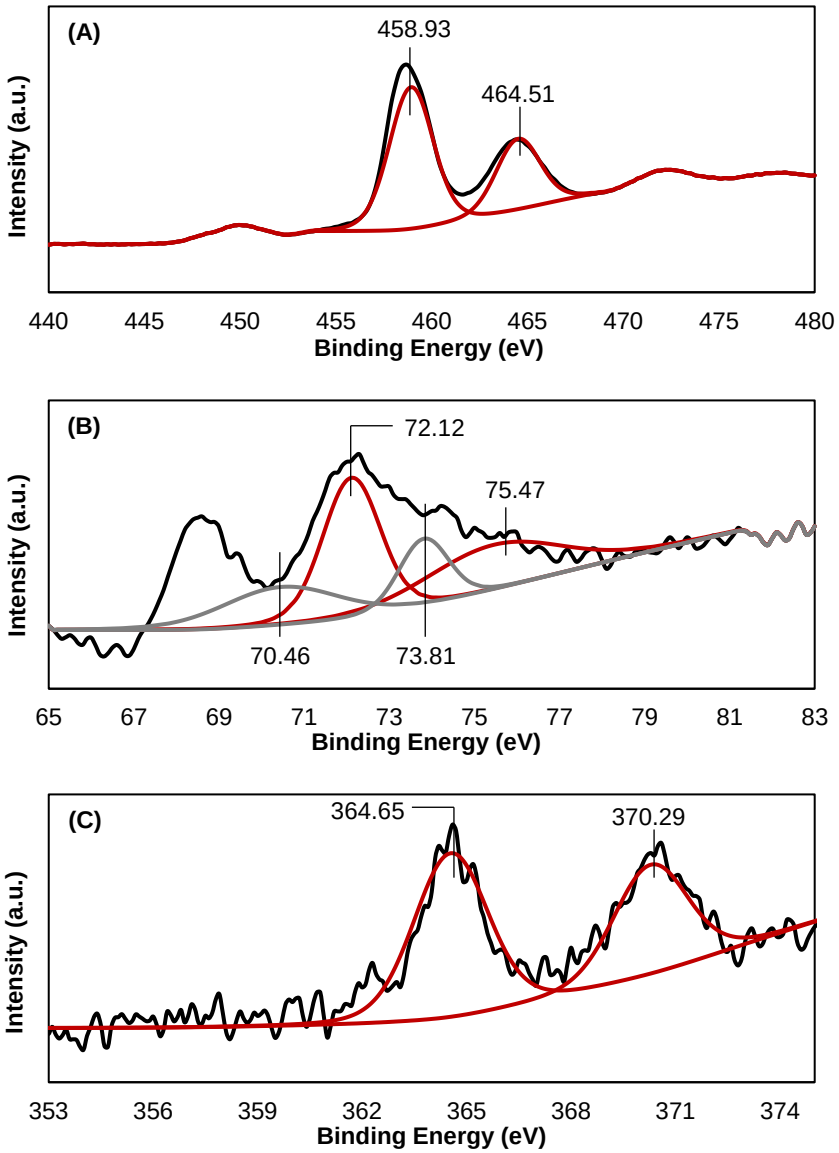

Figure 4.5 High-resolution XPS spectra of TiO_2 (A), TiO_2/Pt 0.5% (B) and TiO_2/Ag 10% (C) photocatalysts.

Photocurrent response measurements were carried out to evaluate the photogenerated charge transport in the synthesized photocatalysts. The photocurrent response was reversible as the illumination was turned on and off to analyze the photocurrent induced by light irradiation in the solids, and a photocurrent parameter was defined as the normalized value of the difference between ON and OFF currents. Figure 4.6 shows the photocurrent parameter for TiO_2, TiO_2/GO 5%, TiO_2/Pt 0.5%, and TiO_2/Ag 10%. The bare TiO_2 nanoparticles do not present a photocurrent response because the light source mainly emits in the visible range, while the synthesized photocatalysts showed photocurrent response. The TiO_2/Pt 0.5% catalyst exhibited the best value according to the photocurrent parameter; therefore. The TiO_2/GO 5% and TiO_2/Ag 10% composites presented similar photocurrent values, 38% and 35% lower than that of TiO_2/Pt, respectively. Therefore, these photocatalysts are expected to exhibit lower activity during DCA degradation. Thus far, the improved photoresponse of TiO_2-doped composites can presumably be considered to benefit the photocatalytic activity.

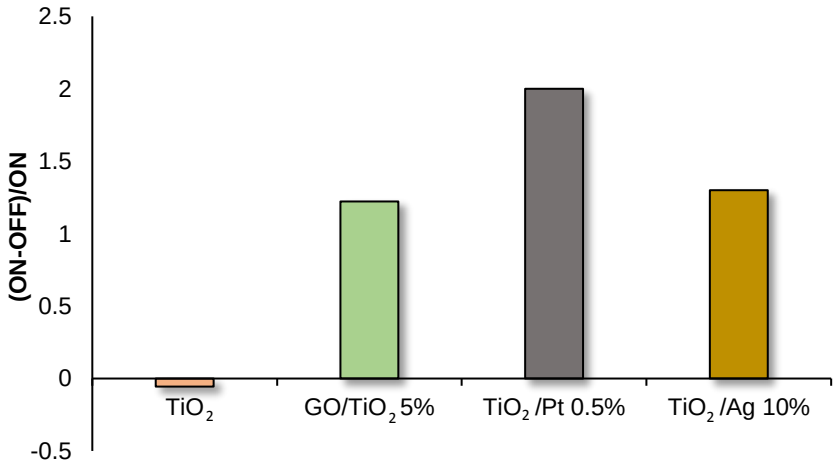

Figure 4.6 Photocurrent parameters for TiO_2, TiO_2/GO 5%, TiO_2/Pt 0.5%, and TiO_2/Ag 10% photocatalysts under visible light.

4.2. Photocatalytic performance of TiO_2/NM and TiO_2/GO/NM photocatalysts

As in the previous chapter, DCA solutions were employed to study the photocatalytic activity of the synthesized photocatalysts under UV-Vis light. Dark adsorption experiments of the DCA onto the solids were carried out and no significant adsorption of DCA was noticed.

Figure 4.7 shows the degradation of DCA after eight hours of treatment under UV-Vis light for all photocatalysts. Additionally, the experimental data on DCA degradation were fitted to a zero-th order kinetic model. Among all the studied photocatalysts, commercial TiO_2 exhibited the lowest photocatalytic efficiency for DCA oxidation. By incorporating GO sheets, as it was concluded in the previous chapter, a degradation of 87.10% was achieved after 8 hours of treatment.

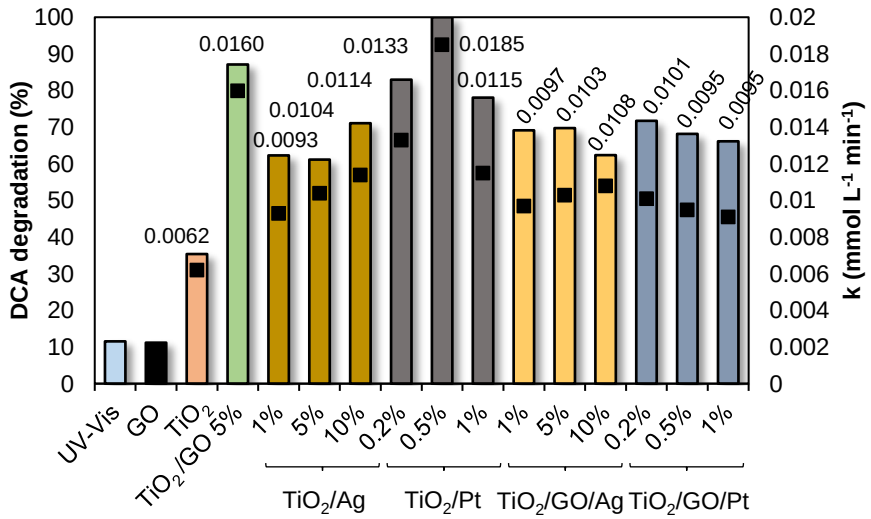

Figure 4.7 DCA degradation percentages after 8 hours of irradiation time and kinetic constants values for each photocatalyst. Conditions: UV-Vis light, $[DCA]_0$ = 1000 mg L^{-1}, [Catalyst] = 0.3 g L^{-1}, T = 20ºC.

Figure 4.8 shows the possible mechanisms responsible for the improved performance associated to doping TiO_2 with noble metal nanoparticles. These metals doped on the TiO_2 surface create a Schottky barrier at the TiO_2/NM interface, which can serve as an effective electron trap, preventing the backflow of electrons to the TiO_2. The height of this barrier increases with the difference between the work functions of noble metals and TiO_2.

However, the Schottky barrier does not play an important role under visible light because TiO_2 is not able to be excited. The more favorable use of visible light can be due to the LSPR effect, which can influence the photocatalytic activity via the following three mechanisms: photon scattering, plasmon resonance energy transfer (PRET) and electron transfer from the noble metal to TiO_2 (Khan *et al*. 2015; Zhang *et al*. 2015). Because the photon scattering mechanism only changes the optical paths of the photons and the injection of electrons from the metal nanoparticle to the semiconductor opposes the Schottky barrier's natural tendency, only the PRET mechanism can enhance the photocatalytic activity under visible light. It is based on the radioactive decay of the surface plasmonic states that excite electrons in TiO_2, increasing the electron-hole pair generation.

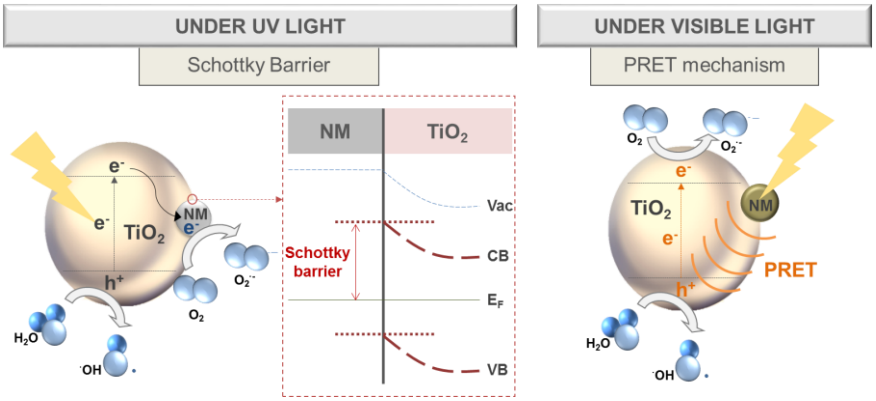

Figure 4.8 Possible mechanisms responsible of the improved photocatalytic activity improvement due to noble metals.

After covering the TiO_2 surface with noble metal nanoparticles, the photocatalytic activity was improved with respect to that of bare TiO_2. The experimental results showed that TiO_2/Pt composites reported the best photoactivity among the NM-doped photocatalysts, achieving total degradation using TiO_2/Pt 0.5% after 7 hours. In the case of silver-doped composites, only 71% degradation is reached using TiO_2/Ag 10% after 8 hours of irradiation time. As the work function of platinum (-5.65 eV) is higher than that of silver (-4.7 eV), the TiO_2/Pt junction has a larger Schottky barrier capable of transferring electrons more efficiently under UV irradiation. Additionally, under visible light, the PRET mechanism can influence the photocatalytic activity improvement.

Regarding the influence of the noble metal load in the photocatalysts, Pt-doped composites with an intermediate concentration of 0.5% provided the best results. With higher metal loadings, the electron transfer can also deform the potential field in the TiO_2 nanoparticles and draw a portion of the holes toward the metal/TiO_2 junction, which increases the recombination rate (Devi and Kavitha, 2016). Moreover, high concentrations of the deposited metal can act as a shield for the absorption of photons. Nevertheless, in the case of Ag-doped composites, the highest metal load provided the best DCA degradation and mineralization results. The XRD analysis and TEM images showed that the metallic silver is not very well dispersed on TiO_2 surface. Therefore, when more silver precursor is used, a larger number of metallic silver nanoparticles are presumably capable of being deposited, improving the photocatalytic activity.

TiO_2/GO/NM ternary composites presented better photocatalytic performance than commercial TiO_2; however, their photocatalytic activity was worse than that of TiO_2/GO and not always better than TiO_2/NM photocatalysts. A photocatalytic degradation of DCA close to 70% using TiO_2/GO/Ag 1% and TiO_2/GO/Ag 5% was obtained. However, the composites without GO achieved approximately 61% degradation after 8

hours of irradiation with TiO_2/Ag 1% and TiO_2/Ag 5%. Increasing the concentration of silver up to to 10% does not improve the photocatalytic performance of the ternary composites; besides the photo-oxidation yield was reduced from 71% for TiO_2/Ag 10% to 62.3% for TiO_2/GO/Ag 10%. This may be due to the stress induced by the higher Ag content deposited on the TiO_2/GO, which leads to a greater number of defects in the lattice symmetry. Ternary composites formed by TiO_2, GO and Pt nanoparticles always exhibited worse photocatalytic activity than the binary TiO_2/Pt composites. GO nanosheets may hinder the electron transfer to the platinum and may act as charge carrier recombination centers. Therefore, we conclude that GO is an excellent option for TiO_2 binary composites, despite being less photoactive than Pt, but it is not suitable for ternary composites with TiO_2 and noble metals for the removal of DCA aqueous solutions. On the other hand, the TiO_2/GO/Pt photocatalyst provides worse performance than the binary TiO_2/Pt probably due to the use of non-optimized GO loading for ternary catalysts. Furthermore, analysis of DCA mineralization based on changes in DOC revealed that the measured values matched undegraded DCA (Figure 4.9). Therefore, practically total mineralization was achieved using the synthesized photocatalysts.

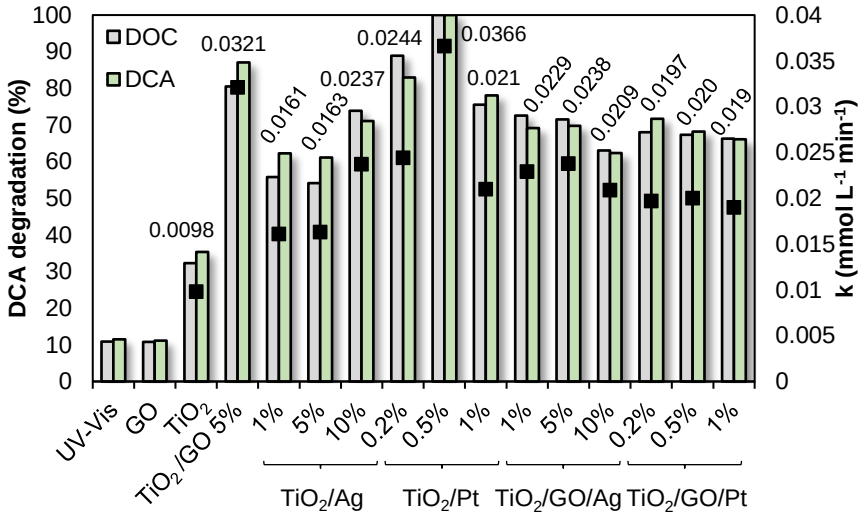

Figure 4.9 DCA and DOC removal after 8 hours of irradiation time and DOC kinetic constants values for each photocatalyst. Conditions: UV-Vis light, $[DCA]_0$ = 1000 mg L^{-1}, $[DOC]_0$ = 148 mg L^{-1}, [Catalyst] = 0.3 g L^{-1}, T = 20ºC.

The use of ternary and binary photocatalysts based on TiO_2, noble metals and graphene oxide has been reported in the literature for environmental applications (Table 4.2).

Table 4.2 TiO_2-noble metal photocatalyts for pollutant transformation.

Author	Catalyst	Light	Pollutant	Main results
Grabowska *et al*., 2016	TiO_2-Ag TiO_2-Pt TiO_2-Au TiO_2-Pd	UV-vis	Toluene Phenol	UV: 0.1wt% of NM Vis: 0.1 wt% of NM UV: 1 wt% of NM Vis: 0.5 wt% of NM
Li *et al*., 2016	Ag-TiO_2 Pd-TiO_2 Pt-TiO_2	UV-vis	PFOA*	Pt-TiO_2 > Pd-TiO_2 > Ag-TiO_2 > TiO_2
Vaiano *et al*., 2016	Au-TiO_2 Pt-TiO_2	UV	PB V**	Au-TiO_2 > Pt-TiO_2
Tan *et al*., 2015	GT-Pt GT-Pd GT-Ag GT-Au	Visible	CO_2	GT-Pt > GT-Pd > GT-Ag > GT-Au > GT > P25
Wang *et al*., 2015	TiO_2-Ag TiO_2-Pt	UV	CO_2	TiO_2-Ag > TiO_2-Pt > TiO_2
Ismail *et al*., 2013	Au-TiO_2 Pt-TiO_2 Pd-TiO_2	UV	Methanol	Pd-TiO_2 > Pt-TiO_2 > Au-TiO_2 > P25
Liu *et al*., 2013	GO-TiO_2-Ag GO-TiO_2 GO-Ag	Solar simulator	Phenol AO-7***	GO/TiO_2/Ag 9.1 wt% > GO/TiO_2/Ag 13 wt% > GO/TiO_2/Ag 4.76 wt% > GO/TiO_2 > TiO_2
Ismail *et al*., 2011	Pt/TiO_2	UV-Vis	DCA	90% of degradation (90 min)

**PFOA: Perfluorooctanoic acid*
***PB V: Patent Blue V*
****AO-7: Acid Orange 7*

Ternary composites based on TiO_2, GO and noble metals (Pt, Pd, Au, Ag) were tested in CO_2 photoreduction under visible light (Tan *et al*., 2015). Among the noble metals studied, the Pt-doped ternary composite (with 2.0 wt% of Pt loading) demonstrated the best photoactivity. However, no comparison to TiO_2/noble metal binary photocatalysts was reported. The study developed by Wang and co-workers (2015) demonstrated the extremely high CO_2 photoreduction efficiency of photocatalysts based on TiO_2 and noble metals (Ag and Pt) under UV light. Although Pt deposited on the TiO_2 surface produces a higher Schottky barrier than that with deposited Ag, the photocatalytic activity results go against this theory, presenting the Ag-based materials the highest photocatalytic activity. Noble metals Pt, Pd and Ag modified TiO_2 photocatalysts have been also used for photocatalytic decomposition of perfluorooctanoic acid (PFOA) (Li *et al*., 2016). All the three noble metal-TiO_2 solids exhibited great photoactivity for PFOA decomposition, following the order: TiO_2/Pt > TiO_2/Pd > TiO_2/Au. Liu and co-workers (2013) developed multifunctional nanocomposites consisting of GO nanosheets, TiO_2 nanorods and Ag nanoparticles that showed remarkably enhanced photocatalytic degradation activities toward AO-7 and phenol degradation under solar irradiation compared with GO-TiO_2 and GO-Ag. Grabowska and co-workers (2016) studied TiO_2 microspheres loaded with noble metal nanoparticles (Au, Ag, Pt and Pd), analyzing different amounts of noble metals on the phenol degradation in aqueous phase under UV and visible light. It was noticed that, under UV light, 1 wt% of noble metal was profitable and in the visible-induced reaction, 0.5 wt% of noble metal was beneficial. Photocatalytic removal of the PB dye with noble metals (Au and Pt) based photocatalysts has been tested by Vaiano and co-workers (2016), observing that the presence of the noble metal on the TiO_2 surface enhanced the removal efficiency of the dye and that in particular the photocatalyst with gold showed better effectiveness for PB removal. Ismail and co-workers (2011) tested TiO_2/Pt 0.5 wt% photocatalyst under UV-vis

light for the degradation of DCA solutions. The photocatalytic activity was considerably increased by platinization of TiO_2, achieving a degradation of 90% after 90 minutes of irradiation time. Different noble metals deposited onto TiO_2 surface were assessed against methanol degradation under UV light in the work developed by Ismail and co-workers (2013). Photocatalytic activity behaved quite differently depending on the type of noble metals and the photocatalysts performance was in the order Pd > Pt > Au. Therefore, several results were reported depending on the co-catalyst amount, the noble metal used, the target compound, the light source and the photocatalyst synthesis method.

Finally, to assess the performance stability and reusability of the composites, the photo-oxidation of DCA was studied for three different cycles using the TiO_2/GO 5%, TiO_2/Pt 0.5%, and TiO_2/Ag 10% photocatalysts. The results are shown in Figure 4.10; all the catalysts were found to maintain stable photocatalytic activity, with a total loss of 4.3%, 2.7% and 1.8% after the third cycle for TiO_2/GO 5%, TiO_2/Pt 0.5%, and TiO_2/Ag 10% photocatalysts, respectively.

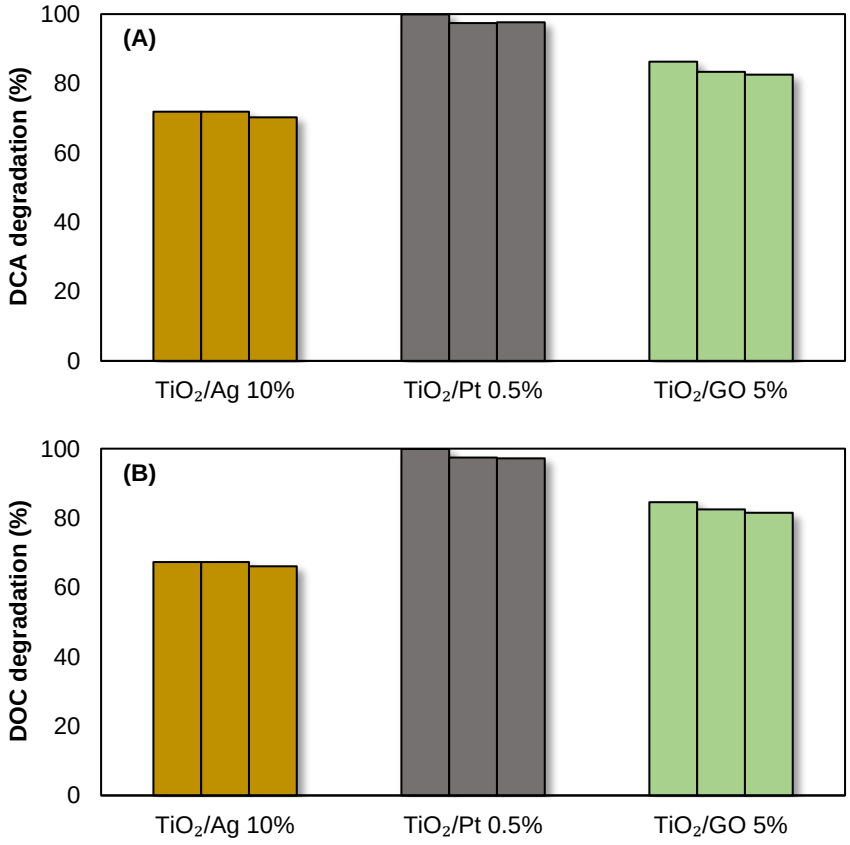

Figure 4.10 DCA degradation (A) and mineralization (B) over TiO_2/GO 5%, TiO_2/Pt 0.5%, and TiO_2/Ag 10% photocatalysts for three successive runs of 8 hours each.

4.3. Role of ROS on the activity of noble metal-doped TiO_2 photocatalysts

The influence of the $O_2^{\cdot-}$, $\cdot OH_{ads}$, $\cdot OH_{free}$ radicals and h^+_{VB} in the photocatalytic process, using the noble metal-doped TiO_2 photocatalysts that presented the best performance (TiO_2/Pt 0.5% and TiO_2/Ag 10%), was investigated through DCA degradation under UV-Vis light employing different scavengers. The excitation of the semiconductor provokes the generation of an empty unfilled valence band (h^+_{VB}) and photogenerated

electrons in the conduction band (4.1). In the valence band, the h^{+}_{VB} can react directly with the adsorbed hydroxide ion (OH^{-}) producing the $\cdot OH_{ads}$ radical (4.6), or with water molecules to form the $\cdot OH_{free}$ radical (4.7). Moreover, the h^{+}_{VB} can act directly as an active degradation species. Finally, the photogenerated electrons of the conduction band can result in $O_2^{\cdot-}$ radical formation through the reduction of oxygen molecules by electron transfer (4.5).

Benzoquinone (BQ) was used as scavenger to test the role of $O_2^{\cdot-}$ radicals in the photocatalytic degradation because it acts as a more efficient electron scavenger than molecular oxygen owing to its rather high inherent electron affinity. Therefore, BQ readily scavenges electrons at the surface of TiO_2 to form hydroquinone (HQ) (Henderson and Shen, 2017), avoiding the formation of $O_2^{\cdot-}$ radicals according to the equation (4.8).

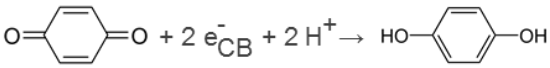

(4.8)

In order to evaluate the role of $\cdot OH_{free}$ in the photocatalytic process, tert-butanol (t-BuOH) was used as it is very good at trapping $\cdot OH_{free}$ radicals due to the fact that it generates inert intermediates as shown in equation (4.9) (Cavalcante *et al*. 2016).

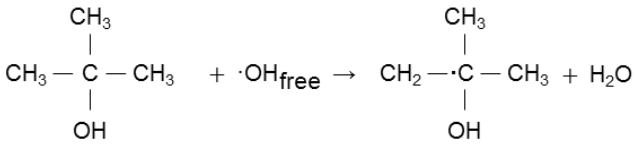

(4.9)

Finally, formic acid (FA) was employed to assess the participation of the $\cdot OH_{ads}$, $\cdot OH_{free}$ and h^{+}_{VB} radicals due to its large capacity to be adsorbed

onto the surface of the catalyst under acidic conditions and suppress the h^+_{VB}, inhibiting $\cdot OH_{free}$ and $\cdot OH_{ads}$ processes (Hirakawa *et al*. 2007).

$$HCOO^- + 2h^+_{VB} \rightarrow CO_2 + H^+ \quad (4.10)$$

$$HCOO^- + \cdot OH_{free} \rightarrow CO_2^- + H_2O \quad (4.11)$$

As dark adsorption experiments of DCA onto the catalysts surface were carried out without significant adsorption, direct degradation due to h^+_{VB} was ruled out for all photocatalysts.

Figure 4.11-A shows the results of the addition of BQ, t-BuOH and FA to the photocatalytic degradation medium of DCA using bare TiO_2 as catalyst. No inhibition was observed when $O_2^{\cdot -}$ radicals were removed by BQ, indicating that these species do not participate in the photocatalytic degradation process. However, when t-BuOH or FA were added to the DCA solution, total inhibition was observed. Since the role of h^+_{VB} was not remarkable due to its low adsorptive ability, together with the fact that the same inhibition was observed when either $\cdot OH_{free}$ or both $\cdot OH_{free}$ and $\cdot OH_{ads}$ were extracted, it was concluded that the $\cdot OH_{free}$ radicals play the most important role in DCA degradation when TiO_2 is used as catalyst. In order to substantiate these results, Figure 4.11-B shows the influence of scavenger molecules addition in the generation of $\cdot OH_{free}$ radicals. No decrease in the generation of $\cdot OH_{free}$ radicals was observed when BQ was added, but when FA was added the concentration of $\cdot OH_{free}$ was almost negligible.

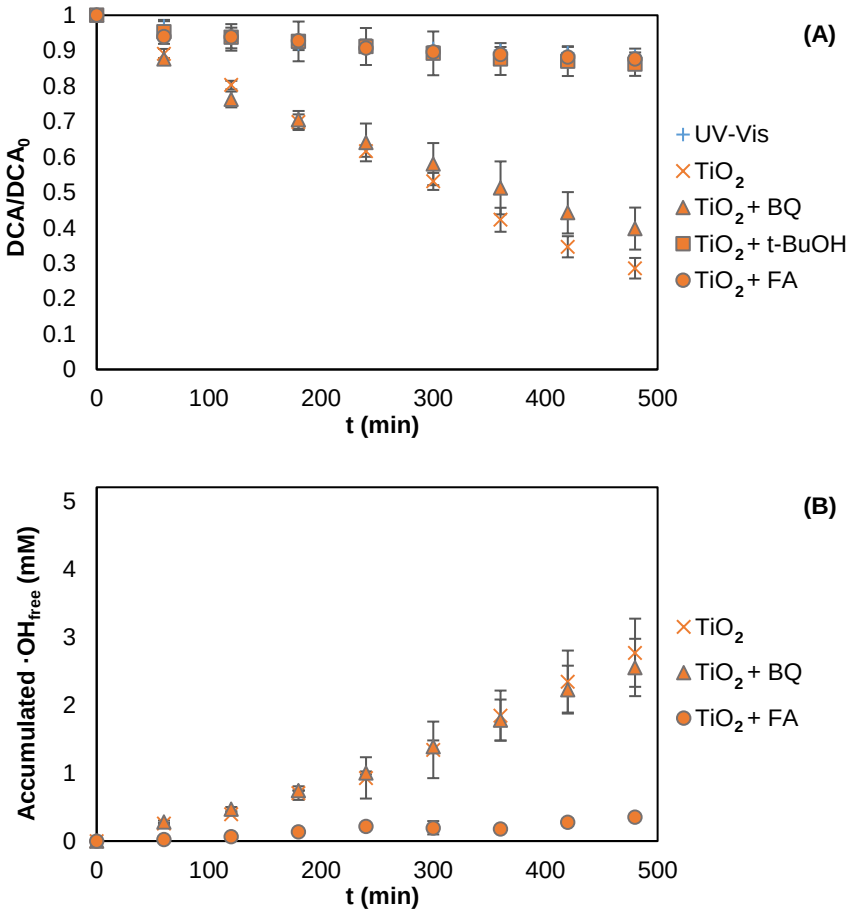

Figure 4.11 Effect of BQ, t-BuOH and FA addition on the photocatalytic degradation of DCA (A) and ·OH generation (B) for bare TiO_2.

In order to investigate the improved performance of TiO_2/Pt, Figure 4.12-A shows the effects of BQ, t-BuOH and FA addition to the DCA degradation medium. A remarkable inhibition of the photocatalytic activity was seen when $O_2^{\cdot-}$ radicals were removed, contrary to the behavior observed with TiO_2 under the same conditions. A similar trend for DCA degradation was observed adding t-BuOH to trap $\cdot OH_{free}$ radicals. Moreover, the photocatalytic activity was suppressed when FA consumed $\cdot OH_{ads}$, $\cdot OH_{free}$ and h^+_{VB} radicals. On the basis of the data obtained with

TiO_2/Pt, the results seem to indicate that $O_2^{\cdot-}$ radicals are critical in the degradation process through disproportionation to H_2O_2 and the formation of $\cdot OH_{free}$ (4.12) - (4.16) (Hoffman *et al*., 1995; Hirakawa *et al*., 2007; Liu *et al*., 2012; Sahel *et al*., 2016). According to previous studies, reaction (4.16) is the main contributor to the production of $\cdot OH_{free}$ radicals from H_2O_2 (Hirakawa *et al.*, 2007).

$$O_2^{\cdot-} + H^+ \rightarrow HO_2^{\cdot} \quad (4.12)$$

$$HO_2^{\cdot} + HO_2^{\cdot} \rightarrow O_2 + H_2O_2 \quad (4.13)$$

$$HO_2^{\cdot} + H^+ + e^- \rightarrow H_2O_2 \quad (4.14)$$

$$H_2O_2 + e^- \rightarrow \cdot OH_{free} + HO^- \quad (4.15)$$

$$H_2O_2 + O_2^{\cdot-} \rightarrow \cdot OH_{free} + HO^- + O_2 \quad (4.16)$$

The difference between the inhibition observed with the addition of t-BuOH and that of FA, results in the direct contribution of the $\cdot OH_{ads}$ radicals since the involvement of h^+_{VB} was ruled out. Therefore, the degradation pathway using TiO_2/Pt was conducted mainly by free $\cdot OH_{free}$ radicals and, to a lesser extent, by $\cdot OH_{ads}$ radicals. In order to better understand these results, $\cdot OH_{free}$ radicals were quantified using TiO_2/Pt as the catalyst together with the scavenger molecules (Figure 4.12-B). When BQ was introduced into the DCA solution as an analysis tool for trapping $O_2^{\cdot-}$ radicals, there was a significant decrease in the photocatalytic generation of $\cdot OH_{free}$, supporting the assumption that the $O_2^{\cdot-}$ radicals were being transformed into $\cdot OH_{free}$ radicals (4.15) - (4.16) leaving, therefore, few $\cdot OH_{free}$ radicals in solution when the $O_2^{\cdot-}$ radicals were removed. A similar concentration of $\cdot OH_{free}$ radicals was detected when incorporating FA into the medium, meaning that $\cdot OH_{free}$ radicals were not photocatalytically generated when introducing BQ or FA. Finally, it should be noted that TiO_2/Pt generated 60.6% more $\cdot OH_{free}$ radicals than bare TiO_2 after 480

min. This can be attributed to the conversion of $O_2^{\cdot-}$ radicals to $\cdot OH_{free}$ radicals because platinum acts as an electron trap, making more electrons available for the photocatalytic process than with bare TiO_2, leading to a decrease in the recombination rate of e^--h^+ (4.4).

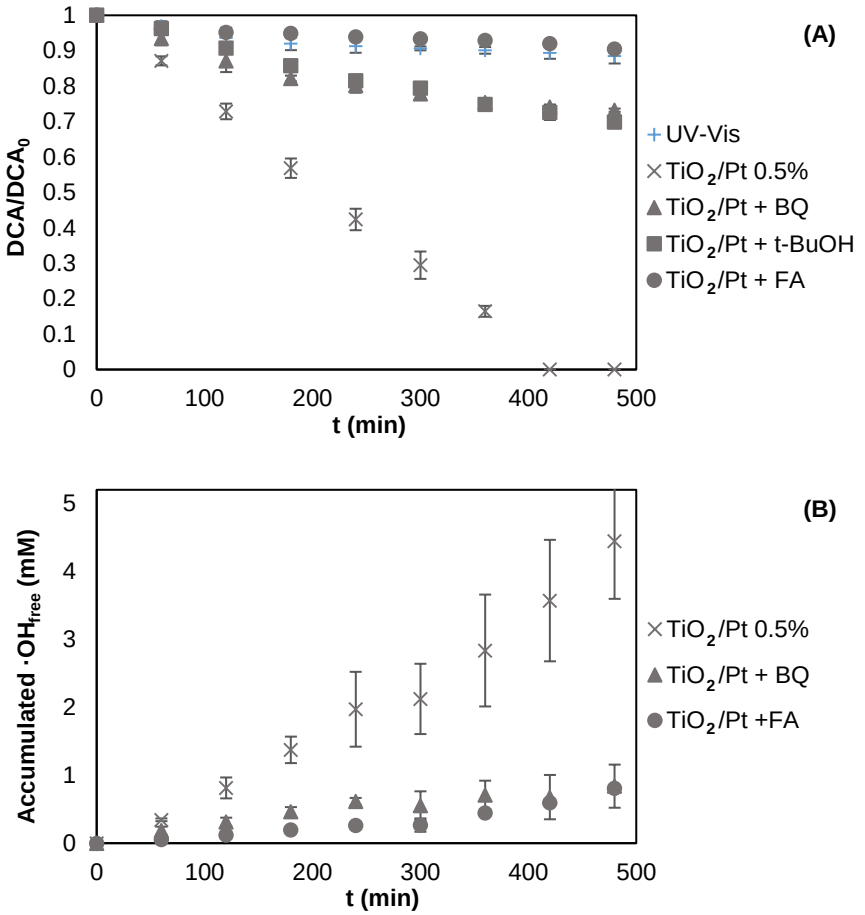

Figure 4.12 Effect of BQ, t-BuOH and FA addition on the photocatalytic degradation of DCA (A) and ·OH generation (B) for TiO_2/Pt.

The TiO_2/Ag catalyst was evaluated in order to compare the different ROS involved in DCA degradation depending on the noble metal used as dopant. Figure 4.13-A shows the influence on DCA degradation depending

on the scavenger added. Incorporating BQ or t-BuOH causes significant inhibition of the photocatalytic activity. Therefore, for silver-doped TiO_2 the major species involved in the degradation process are $\cdot OH_{free}$ radicals resulting from $O_2^{\cdot-}$ radical transformation. The TiO_2/Ag junction provokes the formation of the Schottky barrier, capable of efficiently transferring electrons from TiO_2 to Ag, providing electrons for the degradation. FA was used as a trapping molecule for $\cdot OH_{ads}$, $\cdot OH_{free}$ and h^+_{VB} radicals, as in previous studies, but an anomalous behavior was noted in the DCA degradation. Chloroacetic acid was detected as a reaction intermediate using TiO_2/Ag but not when using either TiO_2 or TiO_2/Pt. This intermediate appears through the hydrogenation reaction between FA and DCA catalyzed by Ag (Herron *et al*., 2014). Therefore, since the addition of FA modifies the DCA degradation pathway, it cannot be employed as scavenger when TiO_2/Ag is used as catalyst. The $\cdot OH_{free}$ radicals detected employing TiO_2/Ag (Figure 4.13-B) presented an intermediate value between those measured with TiO_2/Pt and TiO_2. $\cdot OH_{free}$ radicals were not photocatalytically generated when introducing BQ or FA into the reaction media, as it was seen in the analysis carried out with TiO_2/Pt.

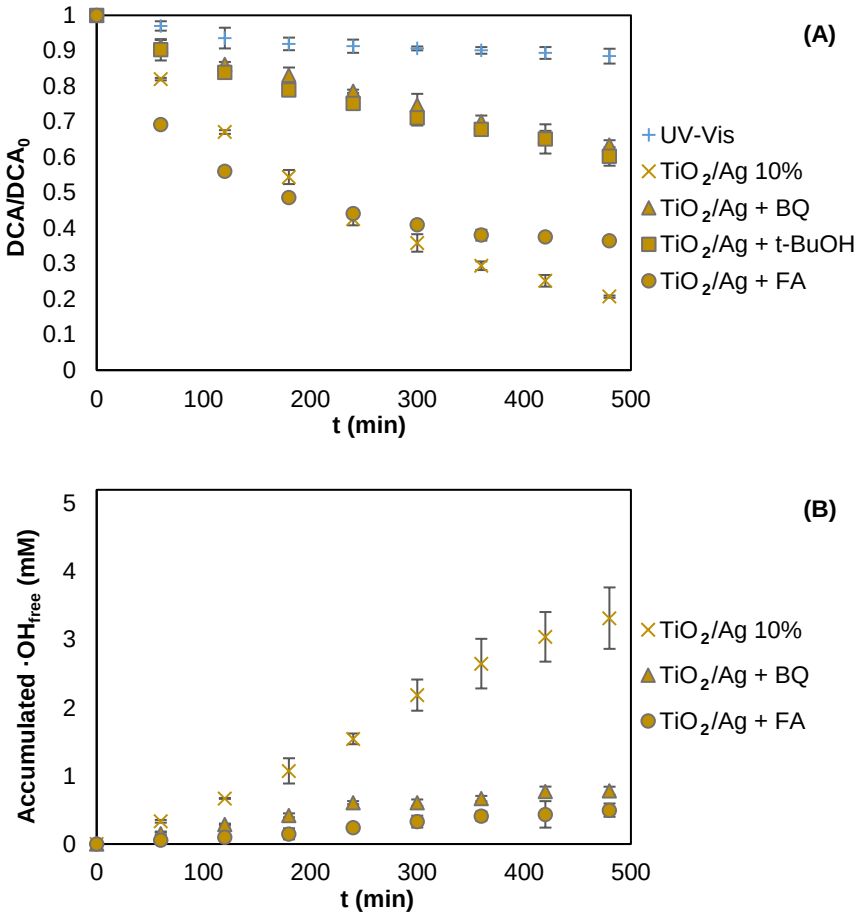

Figure 4.13 Effect of BQ, t-BuOH and FA addition on the photocatalytic degradation of DCA (A) and ·OH generation (B) for TiO_2/Ag.

H_2O_2 was quantified in order to verify the presence of this compound as an intermediate in the formation of $\cdot OH_{free}$ radicals (Figure 4.14). It can be observed that negligible concentrations of H_2O_2 were detected when TiO_2 was employed as photocatalyst; however, after two hours of irradiation time the presence of H_2O_2 was verified in the reaction media containing TiO_2/Pt and TiO_2/Ag photocatalysts and its concentration increased with time. As it can be observed, higher amounts of H_2O_2 were formed using TiO_2/Pt than using TiO_2/Ag. This fact may be related to the higher $\cdot OH_{free}$

radicals generation through H_2O_2 disproportionation using Pt-based photocatalyst compared to Ag-based photocatalyst.

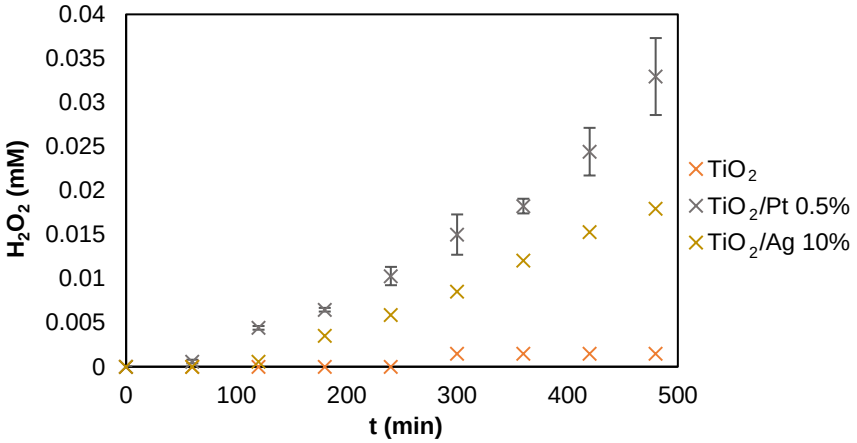

Figure 4.14 H_2O_2 quantification using TiO_2, TiO_2/Pt and TiO_2/Ag photocatalyst.

Since ROS formation could also depend on the rate of photon absorption by the catalyst in suspension, and different optical properties for noble metal-doped TiO_2 photocatalysts could be anticipated, the specific extinction coefficient (β_λ) has been calculated per unit of catalyst mass concentration applying a standard linear regression with forced intercept at the origin. Figure 4.15 depicts the extinction coefficient for each photocatalyst as a function of the wavelength. Lower values for the specific extinction coefficient were obtained for TiO_2/Pt and TiO_2/Ag compared to TiO_2. However, using noble metal-based materials better photocatalytic activity and different degradation pathways compared to bare TiO_2 were observed.

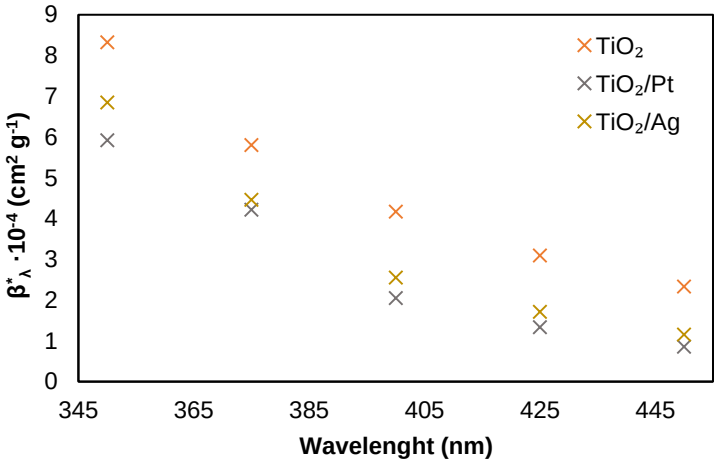

Figure 4.15. Specific extinction coefficient of TiO_2, TiO_2/Pt, and TiO_2/Ag samples as a function of the wavelength.

According to Cassano & Alfano (2000) the total extinction coefficient can be related to the absorption coefficient and the scattering coefficient through the following expression:

$$\beta_\lambda = \kappa_\lambda + \sigma_\lambda \quad (4.17)$$

where κ_λ is the absorption coefficient and σ_λ is the scattering coefficient. It can be concluded that from the optical point of view, TiO_2/Pt and TiO_2/Ag show properties both qualitatively and quantitatively similar but, in addition, TiO_2 has a quantitatively higher response over the studied wavelength range compared to noble metal-based photocatalysts. Therefore, the enhancement of the photocatalytic activity due to electron-hole lifetime extension seems to be the main argument supported by the obtained results.

Finally, Figure 4.16 shows the contribution of ROS to DCA degradation depending on the catalyst type. It can be observed that 100% of the DCA degradation was conducted by $\cdot OH_{free}$ radicals generated from water

molecules reacting with h^+_{VB} when TiO_2 was used as the catalyst (Figure 4.16-A). With regard to TiO_2/Pt, since Pt acts as an electron trap supplying a greater number of available electrons, approximately 78.2% of the degradation was conducted by $\cdot OH_{free}$ radicals formed from photogenerated $O_2^{\cdot-}$ radicals (Figure 4.16-B). $O_2^{\cdot-}$ radicals are created when O_2 molecules from the reaction medium accept an electron (4.5), and these induce the generation of H_2O_2 through an intermediate peroxide process (4.13) - (4.14). The H_2O_2 can result in $\cdot OH_{free}$ radicals, mainly via electron transfer, which act as powerful oxidants and participate in the decomposition of DCA. Therefore, H_2O_2 apparently plays a key role in the TiO_2/Pt photocatalytic process. Similarly, but contributing 64.9%, the DCA degradation using TiO_2/Ag was promoted by $\cdot OH_{free}$ radicals generated from the transformation of $O_2^{\cdot-}$ radicals. Moreover, the $\cdot OH_{ads}$ radicals contributed 35.1% in the study of the silver-doped catalyst (Figure 4.16-B). These results are supported by the evidence of higher concentration of H_2O_2 using TiO_2/Pt than using TiO_2/Ag and the practically nonexistent generation when TiO_2 was employed as photocatalyst (Figure 4.14).

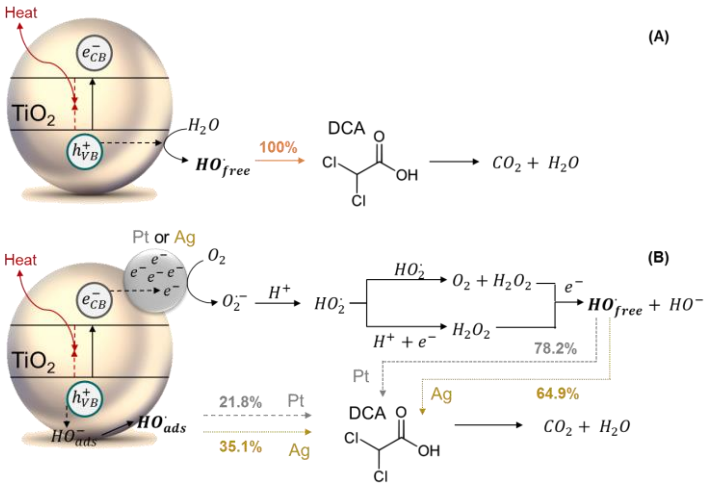

Figure 4.16 Proposed ROS mechanism in the photocatalytic degradation of DCA by TiO_2 (A), TiO_2/Pt, and TiO_2/Ag (B)

Previous work has focused on understanding the generation mechanism for ROS and their involvement in the degradation pathways of organic pollutants using selected chemical scavengers. Research efforts have aimed at the mechanistic study of the generation of ROS on TiO_2; however, varying results have been reported. Wang and co-workers (2010) indicated that valence band holes were the main active species in the TiO_2 photocatalyst (P25), which could oxidize the adsorbed methylene blue under UV light. However, Raja and co-workers (2005) concluded that superoxide radicals play an important role during the ring opening of a lignin model compound using a TiO_2-P25 semiconductor and UV-Vis light. On the other hand, Chen and co-workers (2005) reported that the photocatalytic degradation mechanism under UV light consisted of the strong absorption of azo dye acid orange 7 molecules on the TiO_2 surface, and then the degradation reaction was mostly initiated by direct electron transfer between a positive hole and an organic molecule. When TiO_2-P25 was tested in a recent work developed by Cavalcante and co-workers (2016), a coupled influence of hydroxyl radicals (84%) and valence band holes (10%) was observed during the photocatalytic degradation of metoprolol employing a solar simulator as the light source. Moreover, when TiO_2 was coupled to different dopants, different ROS were involved in the organic pollutant degradation pathways. Cruz-Ortiz and co-workers (2017) studied the influence of the light source on ROS generation using TiO_2/rGO catalysts. They reported that superoxide radicals were the main species involved in *Escherichia coli* disinfection under visible light; however, hydroxyl radicals, hydrogen peroxide, and singlet oxygen ($^1O_2$) conducted the degradation process when UV-Vis light was used. Cavalcante and co-workers (2016) examined the contribution of the main active species to the photocatalytic degradation of metoprolol using a solar simulator and TiO_2/Boron 5% as the photocatalyst, indicating that ·OH radicals are the dominant reactive species, contributing around 80%, with $O_2^{\cdot-}$ radicals and holes contributing to a lesser extent. Nevertheless, the study developed by

Yang and co-workers (2015) showed that active photoinduced holes and $O_2^{\cdot-}$ radicals, rather than ·OH radicals, were the dominant species responsible for rhodamine B (RhB) degradation when P25/Ag_3PO_4/graphene oxide was used as the photocatalyst under visible light. For nitrogen and fluorine doped TiO_2 (NF-TiO_2), studies on the role of ROS suggested that $O_2^{\cdot-}$ and ·OH were involved in cyanotoxin degradation in visible and UV-Vis light, respectively (Pelaez *et al*., 2016). Therefore, although some researchers have looked at the ROS generated in photocatalytic processes, the role of the reactive oxygen species still remains controversial due to the dependence on the nature of the photocatalyst, light source, and organic pollutant treated.

4.4. Final remarks

Titanium dioxide doped with noble metals and/or GO nanosheets with higher photocatalytic activity than bare TiO_2 were successfully synthesized, varying the noble metal load. The improvement in the photocatalytic activity of TiO_2/NM composites was successfully explained by two mechanisms. Under UV irradiation, the Schottky barrier does not permit the backflow of electrons, thereby preventing recombination, and secondly, under visible light, the LSPR effect promotes charge-carrier separation within the TiO_2 with the assistance of the local electromagnetic field induced by surface plasmons. Under the defined experimental conditions, the effectiveness of the photocatalytic degradation of DCA was found to follow the order of TiO_2/Pt>GO/TiO_2>TiO_2/Ag>TiO_2. Therefore, TiO_2/Pt composites showed the highest photoactivity among the other catalysts, achieving total mineralization after seven hours of treatment. This can be explained by the larger Schottky barrier formed with Pt nanoparticles than that formed with Ag, allowing the effective transfer of photogenerated charges. The presence of GO in ternary composites does not always improve the photocatalytic process. The recoverability and

reusability were verified, and the catalysts did not show significant loss of activity.

Moreover, and in order to gain insight into the degradation mechanisms, the contribution of different ROS to the oxidation kinetics of DCA using TiO_2 and noble metal-doped TiO_2 catalysts has been studied. Direct degradation via h^+_{VB} was ruled out for all the photocatalysts studied since there was no significant adsorption of DCA onto the solids. In the case of the TiO_2 catalyst, $\cdot OH_{free}$ radicals played the most important role in DCA degradation kinetics. The improved performance of noble metal-doped catalysts was seen in addition to the generation of ROS other than $\cdot OH_{free}$ radicals compared to bare TiO_2. DCA degradation in the presence of TiO_2/Pt and TiO_2/Ag was mainly due to the activity of $\cdot OH_{free}$ radicals from the transformation of $O_2^{\cdot-}$ and, to a lesser extent, $\cdot OH_{ads}$ radicals. The quantification of $\cdot OH_{free}$ radicals when $O_2^{\cdot-}$ radicals were removed from the reaction medium showed a significant decrease in the generation of $\cdot OH_{free}$ radicals. It was therefore assumed that $O_2^{\cdot-}$ radicals were critical in the formation of $\cdot OH_{free}$ radicals through disproportionation to H_2O_2. A higher contribution of these $\cdot OH_{free}$ radicals was seen with TiO_2/Pt (78.2% ± 0.5) than with TiO_2/Ag (64.9% ± 3.6). FA could not be used as scavenger when TiO_2/Ag was employed as the catalyst due to the reaction between FA and the DCA catalyzed by Ag. In conclusion, this chapter contributes to the technical assessment of the photocatalytic DCA degradation by analyzing the performance of newly synthesized photocatalysts while also providing insight into the mechanisms responsible for the photocatalytic degradation through an analysis of the role of different ROS.

4.5. References

Cassano, A.E., Alfano, O.M. (2000) Reaction engineering of suspended solid heterogeneous photocatalytic reactors, Catalysis Today 58:167-197.

Cavalcante, R.P., Dantas, R.F., Bayarri, B., González, O., Giménez, J., Esplugas, S., Junior, A.M. (2016) Photocatalytic mechanism of metoprolol oxidation by photocatalysts TiO_2 and TiO_2 doped with 5% B: Primary active species and intermediates. Applied Catalysis B: Environmental 194:111-122.

Chen, Y., Yang, S., Wang, K., Lou, L. (2005) Role of primary active species and TiO_2 surface characteristic in UV-illuminated photodegradation of Acid Orange 7. Journal of Photochemistry and Photobiology A: Chesmistry 172:47-54.

Chong, M.N., Jin, B., Chow, C.W.K., Saint, C. (2010) Recent developments in photocatalytic water treatment technology: A review. Water Research 44:2997-3027.

Cruz-Ortiz, B.R., Hamilton, J.W.J., Pablos, C., Días-Jiménez, L., Costés-Hernández, D.A., Sharma, P.K., Castro-Alférez, M., Fernández-Ibañez, P., Dunlop, P.S.M., Byrne, J.A. (2017) Mechanism of photocatalytic disinfection using titania-graphene composites under UV and visible irradiation. Chemical Engineering Journal 316:179-186.

Devi, L.G., Kavitha, R. (2016) A review on plasmonic metal-TiO_2 composite for generation, trapping, storing and dynamic vectorial transfer of photogenerated electrons across the Schottky junction in a photocatalytic system. Applied Surface Science 360:601-622.

Gao, F., Yang, Y., Wang, T. (2015) Preparation of porous TiO_2/Ag heterostructure films with enhanced photocatalytic activity. Chemical Engineering Journal 270:418-427.

Gou, X., Cheng, Y., Liu, B., Yang, B., Yan, X. (2015) Fabrication and Photocatalytic Properties of TiO_2/Reduced Graphene Oxide/Ag Nanocomposites with UV/Vis Response. European Journal of Inorganic Chemistry 2015:2222-2228.

Grabowska E., Marchelek M., Klimczuk T., Trykowski G., Zaleska-Medynska A. (2016) Noble metal modified TiO_2 microspheres: Surface properties and photocatalytic activity under UV-vis and visible light. Journal of Molecular Catalysis A: Chemical 423:191-206.

Henderson, M.A., Shen, M. (2017) Electron-scavenging chemistry of benzoquinone on TiO_2 (110). Topics in Catalysis 60:440-445.

Herron, J. A., Scaranto, J., Ferrin, P.R., Li, S., Mavrikakis, M. (2014) Trends in formic acid decomposition on model transition metal surfaces: a density functional theory study, ACS Catalysis 4:4434-4445.

Hirakawa, T., Yawata, K., Nosaka, Y. (2007) Photocatalytic reactivity for $O_2^{\cdot-}$ and $OH^{\cdot}$ radical formation in anatase and rutile TiO_2 suspension as the effect of H_2O_2 addition. Applied Catalysis A: General 325:105-111.

Hoffman, M.R., Martin, S.T., Choi, W., Bahneman, D.W. (1995) Environmental applications of semiconductor photocatalysis. Chemical Reviews 95:69-96.

Hsieh, S.H., Chen, W.J., Wu, C.T. (2015) Pt-TiO_2/graphene photocatalysts for degradation of AO7 dye under visible light. Applied Surface Science 340:9-17.

Ingram, D.B., Christopher, P., Bauer, J.L., Linic, S. (2011) Predictive model for the design of plasmonic metal/semiconductor composite photocatalysts. ACS Catalysis 1:1441-1447.

Ismail A.A., Al-Sayari S.A., Bahnemann, D.W. (2013) Photodeposition of precious metals onto mesoporous TiO_2 nanocrystal with enhanced their photocatalytic activity for methanol oxidation. Catalysis Today 209:2-7.

Ismail A.A., Bahnemann, D.W. (2011) Mesostructured Pt/TiO_2 nanocomposites as highly active photocatalysts fot the photoxidation of dichloroacetic acid. Journal of Physical Chemistry C 115:5784-5791.

Khan, M.R., Chuan, T.W., Yousuf, A., Chowdhury, M.N.K., Cheng, C.K. (2015) Schottky barrier and surface plasmonic resonance phenomena towards the photocatalytic reaction: study of their mechanisms to enhance photocatalytic activity. Catalysis Science & Technology 5:2522-2531.

Lee, S-Y., Park, S-J. (2013) TiO_2 photocatalyst for water treatment applications. Journal of Industrial and Engineering Chemistry 19:1761-1769.

Li M., Yu Z., Liu Q., Sun L., Huang W. (2016) Photocatalytic decomposition of perfluorooctanoic acid by noble metallic nanoparticles modified TiO_2. Chemical Engineering Journal 286:232-238.

Liao, Y., Brame, J., Que, W., Xie, Z., Xie, H., Li, Q., Fabian, M., Alvarez, P.J. (2013) Photocatalytic generation of multiple ROS types using low-temperature crystallized anodic TiO_2 nanotube arrays. Journal of Hazardous Materials 260:434-441.

Liu, Y., Han, J., Qiu, W., Gao, W. (2012) Hydrogen peroxide generation and photocatalytic degradation of estrone by microstructural controlled ZnO nanorod arrays. Applied Surface Science 263:389-396.

Liu L., Bai H., Liu J., Sun D.D. (2013) Multifunctional graphene oxide-TiO_2-Ag nanocomposites for high performance water disinfection and decontamination under solar irradiation. Journal of Hazardous Materials 261:214-223.

Marinho, B.A., Djellabi, R., Cristóvão, R.O., Loureiro, J.M., Boaventura, R.A.R., Dias, M.M., Lopes, J.C.B., Vilar, V.J.P. (2017) Intensification of heterogeneous TiO_2 photocatalysis using an innovative micro-meso-structured-reactor for Cr(VI) reduction under simulated solar light. Chemical Engineering Journal 318:76-88.

Pelaez, M., Falaras, P., Likodimos, V., O'Shea, K., dela Cruz, A.A., Dunlop, S.M., Byrne, J.A., Dionysiou, D.D. (2016) Use of selected scavengers for the determination of NF-TiO_2 reactive oxygen species during the degradation of microcystin-LR under visible light irradiation. Journal of Molecular Catalysis A: Chemical 425:183-189.

Raja, P., Bozzi, A., Mansilla, H., Kiwi, J. (2005) Evidence for superoxide-radical anion, singlet oxygen and OH-radical intervention during the degradation of the lignin model compound (3-methoxy-4-hydroxyphenylmethylcarbinol), Journal of Photochemistry and Photobiology A: Chemistry 169:271-278.

Sahel, K., Elsellami, L., Mirali, I., Dappozze, F., Bouhent, M., Guillard, C. (2016) Hydrogen peroxide and photocatalysis. Applied Catalysis B: Environmental 188:106-112.

Schneider, J., Matsuoka, M., Takeuchi, M., Zhang, J., Horiuchi, Y., Anpo, M., Bahnemann, D.W. (2014) Understanding TiO_2 Photocatalysis: Mechanisms and Materials. Chemical Reviews 114(19):9919-9986.

Tan L.L., Ong W.J., Chai S.P., Mohamed A.R. (2015) Noble metal modified reduced graphene oxide/TiO_2 ternary nanostructures for efficient visible-light-driven photoreduction of carbon dioxide into methane. Applied Catalysis B: Environmental 166-167:251-259.

Vaiano V., Iervolino G., Sannino D., Murcia J.J., Hidalgo M.C., Ciambelli P., Navío J.A. (2016) Photocatalytic removal of patent blue V dye on Au-TiO_2 and Pt-TiO_2 catalysts. Applied Catalysis B: Environmental 188:134-146.

Verbruggen S.W., Keulemans M., Filippousi M., Flahaut D, Van Tendeloo D., Lacombe S., Martens J.A., Lenaerts S. (2014) Plasmonic gold-silver alloy on TiO_2 photocatalysts with tunable visible light activity. Applied Catalysis B: Environmental 156-157:116-121.

Wang Q., Dong P., Huang Z., Zhang X. (2015) Synthesis of Ag or Pt nanoparticle-deposited TiO_2 nanorods for the highly efficient photoreduction of CO_2 to CH_4. Chemical Physics Letters 639:11-16.

Wang, W-K., Chen, J-J., Li, W-W., Pei, D-N., Zhang, X., Yu, H-Q. (2015) Synthesis of Pt-loaded self-interspersed anatase TiO_2 with a large fraction of (001) facets for efficient photocatalytic nitrobenzene degradation. Applied Materials & Interfaces 7:20349-20359.

Wang, Y., Shi, R., Lin, J., Zhu, Y. (2010) Significant photocatalytic enhancement in methylene blue degradation of TiO_2 photocatalysts via graphene-like carbon in situ hybridization. Applied Catalysis B: Environmental 100:179-183.

Wen, J., Li, X., Liu, E., Fang, Y., Xie, J., Xu, Y. (2015) Photocatalysis fundamentals and surface modification of TiO_2 nanomaterials. Chinese Journal of Catalysis 36:2049-2070.

Yang, X., Qin, J., Jiang, Y., Chen, K., Yan, X., Zhang, D., Li, R., Tang, H. (2015) Fabrication of P25/Ag_3PO_4/graphene oxide heterostructures for enhanced solar photocatalytic degradation of organic pollutants and bacteria. Applied Catalysis B: Environmental 166-167:231-240.

Zhang P., Wang T., Gong J. (2015) Mechanistic understanding of the plasmonic enhancement for solar water splitting. Advanced Materials 27:5328-5342.

Ziylan-Yavas A., Mizukoshi Y., Maeda Y., Ince N.H. (2015) Supporting of pristine TiO_2 with noble metals to enhance the oxidation and mineralization of paracetamol by sonolysis and sonophotolysis. Applied Catalysis B: Environmental 172-173:7-17.

CHAPTER 5

PHOTOCATALYTIC HYDROGEN PRODUCTION FROM A RENEWABLE SOURCE

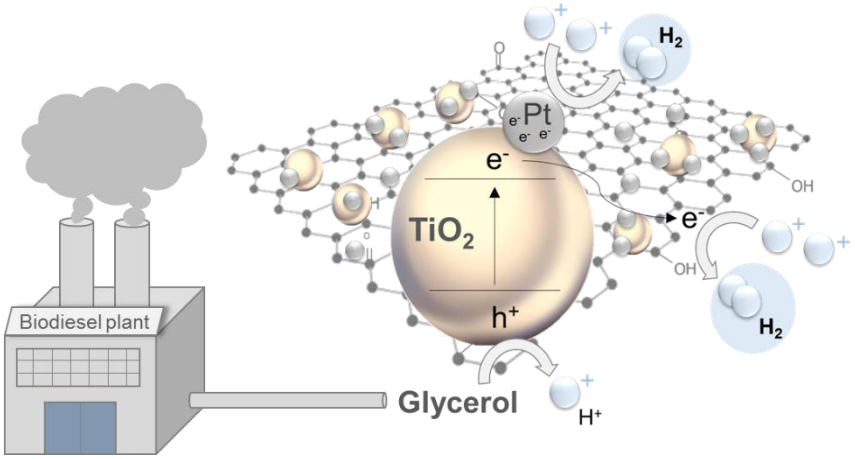

The increasing world population derives in a fast increase of energy consumption and depletion of natural resources, thus, new actions and technologies to face the growing energy crisis are demanded. Currently, 90% of the world's energy supply is derived from fossil fuel, a limited energy source (Peng *et al*., 2015). Moreover, CO_2 release is a well-known disadvantage of carbon burning considering this gas the main culprit involved in greenhouse effect. Therefore, producing green and renewable energy is currently a global issue.

Hydrogen appears as a potential alternative to fossil fuels as energy vector for the future. It is widely considered to be the most promising clean energy vector. Its use is being explored in many technology areas due to its favorable characteristics, i.e., it is storable, presents high energy content, and absence of toxic pollutants, particulates or greenhouse-responsible emissions during its combustion (Kondarides *et al*., 2008; Clarizia *et al*., 2014; Pai *et al*. 2016; Kumar *et al*., 2017). As it was stated in Chapter 1, the main challenge is finding an environmentally friendly source of hydrogen. The industrial hydrogen production processes can only start from substances which contain hydrogen since its presence on earth is in combination with other elements. Moreover, sustainable H_2 production requires clean primary energy sources, e.g. solar energy (Beltran *et al*., 2016).

Among various biomass-derived compounds proposed as feedstock for hydrogen production, glycerol is of special interest because it is produced as by-product in the biodiesel production industry (Daskalaki and Kondarides, 2009). For every 100 ton of product, 10 ton of glycerol are generated. According to the European Union recommendation (2003/30/EC Directive), the fraction of biofuels in conventional fuels should at least be 5.75 wt% in 2010 and 20 wt% in 2020. Therefore, the production of biodiesel was expected to grow due to the environmental policy of the EU, the United States as well as other developed and developing countries

(Stelmachowski *et al*., 2014). The forecast biodiesel production in 2018 is 11.1 million tons and 1.3 million tons in EU and Spain, respectively (Flach *et al*., 2017). Hence, the price of glycerol has decreased significantly due to overproduction, and valorization of sustainable glycerol to green fuels appears as a promising alternative for future energy production (Estahbanati *et al*., 2017).

Much effort is being invested in the development of technologies capable of producing hydrogen using solar light as primary energy source. In this way, heterogeneous photocatalysis is of direct interest due to its ability of integrating hydrogen generation and by-product valorization. As it was remarked in Chapter 1, TiO_2 has been the most promising material used as photocatalyst. However, bare TiO_2 demonstrates almost negligible activity for H_2 production. Currently, an important challenge is the design of a photocatalyst able to drive the photo-reforming of biomass derivatives. The photocatalytic hydrogen production using organic matter as feedstock can be obtained substantially following the next approach: the organic matter reacts with the positive holes (or ·OH radicals) of the illuminated photocatalyst and is oxidized generating intermediate compounds and protons (5.1), while the latter are reduced by photogenerated electrons forming hydrogen (5.2).

$$\text{Valence band: } C_3H_8O_3 + h^+_{Vb}(\cdot OH) \rightarrow \text{Intermediates} + H^+ \quad (5.1)$$

$$\text{Conduction band: } 2H^+ + 2e^-_{CB} \rightarrow H_2 \quad (5.2)$$

In previous chapters, a high performance photocatalyst based on TiO_2 doped with platinum and GO was obtained and its viability has been tested for the treatment of organic water pollution. Therefore, in order to make further progress in the photocatalytic production of hydrogen from biomass-derived compounds, these photocatalysts have been tested using synthetic and crude glycerol solutions. This chapter explores the effects of

six key operating parameters (including vol% of glycerol, pH, catalyst loading, wt% of GO, wt% of Pt and temperature) and studies the performance of TiO_2/GO(x)/Pt(y) photocatalysts under UV-visible and visible light. Therefore, the novelty of this work is to gain insight into the challenges arising from the use of these photocatalysts to produce hydrogen from crude glycerol compared to synthetic glycerol and in addition, the use of visible light compared to ultraviolet light.

5.1. Photocatalysts characterization

TEM images of TiO_2/GO(3%), TiO_2/Pt(3.8%) and TiO_2/GO(3%)/Pt(3.8%) photocatalysts are shown in Figure 5.1. TiO_2/GO(3%) composite presented GO nanosheets decorated with TiO_2 nanoparticles on its surface (Figure 5.1-A1). In the case of TiO_2/Pt(3.8%) composite (Figure 5.1-A2), nanoparticles of platinum, with an average diameter of 5 nm were well deposited on the TiO_2. Figure 5.1-A3 shows the TEM image of TiO_2/GO(3%)/Pt(3.8%) ternary composite, demonstrating a homogeneous dispersion of platinum nanoparticles on the surface of the TiO_2/GO composite. Figure 5.1-B1 shows the EDX spectrum of TiO_2/GO(3%) noticing that the GO sheets were mainly composed of carbon with a minor proportion of oxygen. The presence of platinum nanoparticles in the TiO_2/Pt(3.8%) catalyst was further evidenced (Figure 5.1-B2). Finally, ternary catalysts also presented Pt peaks in the EDX spectrum (Figure 5.1-B3) confirming the good loading of Pt on the catalyst surface.

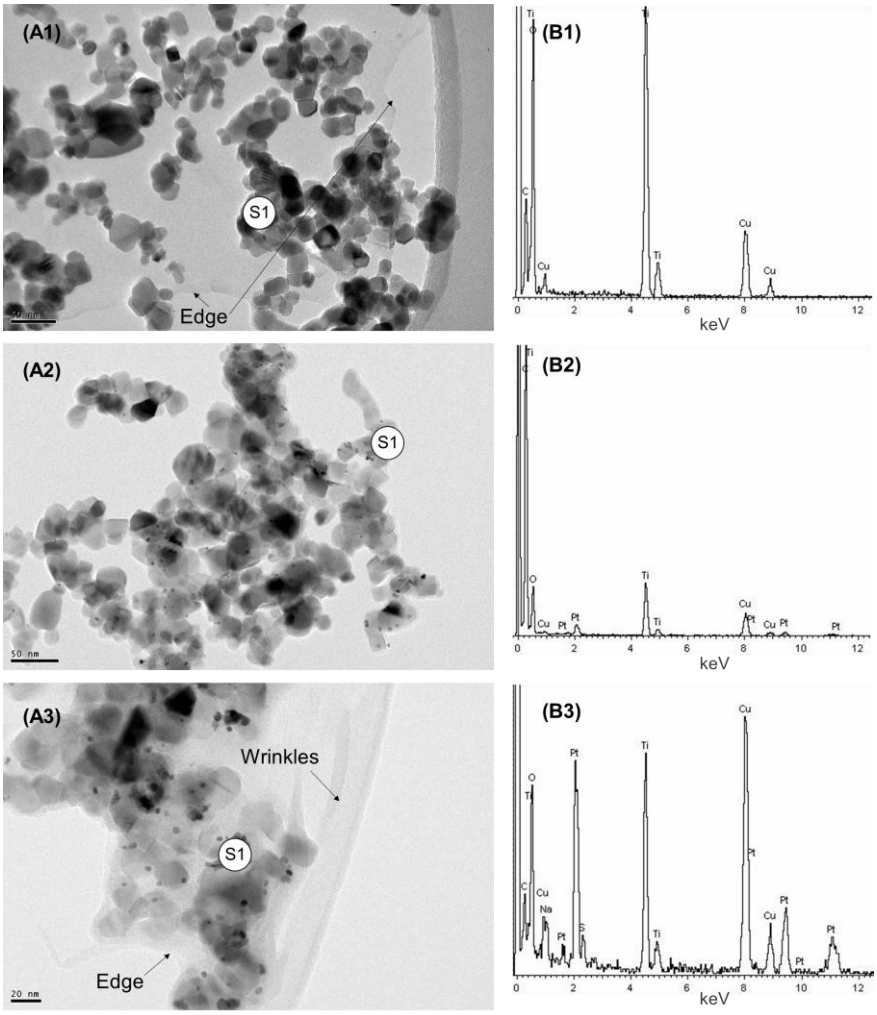

Figure 5.1 TEM images (A) and EDX analysis (B) of TiO_2/GO(3%) (1), TiO_2/Pt(3.8%) (2) and TiO_2/GO(3%)/Pt(3.8%) (3).

Figure 5.2 shows the FTIR spectra of the TiO_2, GO, TiO_2/GO(5%) and TiO_2/GO(3%)/Pt(3.8%) samples. The GO spectrum shows many strong absorption peaks that are related to various oxygen functional groups as already explained in Figure 3.3. In the TiO_2/GO(3%) and TiO_2/GO(3%)/Pt(3.8%) spectra, the intensity of all absorption peaks corresponding to oxygen functional groups presented a significant

decrease compared to those in the GO spectra, implying that GO was significantly reduced to rGO during the synthesis step. In addition, the broad bands between 500-900 cm^{-1} are related to Ti-O-Ti and Ti-O-C stretching vibration. Therefore, the above results confirmed the successful preparation of GO-based catalysts via thermal treatment and the stability of GO sheets after the photodeposition of Pt nanoparticles.

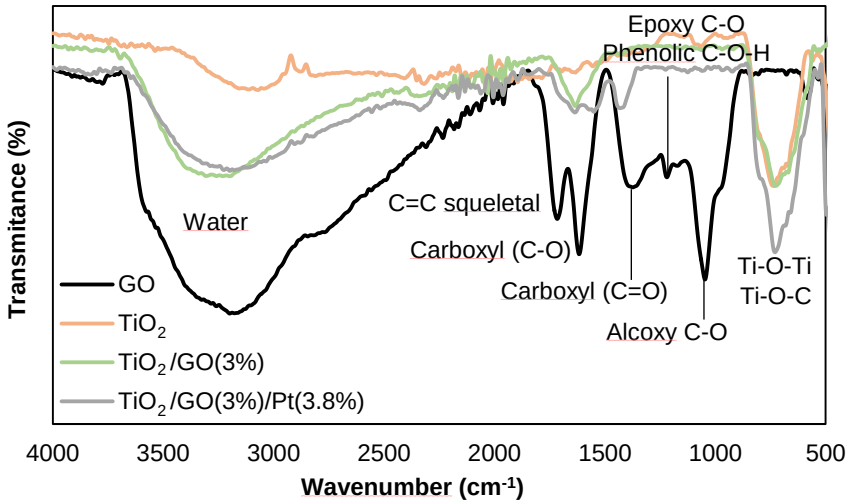

Figure 5.2 FTIR spectra of GO, TiO_2/GO(3%) and TiO_2/GO(3%)/Pt(3.8%) photocatalysts.

Thermal gravimetric analyses of GO, TiO_2/Pt(3.8%), TiO_2/GO(3%), TiO_2/GO(1%)/Pt(3.8%), TiO_2/GO(2%)/Pt(3.8%), TiO_2/GO(3%)/Pt(3.8%) and TiO_2/GO(5%)/Pt(3.8%) in a N_2 atmosphere are shown in Figure 5.3. Three differentiated steps of mass loss with temperature were observed in the GO curve ranging from ambient temperature to 900 ºC. These steps are related to desorption of absorbed water (bellow 100 ºC), the removal of oxygen-containing groups (200-250 ºC) and the destruction of the carbon skeleton (around 500 ºC). The GO-based photocatalysts exhibited displacements of the onsets of weight loss relative to GO. These results suggest that GO was initially stabilized by the embedded TiO_2, which

delayed the weight loss normally observed in the thermal analysis of GO samples.

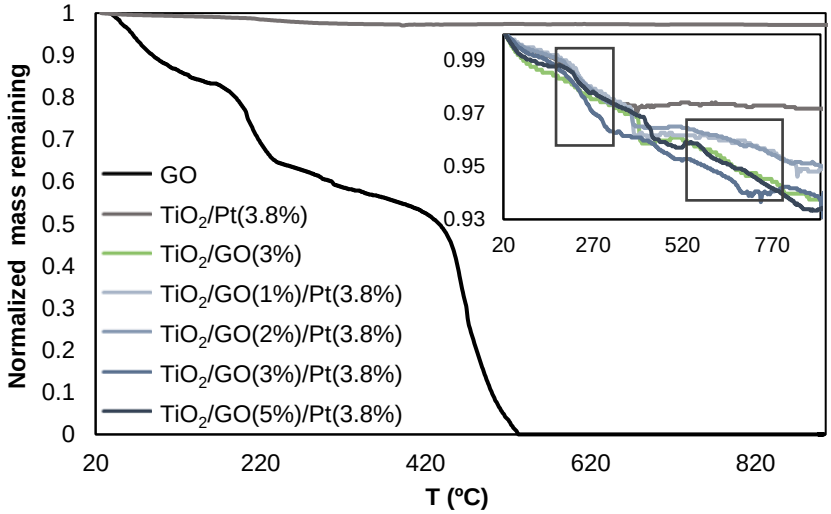

Figure 5.3 Thermal gravimetric analysis of GO and TiO_2/Pt(3.8%), TiO_2/GO(3%), and TiO_2/GO(x)/Pt(3.8%) (x=1-5 wt%).

To determine the specific surface area of the catalysts, N_2 adsorption/desorption measurements and the Brunauer-Emmet-Teller (BET) analysis method were employed. TiO_2-based materials showed a slight enhancement in surface area values compared to bare TiO_2 (54.98 $m^2\ g^{-1}$), reaching increments of 3.40, 6.13, 2.71, 3.82, 7.45, and 3.58% for TiO_2/Pt(3.8%), TiO_2/GO(3%), TiO_2/GO(1%)/Pt(3.8%), TiO_2/GO(2%)/Pt(3.8%), TiO_2/GO(3%)/Pt(3.8%) and TiO_2/GO(5%)/Pt(3.8%), respectively (Table 5.1). There were no significant variations in surface area among the synthesized catalysts; therefore, the influence of this variable on the photocatalytic activity could not be analyzed.

The method of UV-vis diffuse reflectance spectroscopy was employed to estimate the indirect band gap of the photocatalysts (Table 5.1). The values clearly show the narrowing of the band gap with the introduction of

GO in TiO_2 and this is generally attributed to the formation of Ti-O-C bonds between TiO_2 and GO. Among the photocatalysts tested, the lowest band gap was obtained for TiO_2/GO(3%)/Pt(3.8%), which suggests that the interaction of TiO_2 and GO is the strongest one in this photocatalyst.

Table 5.1 Specific area and bandgap values of photocatalysts.

Sample	Specific Area (m^2/g)	Band gap
TiO_2	54.98 ± 0.29	3.25
TiO_2/Pt (3.8%)	56.85 ± 0.33	3.22
TiO_2/GO(3%)	58.35 ± 0.29	3.17
TiO_2/GO(1%)/Pt(3.8%)	57.08 ± 0.28	2.98
TiO_2/GO(2%)/Pt(3.8%)	56.47 ± 0.31	2.89
TiO_2/GO(3%)/Pt(3.8%)	59.08 ± 0.32	2.52
TiO_2/GO(5%)/Pt(3.8%)	56.95 ± 0.27	2.98

XRD analyses were performed to identify the crystal phases of the TiO_2, GO, TiO_2/GO(3%), TiO_2/Pt(3.8%) and TiO_2/GO(3%)/Pt(3.8%) catalysts (Figure 5.4). The diffraction peak at 11.3º in the GO curve is related to the possible existence of trapped water molecules between the layers of GO. However, GO-based composites did not exhibit this peak due to the removal of regular stacking of the GO by the intercalation of TiO_2. Characteristic crystal planes of anatase and rutile phases observed in bare TiO_2 were also detected in TiO_2/GO(3%), TiO_2/Pt(3.8%) and TiO_2/GO(3%)/Pt(3.8%). Moreover, diffraction peaks corresponding to standard patterns for Pt (JCPDS 65-2868) were observed in the TiO_2/Pt(3.8%) and TiO_2/GO(3%)/Pt(3.8%) curves, supporting the presence of this noble metal in the composites.

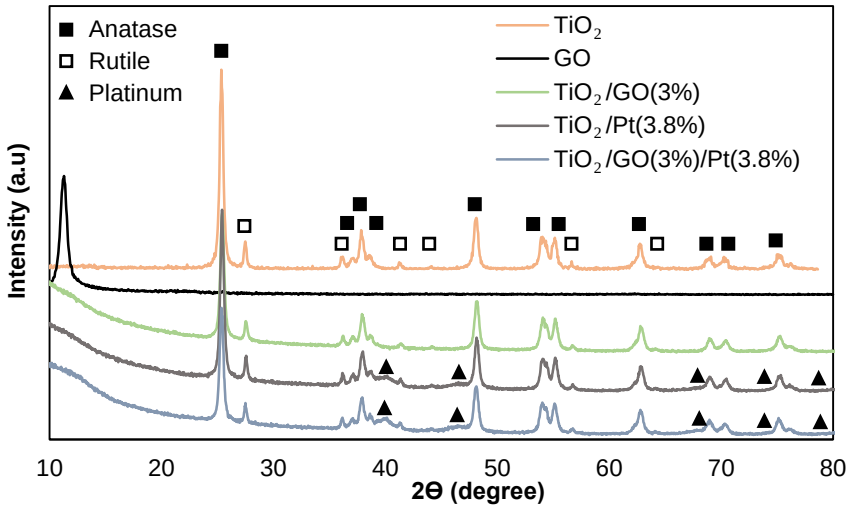

Figure 5.4 XRD patterns of TiO_2, GO, TiO_2/GO(3%), TiO_2/Pt(3.8%) and TiO_2/GO(3%)/Pt(3.8%) photocatalysts.

The surface composition and elemental chemical state of TiO_2/GO(3%)/Pt(3.8%) were characterized using XPS technique. The Ti 2p XPS spectrum (Figure 5.5-A) shows three species of Ti related to TiO_2, TiO and Ti. Therefore, commercial TiO_2 suffered some modifications during the coupling of GO nanosheets and Pt nanoparticles on its surface. Figure 5.5-B shows C 1s spectral region of TiO_2/GO(3%)/Pt(3.8%) photocatalyst, observing four different species of C corresponding to C-Ti and C-Pt interactions, adsorbed CO_2, graphitic C and C=O at 281.3 eV, 282.7 eV, 284.9 eV and 288.3 eV, respectively. The typical zone of O 1s signals (Figure 5.5-C) showed four peaks, three of them (528.9 eV, 530.6 eV and 532.2 eV) are assigned to metallic oxides and metallic hydroxides while the peak at 526.9 eV might be ascribed to oxygen atoms partially negatives. Finally, two peaks of Pt $4f_{7/2}$ and Pt $4f_{5/2}$ at 70.9 and 74.2 eV, respectively, with a splitting energy of 3.3 eV (Figure 5.5-D), attributed to the metallic state of Pt, were observed. Moreover, two additional peaks were noticed at 72.3 and 75.7 eV related to Pt^{2+} chemical state. This fact

might be attributed to the presence of Pt-O on TiO_2 surface, or to the diffusion of Pt^0 atoms into TiO_2 crystal lattice and oxidized to Pt^{2+} to substitute Ti^{4+} or form the interstitial ions (Hsieh *et al*., 2015).

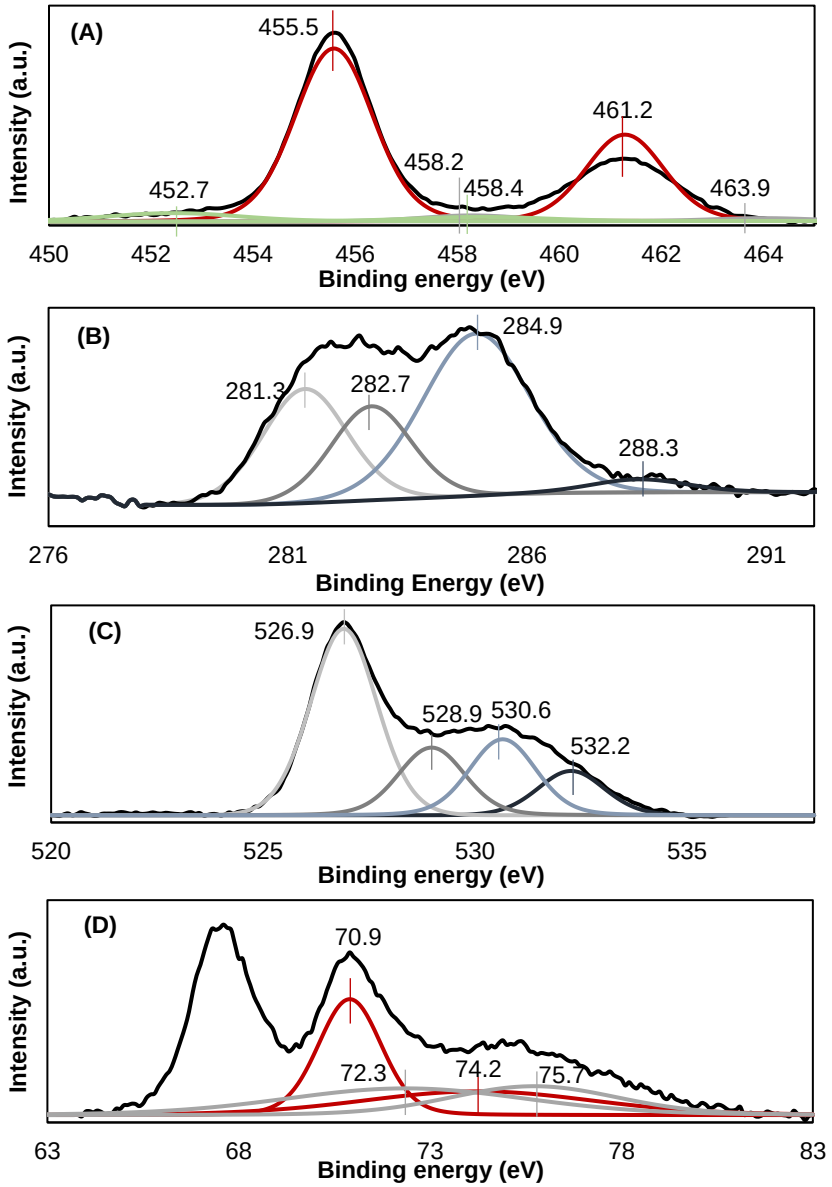

Figure 5.5 High-resolution XPS spectra of TiO_2/GO(3%)/Pt(3.8%): (A) Ti 2p spectral region, (B) C 1s spectral region, (C) O 1s spectral region, and (D) Pt 4f spectral region.

The platinum loadings on the photocatalysts were determined by ICP-MS analysis and the obtained values (Table 5.2) were very similar to the nominal composition, which proves the efficiency of the photodeposition method.

Table 5.2 Pt loading (%wt) values.

Sample	wt% Pt
TiO_2/Pt (3.8%)	3.3
TiO_2/GO(3%)/Pt(1.5%)	1.6
TiO_2/GO(3%)/Pt(2.5%)	2.4
TiO_2/GO(3%)/Pt(3.8%)	3.7

5.2. Photocatalytic hydrogen production rate using synthetic and crude glycerol

The hydrogen production over time presented a short initial period during which the hydrogen generation increases fast and a long second period in which hydrogen production increases more slowly but steadily. The hydrogen production rate was calculated in the second period for the study of the different parameters. It should be noted that the measurement sensitivity of the experimental system used is approximately 0.44 ± 0.02 mmol of hydrogen and low hydrogen productions are not accurate enough.

5.2.1. UV-Vis light as energy source

The effect of six parameters (vol% of glycerol, pH, catalyst loading, wt% of GO, wt% of Pt and temperature) on the photocatalytic hydrogen generation rate, using synthetic glycerol solutions as sacrificial agent and TiO_2/GO(x)/Pt(y) as catalyst, was studied (Table 5.3). All the experiments (Exp) were performed in duplicate.

Table 5.3 Studied parameters using synthetic glycerol as sacrificial agent.

Exp	[Glycerol] (vol %)	pH	[Catalyst] (gL^{-1})	GO (wt%)	Pt (wt%)	T (ºC)
1	5	5	0.50	3	3.8	30
2	20	5	0.50	3	3.8	30
3	50	5	0.50	3	3.8	30
4	80	5	0.50	3	3.8	30
5	20	7	0.50	3	3.8	30
6	20	11	0.50	3	3.8	30
7	20	7	0.10	3	3.8	30
8	20	7	0.25	3	3.8	30
9	20	7	0.75	3	3.8	30
10	20	7	1.00	3	3.8	30
11	20	7	0.25	1	3.8	30
12	20	7	0.25	2	3.8	30
13	20	7	0.25	5	3.8	30
14	20	7	0.25	3	1.5	30
15	20	7	0.25	3	2.5	30
16	20	7	0.25	3	3.8	40

Figure 5.6-A shows the effect of the initial concentration of synthetic glycerol on the hydrogen generation rate. It can be observed that hydrogen production rate increases with the initial glycerol concentration until reaching a maximum of 50.60 mmol h^{-1} g^{-1} for a 20 vol%. The further increase in the alcohol concentration leads to a decrease in the activity, likely because of the saturation of the surface active sites (Lyubina *et al*., 2013). Regarding the effect of pH on the hydrogen production rate, a maximum was reached at pH 7 (Figure 5.6-B). This may be due to the fact that this pH value is close to pH_{zpc} of the catalyst resulting in a maximum concentration of the surface hydroxyl groups. This fact can be related to the maximum adsorption of glycerol on the photocatalyst via hydrogen bonding (Li *et al*., 2009). Figure 5.6-C reveals that the hydrogen production

rate reached the maximum using 0.25 g L^{-1} of catalyst, enhancing 1.14 and 1.5 times the photoactivity compared to 0.1 g L^{-1} and 1 g L^{-1} of catalyst, respectively. Low amounts of catalyst loading can lead to a significant proportion of photons being transmitted outside the reactor and, on the other hand, a high concentration of catalyst in the medium can result in a catalyst agglomeration, interfering the photons absorption (Estahbanati *et al*., 2017). The effect of GO loading on hydrogen production rate can be seen in Figure 5.6-D. The hydrogen production rate increased up to 1.8 fold by the optimization of GO loading (wt%), achieving 70.83 ± 0.43 mmol h^{-1} g^{-1} of hydrogen. High GO content in the ternary composites may hinder the electron transfer acting as charge carrier recombination center. Figure 5.6-E shows the effect of different Pt loading on hydrogen production rate. Platinum clusters act as effective electron traps, reducing the electron-hole pair recombination. Therefore, the hydrogen production rate improves by increasing the Pt loading on the ternary photocatalysts. Larger amounts of Pt were not tested because it is an expensive and scarce noble metal and GO is employed as third co-catalyst with the aim to reduce the amount of platinum maintaining the positive characteristics. Finally, as it can be seen in Figure 5.6-F, the influence of temperature on the hydrogen production rate was moderate. Therefore, it can be concluded that the optimal conditions were 20 vol% of synthetic glycerol, pH 7, TiO_2/GO(3%)/Pt(3.8%) photocatalyst concentration of 0.25 g L^{-1} and 30 ºC, achieving a hydrogen generation rate of 70.83 ± 0.43 mmol h^{-1} g^{-1}, a value much higher than those reported in the literature (Table 5.4).

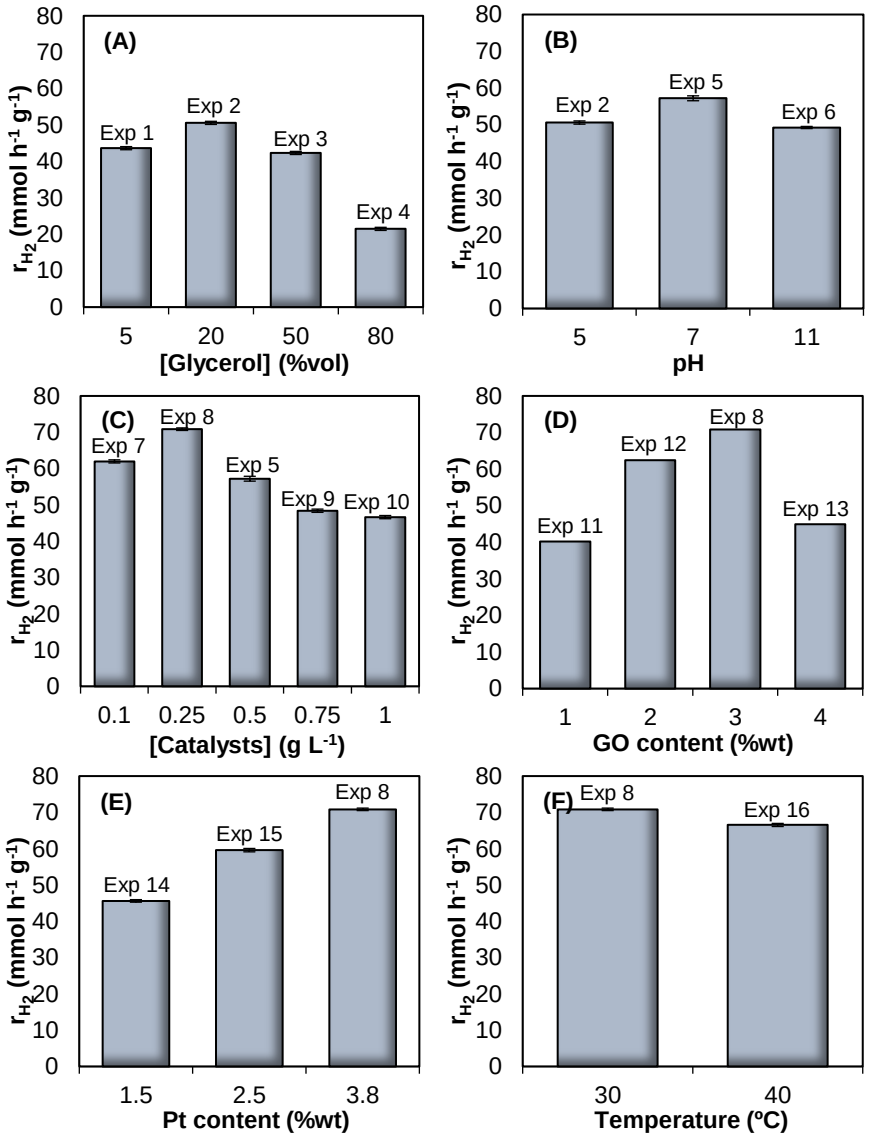

Figure 5.6 Effect of the glycerol initial concentration (vol%) (A), pH (B), catalyst concentration (g L^{-1}) (C), GO loading (wt%) (D), Pt loading (wt%) (E) and temperature (F) on hydrogen production rate using synthetic glycerol solutions.

Table 5.4 collects the photocatalytic hydrogen production rates reported in the literature using glycerol as feedstock. The best

photocatalytic activities were achieved using noble metal-doped TiO_2 photocatalysts under UV light, reaching up to 56.0 mmol h^{-1} g^{-1} of hydrogen. However, a low volume of glycerol solutions was treated in these works (Chen *et al*., 2015; Melián *et al*., 2016; Estahnanati *et al*., 2017). Comparing the results obtained in the present thesis with reported works that employ similar working volumes, it can be observed that hydrogen production rates are up to three orders of magnitude lower (Lv *et al.*, 2015; Clarizia *et al*., 2017; Wang *et al*., 2017). Regarding the hydrogen production rates using visible light or solar simulators, the obtained results were similar or overperform those of the literature, however, the working volume treated in the present thesis is higher (Kondarides *et al*., 2009; Daskalaki and Kondarides, 2009; Beltran *et al*., 2016; Kumer *et al*., 2017; Reddy *et al*., 2017; Seadira *et al*., 2018). Among collected studies from the literature, only Skaf and co-workers (2012) employed a real glycerol by-product from a biodiesel production plant. In the present work, a considerable enhancement in the photocatalytic hydrogen production from crude glycerol has been accomplished.

Table 5.4 Comparison of the photocatalytic hydrogen generation rate obtained in this work with results reported in the literature, using glycerol as sacrificial agent.

Author	**Catalyst**	**Light**	**Volume (mL)**	**r_{H_2} (mmol h^{-1} g^{-1})**
This work	TiO_2/GO/Pt	UV	300	70.83 (synthetic) 12.72 (Crude)
		Visible		3.28 (Synthetic)
Seadira *et al*., 2018	Cu/THS*	Solar Simulator	50	4.25
Reddy *et al*., 2017	TiO_2/Bi	Solar simulator	50	1.00
Kumar *et al*., 2017	TiO_2	Solar simulator	50	4.25
Wang *et al*., 2017	Ag_2O/TiO_2	UV/Vis	100	0.17
Estahnanati *et al*., 2017	TiO_2/Pt	UV	5	56.00
Clarizia *et al*., 2017	TiO_2/Cu	UV	300	7.33
Melián *et al*., 2016	TiO_2/Pt	UV	75	17.33
Beltran *et al*., 2016	TiO_2/Pt	Solar simulator	80	1.30
Skaf *et al*., 2012	TiO_2/Pt	UVA	250	0.25**
Lv *et al*., 2015	ZnO/rGO	UV/Vis	230	0.09
López *et al*. ,2015	TiO_2/Pt	UV	75	8.00
Chen *et al*., 2015	TiO_2/Au	UV	20	26.66
Yu *et al*., 2011	TiO_2/CuO	UV-LED	80	2.06
Daskalaki and Kondarides, 2009	TiO_2/Pt	Solar simulator	60	0.49
Kondarides *et al*., 2008	TiO_2/Pt	Solar simulator	60	2.70

** THS: TiO_2 hollow spheres*
*** Crude glycerol as sacrificial agent*

The effect of three parameters (vol% of glycerol, pH and catalyst loading) on the photocatalytic hydrogen generation rate using crude glycerol solutions and the best photocatalyst previously determined (TiO_2/GO(3%)/Pt(3.8%)) was studied (Table 5.5).

Table 5.5 Studied parameters using crude glycerol as sacrificial agent and TiO_2/GO(3%)/Pt(3.8%) at 30 ºC.

Exp	[Glycerol] (vol%)	pH	[Catalyst] (g L^{-1})
1	0.5	7	0.50
2	1.0	7	0.50
3	5.0	7	0.50
4	20.0	7	0.50
5	1.0	5	0.50
6	1.0	11	0.50
7	1.0	7	0.25
8	1.0	7	1.00

Figure 5.7-A shows the influence of initial crude glycerol concentration on the hydrogen production rate. Crude glycerol residue contains 78% of glycerol, 18% of water, 3% of salts/ashes, 0.5% of methane and 0.5% of non-glycerol organic matter and presents a golden brown color. As already observed using synthetic glycerol, the hydrogen production rate increases with the initial glycerol concentration until reaching a maximum of 12.72 mmol h^{-1} g^{-1} for 1 vol%. The optimal concentration of crude glycerol is lower than that of synthetic glycerol (20 vol%). This fact may be due to the presence of impurities (salts and non-glycerol organic matter) competing for the active sites of the catalyst and the foaming observed at high concentrations of crude glycerol. The natural pH of the crude glycerol solutions was 5, however, adjusting the pH to 7, an increment of 17.23% ± 0.45 on the hydrogen production rate was observed as can be seen in Figure 5.7-B. Therefore, regardless of the origin of glycerol, a neutral pH reports the best results of hydrogen production rate.

The influence of TiO_2/GO(3%)/Pt(3.8%) concentration, ranging between 0.25 g L^{-1} and 1 g L^{-1} was assessed using crude glycerol; and the experimental data are shown in Figure 5.7-C. It can be noticed that the best photocatalytic activity was obtained with 0.5 g L^{-1} of catalyst, a concentration two fold higher than the optimum observed using synthetic glycerol. This suggests that the presence of impurities competing for adsorption on the catalyst surface makes necessary to increase the catalyst loading that provides a greater number of active sites. Moreover, high turbidity of crude glycerol solutions associated to the presence of ashes can interfere with the incident light flux, requiring higher catalyst loading. The turbidity of synthetic glycerol solutions was 0.13±0.05 NTU, while in the case of crude glycerol solutions, the turbidity values range from 2.19 NTU (crude glycerol 0.5 %vol) to 42.22 NTU (crude glycerol 20 vol%).

Therefore, when crude glycerol was employed as sacrificial agent, the optimal operating conditions were 1 vol% of glycerol, pH 7 and 0.5 g L^{-1} of TiO_2/GO(3%)/Pt(3.8%), achieving a hydrogen generation rate of 12.72 ± 0.27 mmol h^{-1} g^{-1}. Hence, promising results in the use of crude glycerol as feedstock for hydrogen production were obtained compared to previous works (Skaf *et al*., 2012). Nevertheless, it can be also concluded that impurities present in crude glycerol from biodiesel production are key factors in developing a realistic hydrogen production process. A filtration pretreatment of crude glycerol could enhance the photocatalytic hydrogen production due to the reduction of turbidity.

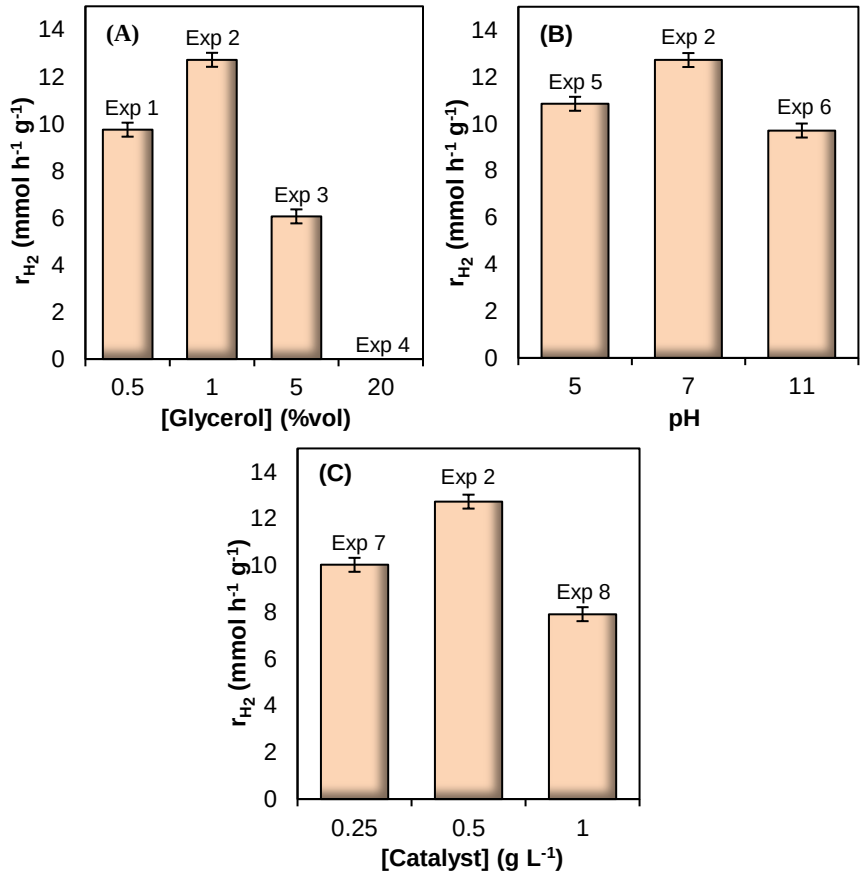

Figure 5.7 Effect of the glycerol initial concentration (%vol) (A), pH (B) and catalyst concentration (g L^{-1}) (C) on hydrogen production rate using crude glycerol solutions.

The hydrogen production rate with the ternary catalyst was compared to other TiO_2-based catalysts under optimal conditions and moreover, water and glycerol photolysis were assessed (Figure 5.8). Photolysis of water and crude glycerol was not noticed however, a production rate of 4.48 ± 0.43 mmol h^{-1} g^{-1} with synthetic glycerol was attained. Moreover, the photocatalytic run using water and the TiO_2/GO(3%)/Pt(3.8%) catalyst under the optimal conditions was developed without any appreciable production of hydrogen. Bare TiO_2 did not exhibit photocatalytic activity

using crude glycerol nevertheless, it produced 6.44 ± 0.37 mmol h^{-1} g^{-1} of hydrogen using synthetic glycerol. Similarly, TiO_2/GO(3%) catalyst showed photocatalytic activity with synthetic glycerol but not with crude glycerol. However, the addition of GO to TiO_2 did not improve the photocatalytic performance compared to TiO_2. In the case of TiO_2 doped with platinum nanoparticles, an enhancement of 9.21 ± 0.44 fold respect to bare TiO_2 was achieved for synthetic glycerol. It is important to remark the fact that the addition of 2 wt% and 3 wt% of GO (Figure 5.6-D) to TiO_2/Pt(3.8%) improved its photocatalytic activity but the addition of 1 wt% or 5 wt% of GO did not. This fact highlights the relevance of finding the adequate and optimum GO loading in ternary composites to improve the performance of photocatalytic hydrogen generation. TiO_2/Pt(3.8%) reached 11.63 ± 0.37 mmol h^{-1} g^{-1} of hydrogen using crude glycerol while TiO_2 did not show any activity. Finally, it can be observed that the ternary composites also improve the generation rate regardless of the origin of glycerol compared to both bare TiO_2 and TiO_2/Pt(3.8%). However, in the case of crude glycerol the improvement obtained with ternary catalysts compared to TiO_2/Pt(3.8%) is lower (9.37% ± 0.23) than in the case of synthetic solutions (19.34% ± 0.17). The enhanced activity of the ternary catalyst could be attributed to the synergistic effect among Pt, TiO_2 and GO, which could promote the transitive property of electrons so as to extremely inhibit the recombination of photoinduced electron-hole pairs (Wang *et al*. 2017).

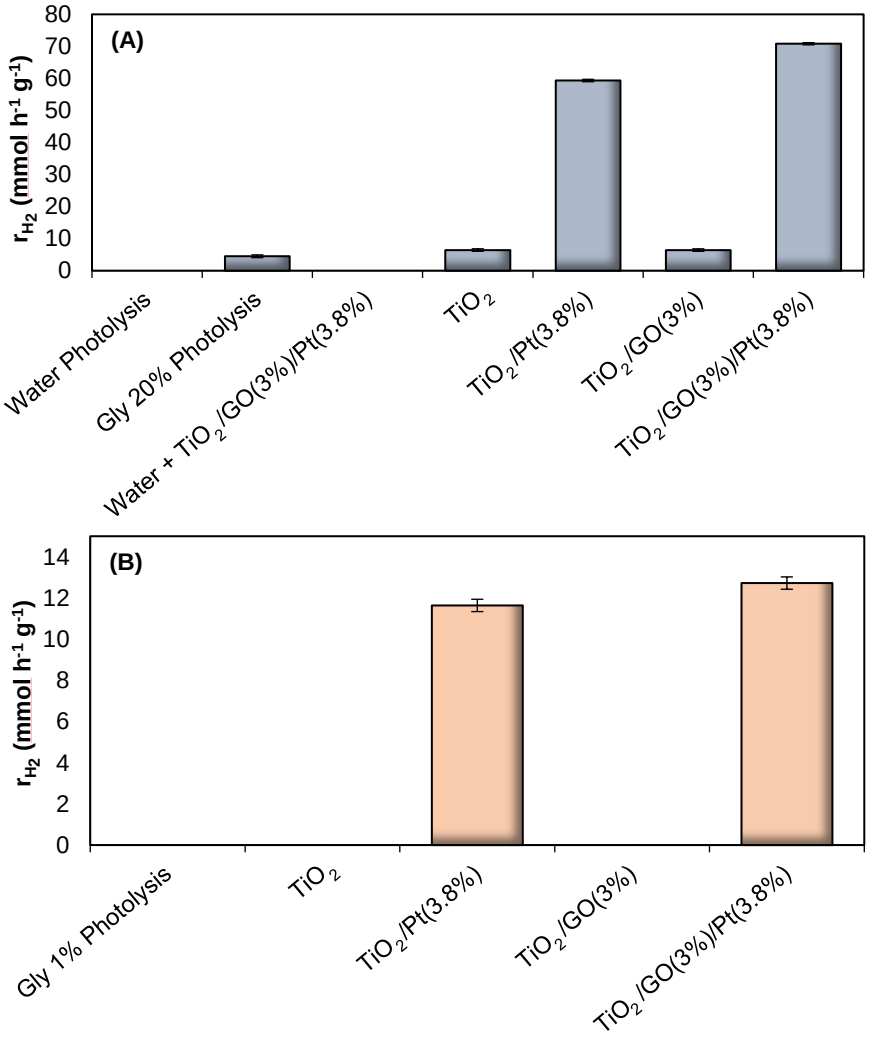

Figure 5.8 Comparison between different TiO_2-based catalyst using synthetic glycerol (A) and crude glycerol (B) under optimal conditions selected for each sacrificial agent.

Figure 5.9 shows the generated gas composition using synthetic (A) and crude (B) glycerol. Hydrogen concentration was about 82% and carbon monoxide was about 15% regardless of the origin of glycerol, indicating a similar degradation pathway.

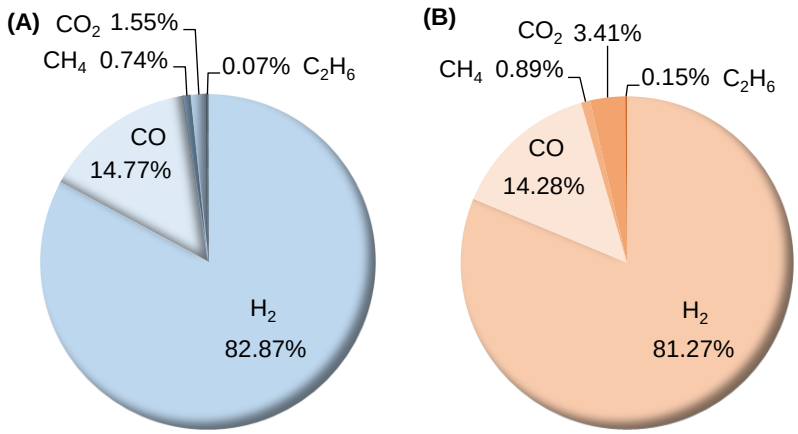

Figure 5.9 Gas composition using synthetic (A) and crude glycerol (B) under optimal conditions selected for each sacrificial agent.

5.2.2. Visible light as energy source

TiO_2-based catalysts (TiO_2, TiO_2/GO(3%), TiO_2/Pt(3.8%) and TiO_2/GO(3%)/Pt(3.8%)) were tested under visible light after optimization of operating parameters using synthetic and crude glycerol solutions. As expected, with TiO_2 and TiO_2/Pt(3.8%) no production of hydrogen from synthetic glycerol was observed since they are not activated under visible light. However, TiO_2/GO(3%) catalyst, despite being suitable for working under visible light, based on bad gap measurements, did not produce hydrogen either. Only the ternary catalyst showed photocatalytic activity, obtaining a hydrogen generation rate of 3.28 ± 0.58 mmol h^{-1} g^{-1}, 95.37% lower than under UV-vis light (Figure 5.10). These values are still higher than those obtained in the available literature using solar simulators and TiO_2-based catalysts (Table 5.4). Therefore, despite the ternary catalyst reinforces the positive characteristics of the two dopants (Pt and GO), further efforts have to be invested on synthetizing active photocatalysts under visible light. Moreover, the ternary composites synthetized in this work did not show an appreciable hydrogen production when crude

glycerol was employed as feedstock. Hence, further research is required in the development of the photocatalytic technology applied to hydrogen production using solar light as primary energy source and real by-products as feedstock.

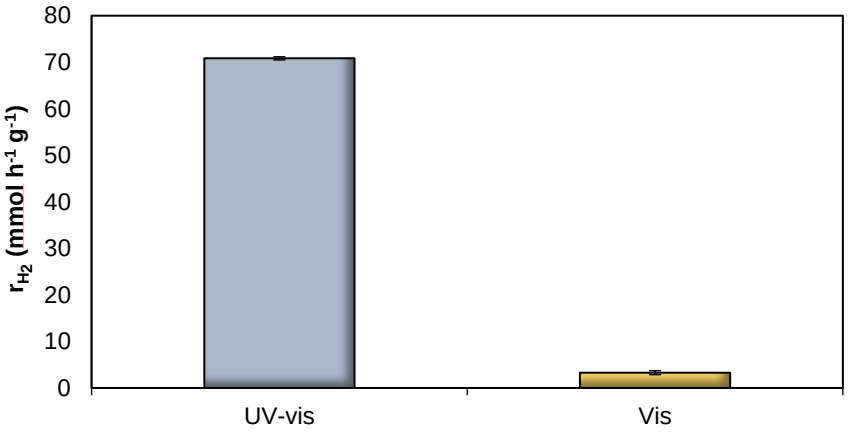

Figure 5.10 Hydrogen production rate from synthetic glycerol using TiO_2/GO(3%)/Pt(3.8%) catalyst under the optimal conditions under UV-vis and visible light. [Glycerol] = 20 vol%, pH 7, [catalyst] = 0.25 g L^{-1} and 30 ºC.

5.2.3. Liquid phase composition

The glycerol degradation was assessed over TiO_2-based photocatalysts using synthetic glycerol (Figure 5.11-A) and crude glycerol (Figure 5.11-B) in order to elucidate the photocatalysts behavior depending on glycerol origin. Regarding synthetic glycerol solutions, 5.1, 11.1, 5.8 and 19.6% of degradation was achieved after three hours of treatment using TiO_2, TiO_2/Pt(3.8%), TiO_2/GO(3%) and TiO_2/GO(3%)/Pt(3.8%), respectively. Therefore, these photocatalysts behaved in a similar way with regard to their activity towards hydrogen production (Figure 5.8-A).

In the case of crude glycerol, the TiO_2/Pt(3.8%) photocatalyst achieved a degradation of 9.1% of glycerol, slightly lower than in the case of

synthetic glycerol. The TiO_2/GO(3%)/Pt(3.8%) photocatalyst removed 11.7% of the initial crude glycerol. Hence, the degradation degree enhancement attained using the ternary catalyst compared to TiO_2/Pt(3.8%) is lower (22.2%) than in the case of synthetic solutions (43.3%), as there was already observed during the hydrogen generation experiments (Figure 5.8-B).

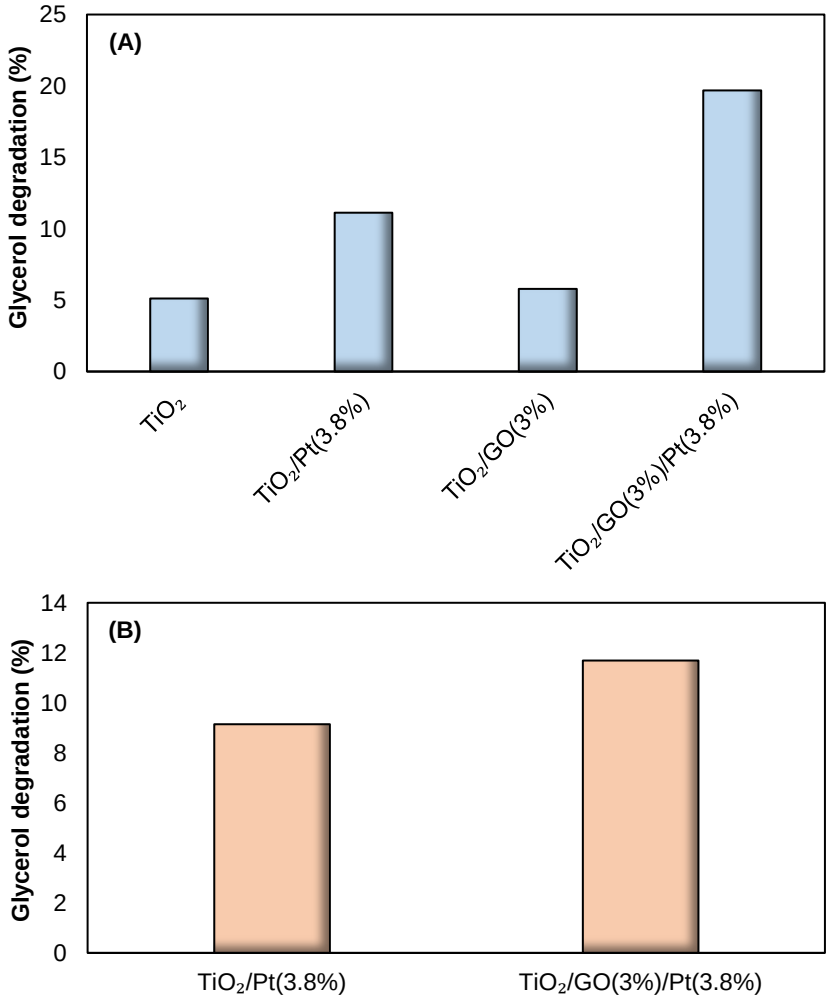

Figure 5.11 Comparison of glycerol degradation using different TiO_2-based catalyst using synthetic glycerol (A) and crude glycerol (B) under optimal conditions selected for each sacrificial agent after three hours of irradiation time.

The remaining glycerol in the liquid phase was also determined using the ternary photocatalyst and synthetic glycerol under visible light (Figure 5.12). Only 0.6% of glycerol was removed after three hours of treatment. These results are in accordance with the low hydrogen generation observed when visible light was employed as energy source (Figure 5.10).

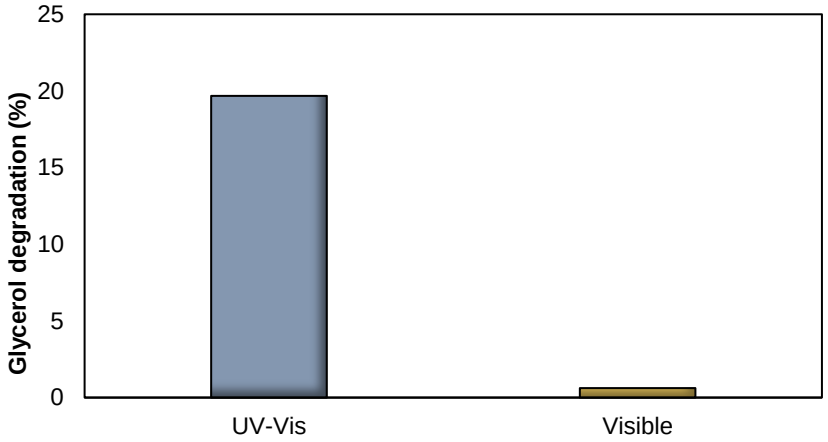

Figure 5.12 Comparison of synthetic glycerol degradation using TiO_2/GO(3%)/Pt(3.8%) catalyst under the optimal conditions and visible light as energy source. [Glycerol] = 20 vol%, pH 7, [catalyst] = 0.25 g L^{-1} and 30 ºC.

Reaction intermediates in liquid phase were analyzed in order to better understand the glycerol reaction pathway. With this aim, the presence of glyceraldehyde, hydroxyacetone, acetone, ethylene glycol, ethanol, acetic acid, methanol, formaldehyde and formic acid were studied in liquid phase. Formaldehyde was the only compound not detected either using synthetic or using crude glycerol as feedstock.

A possible photo-reforming scheme of glycerol in liquid phase is shown in Figure 5.13. The electron in the valence band is promoted to the conduction band of TiO_2, leading to a positive hole in the valence band. Glycerol degradation towards protons and reaction intermediates may proceed following ·OH-mediated and h^+_{VB}-mediated oxidation routes.

Meanwhile, electrons are transferred to GO nanosheets and/or platinum nanoparticles and, as the photo-reforming process takes place in absence of oxygen, these photogenerated electrons are available to reduce protons to H_2 molecules.

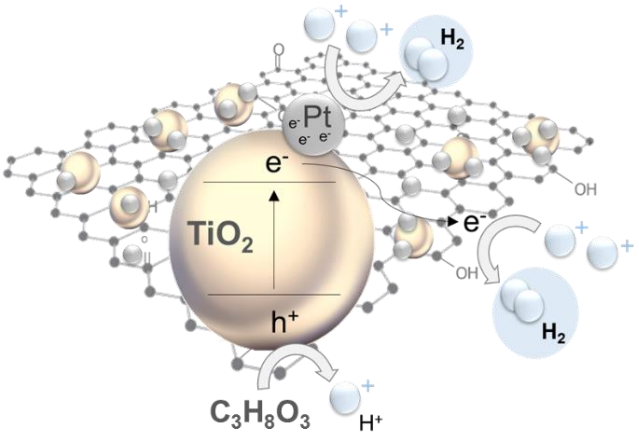

Figure 5.13 Plausible mechanistic scheme of glycerol photo-reforming over TiO_2/GO/Pt photocatalysts in absence of oxygen.

An attempt of reaction pathway for glycerol degradation and hydrogen production is shown in Figure 5.14. It has been reported that polyol molecules may scavenge more than 50% of photogenerated holes of TiO_2 and that the scavenging efficiency increases with increase of the number of the OH groups (Panagiotopoulou *et al*., 2013). In this work, it is proposed a mechanism in which glycerol undergoes dehydrogenation steps on the photocatalyst surface to yield H_2 and adsorbed intermediates, and it is followed by cleavage of C-C bonds and C-O bonds and desorption of smaller molecules.

Two initial steps can take place: (i) the dehydrogenation of glycerol to form glyceraldehyde or (ii) the dehydration of glycerol through a hydroxyacetone intermediate (King *et al*., 2010; Panagiotopoulou *et al*., 2013). In the first route, glyceraldehyde suffers a decarbonylation-

dehydrogenation sequence to produce ethylene glycol, glycoaldehyde (not analyzed) and methanol. Finally, CO and H_2 are formed through formic acid dehydrogenation coming from methanol decomposition. Moreover, parallel reactions can occur with ethylene glycol and glycoaldehyde. Ethylene glycol is dehydrated to acetaldehyde (not analyzed) and subsequently dehydrogenate to produce acetic acid. Moreover, glycoladehyde can also lead to acetic acid formation by rearrangement (Davda *et al*., 2005). In the second route, hydroxyacetone undergoes several dehydrogenation and decarbonylation steps to produce acetaldehyde and ethanol. Moreover, ethanol oxidation can also lead to the formation of acetaldehyde. However, the reverse reaction, ethanol formation from acetaldehyde by H_2 consuming, cannot be ignored (Gong *et al*., 2011). As it was remarked previously, acetaldehyde involves the subsequent production of acetic acid, which can undergo surface reactions (C-C cleavage, C-O cleavage) to form alkanes (CH_4, C_2H_6), CO_2, H_2 and H_2O (Davda *et al*., 2005; Gandarias *et al*., 2010 Pompeo *et al*., 2011; Sola *et al*., 2016).

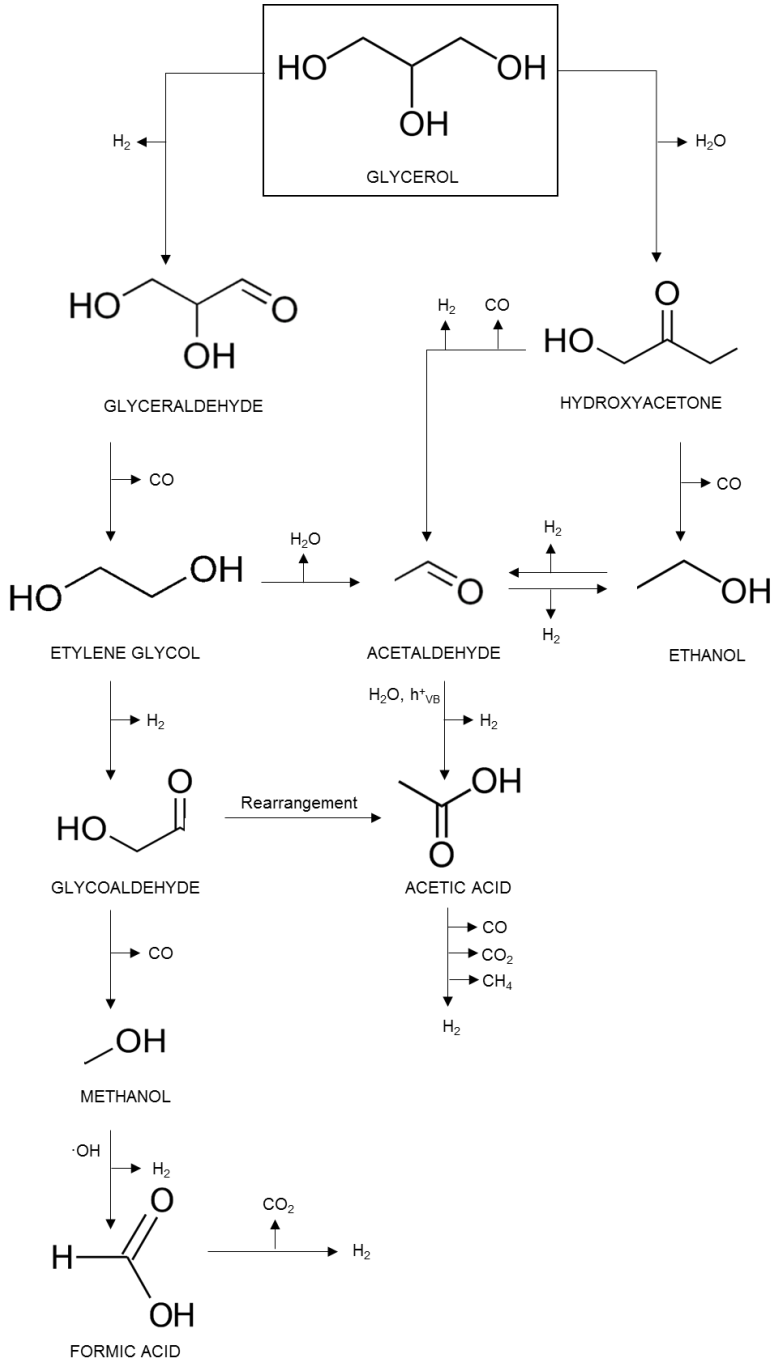

Figure 5.14 Possible reaction pathways of photo-reforming of glycerol solutions.

A detailed analysis of the liquid phase composition employing TiO_2-based photocatalysts and synthetic glycerol (Figure 5.15-A) or crude glycerol (Figure 5.15-B) was developed. Figure 5.15 shows the fraction that represents each detected compound with respect to the total compounds analyzed. The liquid phase composition was similar regardless of the TiO_2-based photocatalyst used or the glycerol origin. Hence, the degradation pathway of glycerol could be expected to be similar independently of its origin. In addition, GO nanosheets or Pt nanoparticles strongly improved the hydrogen reaction rate but not the overall reaction mechanism. It can be observed that smaller molecules, such as formic acid, methanol, acetic acid and ethanol represent a higher fraction than 60% of the total detected compounds independently of the glycerol origin or photocatalyst used. This fact is in good agreement with the proposed mechanism based on glycerol degradation on the photocatalyst surface to yield H_2 and adsorbed intermediates, and the subsequent desorption of smaller molecules.

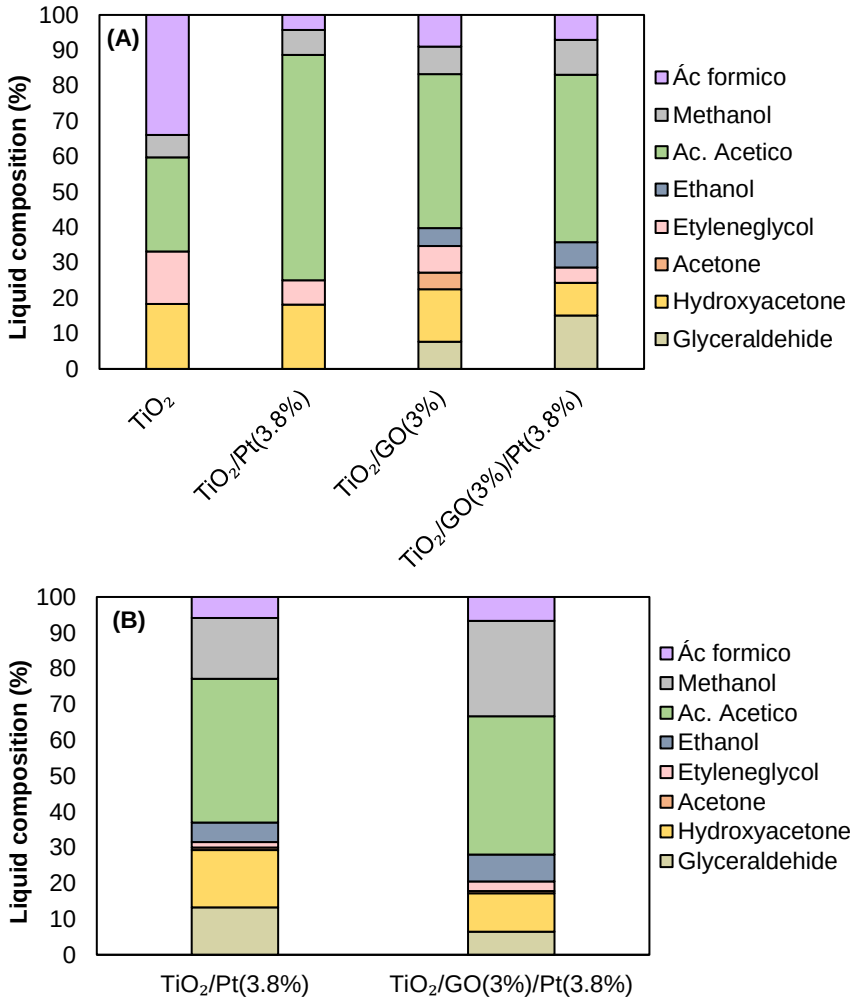

Figure 5.15 Comparison between liquid phase composition using different TiO_2-based catalysts and synthetic glycerol (A) or crude glycerol (B) under optimal conditions selected for each sacrificial agent.

Figure 5.16 shows the liquid phase composition when using UV-vis light or visible light as energy source. Since under visible light low hydrogen production and glycerol degradation were achieved, short chain final intermediates (ethanol, methanol and carboxylic acids) represented the 52.7% of the total organic compounds detected, meanwhile these intermediates reached up to 71.3% of representation using UV-vis light.

Therefore, under visible light, the final steps of glycerol degradation pathway are more difficult to reach.

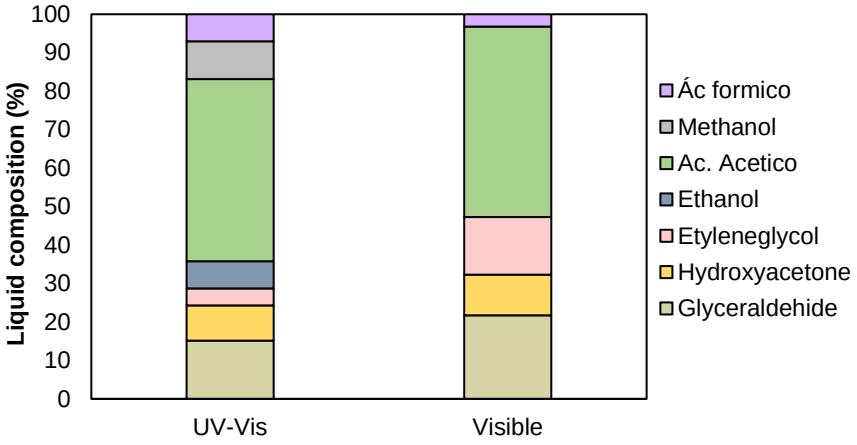

Figure 5.16 Comparison between liquid phase composition using synthetic glycerol and crude glycerol under optimal conditions selected for each sacrificial agent.

5.3. Final remarks

In this chapter, the effect of six parameters (vol% of glycerol, pH, catalyst loading, wt% of GO, wt% of Pt and temperature) on the photocatalytic hydrogen generation rate, using synthetic and crude glycerol solutions as sacrificial agent and TiO_2/GO(x)/Pt(y) as catalyst, has been studied under UV-vis light. The conditions for the maximum hydrogen generation rate of 70.83 ± 0.43 mmol h^{-1} g^{-1} are 20 vol% of synthetic glycerol, pH 7, 0.25 g L^{-1} of TiO_2/GO(3%)/Pt(3.8%) and 30 ºC.

On the other hand, in order to attempt to integrate a real by-product as feedstock for hydrogen production, crude glycerol from a biodiesel production plant was tested using optimized TiO_2/GO(3%)/Pt(3.8%) photocatalyts. Moreover, with the aim to compare the hydrogen production process from synthetic and crude glycerol, three key parameters (vol% of

glycerol, pH and catalyst loading) were analyzed. Several differences were found for optimal conditions and hydrogen production rates depending on the glycerol origin. Crude glycerol solutions photo-reforming reached up to 12.72 ± 0.27 mmol h^{-1} g^{-1} (82.04% less than synthetic glycerol) employing 1 vol% of glycerol, pH 7 and 0.5 g L^{-1} of TiO_2/GO(3%)/Pt(3.8%).

The comparison of several TiO_2-based catalysts was also carried out, observing that ternary composites improved the hydrogen generation rate regardless of the origin of glycerol compared to bare TiO_2, TiO_2/GO(3%) and TiO_2/Pt(3.8%). This fact could be attributed to the synergetic effect among TiO_2, GO and Pt which could promote the inhibition of the recombination of photoinduced electron-hole pairs.

Finally, although the hydrogen production rate achieved under visible light using the ternary catalyst and synthetic glycerol solutions is still higher than those obtained in the available literature using solar simulators and TiO_2-based catalysts, ternary catalysts did not present significant photocatalytic activity using crude glycerol as feedstock.

It can be concluded that the impurities present in crude glycerol from the biodiesel production plant are key factors in developing realistic hydrogen production process. Since turbidity was proved to be a limiting property for photocatalytic hydrogen production from crude glycerol, a filtering pretreatment could lead to an improvement in the photocatalytic process. Moreover, despite the ternary catalyst reinforces the positive characteristics of Pt and GO, further efforts have to be invested on the development of active photocatalysts under visible light.

5.4. References

Beltran, A., Romero-Ocaña, I., Delgado Jaen, J.J., Montini, T., Fornasiero, P. (2016) Photocatalytic valorization of ethanol and glycerol over TiO_2 polymorphs for sustainable hydrogen production. Applied Catalysis A: General 518:167-175.

Chen, W.T., Chan, A., Al-Azri, Z.H.N., Dosado, A.G., Nadeem, N.A., Sun-Waterhouse, D., Idriss, H., Waterhouse, G.I.N. (2015) Effect of TiO_2 polymorph and alcohol sacrificial agent on the activity of Au/TiO_2 photocatalysts for H_2 production in alcohol-water mixtures. Journal of Catalysis 329:499-513.

Clarizia, L., Di Somma, I., Onotri, L., Andreozzi, R., Marotta, R. (2017) Kinetic modeling of hydrogen generation over nano-Cu(s)/TiO_2 catalyst through photoreforming of alcohols. Catalysis Today 281:117-123.

Clarizia, L., Spasiano, D., Di Somma, I., Marotta, R., Andreozzi, R., Dionysiou, D.D. (2014) Copper modified TiO_2 catalysts for hydrogen generation through photoreforming of organics. A short review. International Journal of Hydrogen Energy 39:16812-16831.

Daskalaki, V.M., Kondarides, D.I. (2009) Efficient production of hydrogen by photo-induced reforming of glycerol at ambient conditions. Catalysis Today 144:75-80.

Davda, R.R., Shabaker, J.W., Huber, G.W., Cortright, R.D., Dumesic, J.A. (2005) A review of catalytic issues and process conditions for renewable hydrogen and alkanes by aqueous-phase reforming of oxygenated hydrocarbons over supported metal catalysts. Applied Catalysis B: Environmental 56:171-186.

Estahbanati, M.R.K., Feilizadeh, M., Iliuta, M.C. (2017) Photocatalytic valorization of glycerol to hydrogen: Optimization of operating parameters by artificial neural network. Applied Catalysis B: Environmental 209:483-492.

Flach, B., Lieberz, S., Rossetii, A. (2017) EU-28 Biofuels annual report 2017. GAIN report number: NL7015. USDA Foreign Agricultural Service.

Gandarias, I., Arias, P.L., Requies, J., Güemez, M.B., Fierro, J.L.G. (2010) Hydrogenolysis of glycerol to propanediols over a Pt/ASA catalyst: the role of acid and metal sites on product selectivity and the reaction mechanism. Applied Catalysis B: Environmental 97:248-256.

Gong, D., Subramaniam V.P., Highfield, J.G., Tang, Y., Lai, Y., Chen Z. (2011) In situ mechanistic investigation at the liquid/solid interface by attenuated total reflectance FTIR: ethanol photo-oxidation over pristine and platinized TiO_2 (P25). ACS Catalysis 1:864-871.

Hsieh, S.H., Chen, W.J., Wu, C.T. (2015) Pt-TiO_2/graphene photocatalysts for degradation of AO7 dye under visible light. Applied Surface Science 340:9-17.

King, D.L., Zhang, L., Xia, G., Karim, A.M., Heldebrant, D.J., Wang, X., Peterson, T., Wang, Y. (2010) Aqueous phase reforming of glycerol for hydrogen production over Pt-Re supported on carbon. Applied catalysis B: Environmental 99:206-213.

Kondarides, D.I., Daskalaki, V.M., Patsoura, A., Xenophon E.V. (2008) Hydrogen production by photo-induced reforming of biomass components and derivatives at ambient conditions. Catalysis Letters 122:26-32.

Kumar, D.P., Kumari, V.D., Karthik, R., Sathish, R., Shankar, M.V. (2017) Shape dependence structural, optical and photocatalytic properties of TiO_2 nanocrystals for enhanced hydrogen production via glycerol reforming. Solar Energy Materials & Solar Cells 163:113-119.

Li, M., Li, Y., Peng, S., Lu, G., Li, S. (2009) Photocatalytic hydrogen generation using glycerol wastewater over Pt/TiO_2. Frontiers of Chemistry in China 4(1):32-38.

López, C.R., Melián, E.P., Méndez, J.A.O., Santiago, D.E., Rodriguez, J.M.D., Díaz, O.G.(2015) Comparative study of alcohols as sacrificial agents in H_2 production by heterogeneous photocatalysis using Pt/TiO_2 catalysts. Journal of Photochemistry and Photobiology A: Chemistry 312:45-54.

Lv, R., Wang, X., Lv, W., Xu, Y., Ge, Y., He, H., Li, G., Wu, X., Li, X., Li, Q. (2014) Facile synthesis of ZnO nanorods grown on graphene sheets and its enhanced photocatalytic efficiency. Journal of Chemical Technology and Biotechnology 90: 550-558.

Lyubina, T.P., Markovskaya, D.V., Kozlova, E.A., Parmon, V.N. (2013) Photocatalytic hydrogen evolution from aqueous solutions of glycerol under visible light irradiation. International Journal of Hydrogen Energy 38:14172-14179.

Melian, E.P., López, C.R., Santiago, D.E., Quesada-Cabrera, R., Méndez, J.A.O., Rodriguez, J.M.D., Diaz, O.G. (2016) Study of the photocatalytic activity of Pt-modified commercial TiO_2 for hydrogen production in the presence of common organic sacrificial agents. Applied Catalysis A: General 518:189-197.

Pai, M.R., Banerjee, A.M., Rawool, S.A., Singhal A., Nayak, C., Ehrman, S.H., Tripathi A.K., Bharadwaj, S.R. (2016) A comprehensive study on sunlight driven photocatalytic hydrogen generation using low cost nanocrystalline Cu-Ti oxides Solar Energy Materials & Solar Cells 154:104-120.

Panagiotopoulou, P., Karamerou, E.E., Kondarides, D.I. (2013) Kinetics and mechanism of glycerol photo-oxidation and photo-reforming reaction in aqueous TiO_2 and Pt/TiO_2 suspensions. Catalysis Today 209:91-98.

Peng, S., Ding, M., Yi, T., Zhan, Z., Li, Y. (2015) Photocatalytic hydrogen evolution and decomposition of glycerol over $Cd_{0.5}Zn_{0.5}S$ solid

solution under visible light irradiation. Environmental Progress & Sustainable Energy 35:141-148.

Pompeo, F., Santori, G.F., Nichio, N.N. (2011) Hydrogen production by glycerol steam reforming with Pt/SiO_2 and Ni/SiO_2 catalyst. Catalysis Today 172:183-188.

Reddy, P.A.K., Manvitha, C., Reddy, P.V.L., Kim, K.H., Kumari, V. D. (2017) Enhanced hydrogen production activity over $BiOx\text{-}TiO_2$ under solar irradiation: Improved charge transfer through bismuth. Journal of Energy Chemistry 26:390-397.

Seadira, T.W.P., Sadanandam, G., Ntho, T., Masuku, C.M., Scurrell, M.S. (2018) Preparation and characterization of metals supported on nanostructured TiO_2 hollow spheres for production of hydrogen via photocatalytic reforming of glycerol. Applied Catalysis B: Environmental 222:133-145.

Skaf, D.W., Natrin, N.G., Brodwater, K.C., Bongo, C.R. (2012) Comparison of Photocatalytic Hydrogen Production from Glycerol and Crude Glycerol Obtained from Biodiesel processing. Catalysis Letters 142:1175-1179.

Sola, A.C., Homs, N., Ramirez de la Piscina, P. (2016) Photocatalytic H_2 production from $ethanol_{(aq)}$ solutions: The effect of intermediate products. International Journal of Hydrogen Energy 41:19629-19636.

Stelmachowski, M., Marchwicka, M., Grabowska, E., Diak, M., Zaleska, A. (2014) The Photocatalytic Conversion of (Biodiesel Derived) Glycerol to Hydrogen - A Short Review and Preliminary Experimental Results Part 1: A Review. Journal of Advanced Technologies 17:167-178.

Wang, C., Cai, X., Chen, Y., Cheng, Z., Luo, X., Mo, S., Jia, L., Lin, P., Yang, Z. (2017) Improved hydrogen production from glycerol photoreforming over sol-gel derived TiO_2 coupled with metal oxides. Chemical Engineering Journal 317:522-532.

Wang, P., Zhan, S., Xia, Y., Ma, S., Zhou, Q., Li, Y. (2017) The fundamental role and mechanism of reduced graphene oxide in rGO/Pt-TiO_2 nanocomposite for high-performance photocatalytic water splitting. Applied Catalysis B: Environmental 207:335-346.

Yu, J., Hai, Y., Jaroniec, M. (2011) Photocatalytic hydrogen production over CuO-modified titania. Journal of Colloid and Interface Science 357:223-228.

CHAPTER 6

CONCLUSIONS

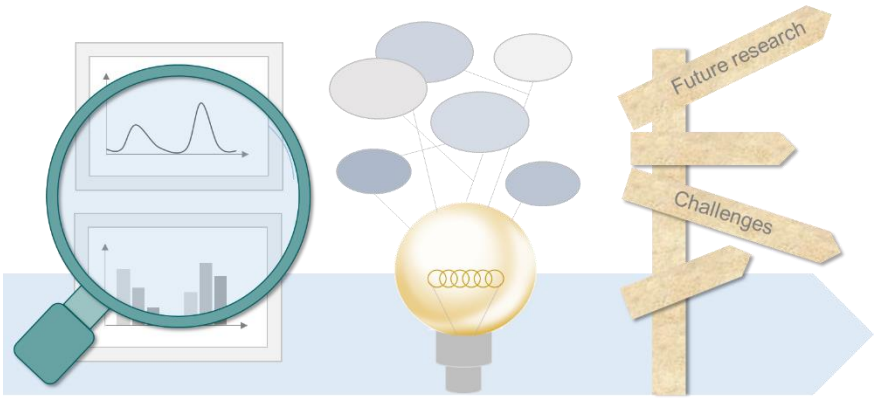

6.1. Conclusions

This thesis contributes to the knowledge on the design and application of TiO_2-based photocatalysts for the removal of organic pollutants from water and for the production of hydrogen from renewable sources.

The main conclusions derived from this work are:

Regarding the role of GO in TiO_2/GO photocatalysts

- Novel photocatalysts were synthesized and characterized by varying the TiO_2/GO weight ratio in the range of 1% to 10% and following three different preparation methods, hydrothermal, solvothermal and mechanical, to obtain an optimized TiO_2/GO photocatalyst.
- The performance of the TiO_2/GO photocatalysts was assessed based on the degradation of DCA, a disinfection by-product, which revealed an improved degradation rate for the new composites compared with bare TiO_2.
- The TiO_2 photocatalyst doped with 5 wt% of GO provided the best photocatalytic activity among all synthesized composites, with a degradation yield of 87.1% after eight hours of treatment and a degradation rate 2.6 times higher than bare TiO_2.
- The results for DCA degradation showed a coupled influence of the photocatalyst preparation method and composition.
- Novel optimized photocatalyst represents a successful alternative for DCA degradation due to the ability of GO sheets to avoid electron-hole recombination and to extend the excitation wavelength to visible range of solar spectrum.
- The photocatalysts were successfully recovered and reused without a significant loss of activity.

Considering the role of noble metals as TiO_2 co-catalysts

- Photocatalysts of TiO_2 doped with Ag or Pt nanoparticles via polyol process and photocatalysts of TiO_2 doped with these noble metals and GO nanosheets were successfully synthesized and characterized, varying the noble metal loading.
- The performance of the synthesized photocatalysts was assessed against the degradation of DCA, revealing an improved degradation rate for the new photocatalysts compared with bare TiO_2.
- TiO_2/Pt 0.5 wt% photocatalysts showed the highest photoactivity among the other catalysts, achieving total degradation and mineralization after seven hours of treatment. The larger Schottky barrier formed with Pt nanoparticles than that formed with Ag, allows the effective transfer of photogenerated charges preventing electron-hole recombination.
- The presence of GO in ternary photocatalysts does not always improve the photocatalytic process compared to binary composites, probably due to the use of non-optimized GO loading.
- The recoverability and reusability were verified, and the photocatalysts did not show a significant loss of activity.
- The contribution of different ROS to the oxidation kinetics of DCA using TiO_2 and noble metal-doped TiO_2 catalysts was evaluated.
- In the case of the TiO_2, $\cdot OH_{free}$ radicals played the most important role in DCA degradation kinetics.
- DCA degradation in the presence of TiO_2/Pt and TiO_2/Ag was mainly due to the activity of $\cdot OH_{free}$ radicals from the transformation of $O_2^{\cdot-}$ and, to a lesser extent, $\cdot OH_{ads}$ radicals. A higher contribution of $\cdot OH_{free}$ radicals from $O_2^{\cdot-}$ was observed with TiO_2/Pt (78.2% ± 0.5) than with TiO_2/Ag (64.9% ± 3.6).

Photocatalytic hydrogen generation from a renewable source

- Photocatalysts based on TiO_2/GO(x)/Pt(y) (x=0-5 wt% and y=0-3.8 wt%) were tested during photocatalytic hydrogen generation using synthetic and crude glycerol solutions as sacrificial agents under UV and visible light.
- The optimal conditions were 20 vol% of synthetic glycerol, pH 7, [TiO_2/GO(3%)/Pt(3.8%)]=0.25 g L^{-1} and 30 ºC, achieving a hydrogen generation rate of 70.83 ± 0.43 mmol h^{-1} g^{-1}.
- Crude glycerol from a biodiesel production plant was tested using optimized TiO_2/GO(3%)/Pt(3.8%) photocatalyts, reaching up to 12.72 ± 0.27 mmol h^{-1} g^{-1} employing optimal conditions of 1 vol% of crude glycerol, pH 7 and 0.5 g L^{-1} of catalyst .
- Several differences were found for optimal conditions and hydrogen production rates depending on the glycerol origin.
- Optimized ternary photocatalysts improved the hydrogen generation rate regardless of the origin of glycerol compared to bare TiO_2, TiO_2/GO(3%) and TiO_2/Pt(3.8%). This fact could be attributed to the synergetic effect among TiO_2, GO and Pt which could promote the inhibition of the recombination of photoinduced electron-hole pairs.
- The relevance of finding the adequate GO loading in ternary composites to improve the photocatalytic performance was highlighted.
- Promising results in hydrogen generation using optimized ternary photocatalysts and synthetic glycerol solutions under visible light were attained, but no significant photocatalytic activity was observed using crude glycerol as feedstock under visible light.
- Impurities present in crude glycerol from biodiesel production plant are a key factor in developing realistic hydrogen production process. Moreover, further efforts have to be invested on active photocatalysts under visible light.

6.2. Challenges for future research

This thesis aims to contribute to the development of TiO_2-based photocatalysts for the removal of organic pollutants from water and for the production of hydrogen from renewable sources. However, despite the achievements already described, there are still some challenges ahead that must be overcome to improve the present research:

- Design high activity-photocatalysts capable of using solar light as energy source.
- Development of a mathematical model that allows to predict the properties of the novel photocatalysts and their interaction with the reaction medium.
- Support the photocatalyst to facilitate its reuse and scaling up of the photocatalysis process or integrate the reaction step with suitable membranes to recover the catalyst.
- Design of an optimal photoreactor that allows working with real effluents under visible light.

6.3. Conclusiones

Esta tesis se centra en el diseño de nuevos fotocatalizadores basados en TiO_2 aplicados a la eliminación de contaminación orgánica del agua y a la producción de hidrógeno a partir de fuentes renovables.

Las principales conclusiones derivadas de este trabajo son:

Respecto al papel del GO en fotocatalizadores de TiO_2/GO

- Se sintetizaron y caracterizaron nuevos fotocatalizadores variando la relación en peso de TiO_2/GO en el rango de 1% a 10% y siguiendo tres métodos diferentes de preparación, hidrotermal, solvotermal y mecánico, con el objetivo de obtener un fotocatalizador de TiO_2/GO optimizado.
- El rendimiento de los fotocatalizadores se evaluó a través de la degradación de DCA, un subproducto de desinfección, que reveló una tasa de degradación mejorada para los nuevos materiales compuestos en comparación con el TiO_2 comercial.
- El fotocatalizador de TiO_2 dopado con un 5% en peso de GO y sintetizado mediante el método hidrotermal proporcionó la mejor actividad fotocatalítica, con un rendimiento de degradación del 87.1% tras ocho horas de tratamiento lo que supone una tasa de degradación 2.6 veces mayor que la del TiO_2 comercial.
- Los resultados de degradación de DCA mostraron una influencia acoplada del método de preparación y la composición del fotocatalizador.
- El fotocatalizador optimizado de TiO_2/GO representa una gran alternativa para la degradación de DCA debido a la capacidad de las láminas GO para evitar la recombinación de los pares electrón-hueco y extender el rango de excitación del catalizador hacia el rango visible del espectro solar.
- Los fotocatalizadores fueron recuperados y reutilizados sin una pérdida significativa de actividad.

Respecto al papel de los metales nobles como co-catalizadores del TiO_2

- Se sintetizaron y caracterizaron fotocatalizadores de TiO_2 dopado con nanoparticulas de plata o platino y fotocatalizadores de TiO_2 dopado con estos metales nobles y láminas de GO, variando la carga de los metales nobles.
- El rendimiento de los fotocatalizadores sintetizados se evaluó frente a la degradación de DCA, revelando una tasa de degradación mejorada para los nuevos fotocatalizadores en comparación con el TiO_2 desnudo.
- Los fotocatalizadores de TiO_2/Pt con un 0,5% en peso de platino presentaron la mayor actividad fotocatalítica, alcanzando una degradación y mineralización del 100% tras siete horas de tratamiento. Esto se debe a que la barrera de Schottky formada por el acoplamiento de nanoparticulas de platino es mayor a la que forma el acoplamiento de nanoparticulas de plata, lo que permite una mayor transferencia de cargas fotogeneradas evitando la recombinación de los pares electrón-hueco.
- La presencia de GO en fotocatalizadores ternarios no siempre mejora el proceso fotocatalítico en comparación con los compuestos binarios, esto es probablemente debido al uso de una carga de láminas de GO no optimizada.
- Se verificó la capacidad de recuperación y reutilización de los fotocatalizadores sin pérdida significativa de actividad.
- Se estudió la contribución de diferentes ROS a la cinética de oxidación del DCA usando TiO_2 y catalizadores de TiO_2 dopados con plata y platino.
- En el caso del TiO_2, los radicales $\cdot OH_{libres}$ desempeñaron el papel más importante en la cinética de degradación del DCA.
- La degradación de DCA en presencia de TiO_2/Pt y TiO_2/Ag se debió principalmente a la actividad de los radicales $\cdot OH_{libres}$

procedented de la transformación de radicales $O_2^{\cdot-}$ y, en menor medida, radicales $\cdot OH_{ads}$. Se observó una mayor contribución de radicales $\cdot OH_{libres}$ procedentes de $O_2^{\cdot-}$ con TiO_2/Pt (78,2% ± 0,5) que con TiO_2/Ag (64,9% ± 3,6).

Producción fotocatalítica de hidrógeno a partir de fuentes renovables

- Se emplearon fotocatalizadores basados en TiO_2/GO(x)/Pt(y) (x=0-5 wt% e y=0-3,8 wt%) en la generación fotocatalítica de hidrógeno empleando glicerol sintético y crudo como agentes de sacrificio bajo luz UV y visible.
- Las condiciones óptimas de operación fueron 20 %vol de glicerol sintético, pH 7, [TiO_2/GO(3%)/Pt(3.8%)]=0.25 g L^{-1} y 30 ºC, alcanzando una tasa de generación de hidrógeno de 70.83 ± 0.43 mmol h^{-1} g^{-1}.
- Se empleó glicerol crudo procedente de una planta de producción de biodiesel y el fotocatalizador optimizado TiO_2/GO(3%)/Pt(3.8%) alcanzando un producción de 12.72 ± 0.27 mmol h^{-1} g^{-1} empleando condiciones óptimas de 1 vol% de glicerol crudo, pH 7 y 0.5 g L^{-1} de catalizador.
- Se encontraron varias diferencias para las condiciones óptimas y las tasas de producción de hidrógeno dependiendo de la naturaleza del glicerol.
- Los fotocatalizadores ternarios optimizados mejoraron la tasa de generación de hidrógeno independientemente de la naturaleza del glicerol en comparación con el TiO_2 comercial, TiO_2/GO(3%) y TiO_2/Pt(3,8%). Este hecho podría atribuirse al efecto sinérgico entre el TiO_2, el GO y el platino promoviendo la inhibición de la recombinación de los pares de electrón-agujero fotogenerados.
- Optimizar la cantidad de GO en los materiales compuestos ternarios es un factor clave para mejorar el rendimiento fotocatalítico de los mismos.

- Se obtuvieron resultados prometedores en la generación de hidrógeno utilizando fotocatalizadores ternarios optimizados y soluciones de glicerol sintético bajo luz visible, pero no se observó actividad fotocatalítica significativa usando glicerol bruto como agente de sacrificio bajo luz visible.
- Las impurezas presentes en el glicerol crudo de la planta de producción de biodiesel son un factor clave en el desarrollo de un proceso de producción de hidrógeno realista. Además, es necesario el estudio y desarrollo de nuevos fotocatalizadores activos bajo luz visible.

6.4. Retos futuros

El objetivo de esta tesis es contribuir al desarrollo de fotocatalizadores basados en TiO_2 para la eliminación de contaminantes orgánicos del agua y para la producción de hidrógeno a partir de fuentes renovables. Sin embargo, a pesar de los logros ya descritos, aún quedan por delante nuevos desafíos que deben superarse para mejorar la presente investigación:

- Diseñar fotocatalizadores altamente activos capaces de utilizar luz solar como fuente de energía.
- Desarrollo de un modelo matemático que permita predecir las propiedades de los nuevos fotocatalizadores y su interacción con el medio de reacción.
- Soportar el fotocatalizador para facilitar su reutilización y el escalado del proceso de fotocatálisis o integrar la etapa de reacción con membranas para recuperar el catalizador.
- Diseño de un fotorreactor óptimo que permita trabajar con efluentes reales utilizando luz visible como fuente de energía.

ANNEXES

ANNEX I. NOMENCLATURE

AFM	Atomic force microscopy
AOPs	Advanced oxidation processes
BET	Brunauer, Emmet and Teller
BQ	Benzoquinone
CB	Conduction band
DBAA	Dibromoacetic acid
DBPs	Disinfection by-product
DCA	Dichloroacetic acid
DMSO	Dimethyl sulfoxide
DNPH	Dinitrophenylhydrazine
DOC	Dissolved organic carbon
DWD	Drinking water directive
e^-_{CB}	Conduntion band electrons
EDX	Energy dispersive X-Ray
E_G	Band gap energy
EG	Ethylene glycol
HPLC	High-performance liquid chromatography
ICP	Inductively coupled plasma mass spectrometry
FA	Formic acid
FT-IR	Fourier transform infrared
GO	Graphene oxide
HAAs	Haloacetic acids
HQ	Hydroquinone
h^+_{VB}	Valence band holes
IC	Inorganic carbon
IPPC	Intergovernmental panel on climate change
IR	Infrared
JCPDS	Joint committee on powder diffraction standards
LSPR	Localized surface plasmon resonance

MBAA	Monobromoacetic acid
MCAA	Monochloroacetic acid
NDIR	Non-dispersive infrared
NIR	Near infrared
NM	Noble metal
NOM	Natural organic matter
$O_2^{\cdot -}$	Superoxide radical
$\cdot OH_{ads}$	Adsorbed hydroxyl radicals
$\cdot OH_{free}$	Free hydroxyl radicals
PRET	Plasmon resonance energy transfer
rGO	Reduced graphene oxide
ROS	Reactive oxygen species
t-BuOH	tert-butanol
TCAA	Trichloroacetic acid
TEM	Transmission electron microscopy
TGA	Thermogravimetric analysis
TC	Total carbon
TOC	Total organic carbon
UP	Ultrapure
US EPA	United States Environmental Protection Agency
UV	Ultraviolet
UVA	Ultraviolet A
UVB	Ultraviolet B
UVC	Ultraviolet C
VB	Valence band
Vis	Visible
XRD	X-ray diffraction

ANNEX II. SCIENTIFIC PAPERS

- Related papers published prior to the present thesis

María J. Rivero, Sara Dominguez, Paula Ribao, Raquel Ibañez, Inmaculada Ortiz, Angel Irabien (2014) Kinetic Analysis and Biodegradability of the Fenton Mineralisation of Bisphenol A. Journal of Chemical Technology & Biotechnology 89(8):1228-1234. JCR impact factor 2014: 2.738, Q1, position 28 of 135 in the Chemical Engineering category.

- Related papers published during the present thesis

Sara Dominguez, Paula Ribao, María José Rivero, Inmaculada Ortiz (2015) Influence of Radiation and TiO_2 Concentration on the Hydroxyl Radicals Generation in a Photocatalytic LED Reactor. Application to dodecylbenzenesulfonate degradation. Applied Catalysis B: Environmental 178:165-169. JCR impact factor 2015: 8.328, Q1, position 3 of 135 in the Chemical Engineering category.

Paula Ribao, María José Rivero, Inmaculada Ortiz (2017) TiO_2 Structures Doped with Noble Metals and/or Graphene Oxide to Improve the Photocatalytic Degradation of Dichloroacetic Acid. Environmental Science and Pollution Research, 24:12628-12637. JCR impact factor 2017: 2.800, Q2, position 82 of 241 in the Environmental Sciences category.

Paula Ribao, María José Rivero, Inmaculada Ortiz (2017) Enhanced photocatalytic activity using GO/TiO_2 catalyst for the removal of DCA solutions. Environmental Science and Pollution Research. Doi: 10.1007/s11356-017-0901-6. Article in press. JCR impact factor 2017: 2.800, Q2, position 82 of 241 in the Environmental Sciences category.

Beatriz Gómez-Ruiz, Paula Ribao, Nazely Diban, María José Rivero, Inmaculada Ortiz, Ane Urtiaga (2018) Photocatalytic degradation and mineralization of perfluorooctanoic acid (PFOA) using a composite TiO_2-rGO catalyst. Journal of Hazardous Materials, 344:950-957. JCR impact factor 2017: 6.343, Q1, position 5 of 50 in the Environmental Engineering category and position 13 of 241 in the Environmental Sciences category.

Paula Ribao, Juan Corredor, María J. Rivero, Inmaculada Ortiz (2018) Role of reactive oxygen species on the activity of noble metal-doped TiO_2 photocatalysts. Journal of Hazardous Materials. Doi: 10.1016/j.jhazmat.2018.05.026. Article in press. JCR impact factor 2017: 6.343, Q1, position 5 of 50 in the Environmental Engineering category and position 13 of 241 in the Environmental Sciences category.

María José Rivero, Olalla Iglesias, Paula Ribao, Inmaculada Ortiz (2018) Kinetic performance of TiO_2/Pt/reduced graphene oxide composites in the photocatalytic hydrogen production. International Journal of Hydrogen Energy. Doi: 10.1016/j.ijhydene.2018.02.115. Article in press. JCR impact factor 2017: 4.229, Q1, position 24 of 97 in the Energy and Fuels category.

Paula Ribao, Alexandra M. Esteves, Vitor R. Fernandes, María J. Rivero, Carmen M. Rangel, Inmaculada Ortiz (2018). Challenges arising from the use of TiO_2/GO/Pt catalysts to produce hydrogen from crude glycerol compared to synthetic glycerol. Submitted to a Journal (Chemical Engineering Journal). JCR impact factor 2017: 6.735, Q1, position 3 of 50 in the Environmental Engineering category and position 7 of 137 in the Chemical Engineering category.

ANNEX III. CONGRESS CONTRIBUTIONS

- Related contributions prior to the present thesis

Sara Dominguez, Paula Ribao, María José Rivero, Inmaculada Ortiz. Influence of TIO_2 Concentration on the ·OH Radicals Generation. Photocatalytic Removal of Dodecylbenzenesulfonate. ANQUE-ICCE-BIOTEC 2014 Congresses on Chemistry, Chemical Engineering and Biotechnology. Madrid, Spain, 1-4 July, 2014. Poster presentation.

Paula Ribao, Sara Dominguez, Fernando Ramirez, Marina Gonzalez-Barriuso, María J. Rivero, Angel Yedra, Inmaculada Ortiz. New Catalysts Based on Nanocomposites of Graphene Oxide-TiO_2 for Photocatalytic. ANQUE-ICCE-BIOTEC 2014 Congresses on Chemistry, Chemical Engineering and Biotechnology. Madrid, Spain, 1-4 July, 2014. Poster presentation.

María J. Rivero, Sara Dominguez, Paula Ribao, Inmaculada Ortiz. Influence of Radiation on the $^{\cdot}OH$ Generation in a Photocatalytic LED Reactor. Application to removal of dodecylbenzenesulfonate. 8th European Meeting on Solar Chemistry and Photocatalysis: Environmental Applications - SPEA8. Thessaloniki, Greece, 25-28 June, 2014. Oral presentation.

- Related contributions during the present thesis

Paula Ribao, Alexandra M. Esteves, Vitor R. Fernandes, María José Rivero, Carmen M. Rangel, Inmaculada Ortiz. Exploring crude glycerol as feedstock in the development of a realistic hydrogen production process. 10th European Meeting on Solar Chemistry and Photocatalysis: Environmental Aplications (SPEA10). Almería, Spain, 4-8 June, 2018. Oral presentation

Paula Ribao, Alexandra M. Esteves, Vitor R. Fernandes, María José Rivero, Carmen M. Rangel, Inmaculada Ortiz. Photocatalytic Hydrogen Production using TiO_2-rGO-Pt Nanocomposites and Glycerol as a Sacrificial Agent. European Hydrogen Energy Conference 2018 (EHEC). Málaga, Spain, 14-16 March, 2018. Poster presentation.

Paula Ribao, Juan Corredor, Maria J. Rivero, Inmaculada Ortiz. Selecting an optimal concentration of benzoquinone for a sustainable use as superoxide radical scavenger. 3rd Iberoamerican Conference on Advance Oxidation Technologies (III CIPOA). Guatape, Colombia, 14-17 November, 2017. Poster presentation.

Beatriz Gómez-Ruiz, Paula Ribao, Nazely Diban, María José Rivero, Inmaculada Ortiz, Ane Urtiaga. Efficient photocatalytic degradation of perfluorooctanoic acid (PFOA) by TiO_2 doped with graphene oxide. 10th World Congress of Chemical Engineering. Barcelona, Spain, 1-5 October, 2017. Oral presentation.

Juan Corredor, Paula Ribao, María José Rivero, Inmaculada Ortiz. New developments on Photocatalytic Process Intensification. 10th World Congress of Chemical Engineering. Barcelona, Spain, 1-5 October, 2017. Poster presentation.

Olalla Iglesias, Paula Ribao, María José Rivero, Inmaculada Ortiz. Enhanced Photocatalytic Hydrogen Evolution over TiO_2/Graphene Oxide Catalyst. Advanced Nanomaterial (ANM2017). Aveiro, Portugal, 19-21 July, 2017. Poster presentation.

Paula Ribao, Juan Corredor, María José Rivero, Inmaculada Ortiz. The Role of Reactive Oxidative Species in the Photocatalytis Activity of modified TiO_2 Catalysts. 5th Environmental Applications of Advanced Oxidation Processes. Prague, Czech Republic, 25-29 June, 2017. Poster presentation.

Ane Urtiaga, Beatriz Gómez-Ruiz, María José Rivero, Paula Ribao, Nazely Diban, Inmaculada Ortiz. TiO_2-Graphene photocatalytic degradation of perfluorooctanoic acid (PFOA). 5th Environmental Applications of Advanced Oxidation Processes. Prague, Czech Republic, 25-29 June, 2017. Oral presentation.

Olalla Iglesias, Paula Ribao, María José Rivero, Inmaculada Ortiz. Comparative kinetic of composite photocatalysts in the production of hydrogen from methanol. 1st Fotofuel conference: current challenges in solar fuels production. Almería, Spain, 25-27 October, 2016.

Paula Ribao, María José Rivero, Inmaculada Ortiz. Advances in the investigation of photocatalytic processes in the group of advanced separation processes (University of Cantabria). IV Reunión Nacional de Grupos de Fotocatálisis. Badajoz, Spain, 22-23 September, 2016. Oral presentation.

Paula Ribao, María José Rivero, Inmaculada Ortiz. Graphene Oxide/TiO_2 Structures Doped with Noble Metals to Improve the Photocatalytic Degradation of Dichloroacetic Acid. 9th European Meeting on Solar Chemistry and Photocatalysis: Environmental Applications (SPEA9). Strasbourg, France, 13-17 June, 2016. Poster presentation.

Marina González-Barriuso, Laura Astoreca, Paula Ribao, María José Rivero, Carmen Manteca, Ángel Yedra. Synthesis of graphene oxide-TiO_2 nanocomposites for photocatalytic applications. GraphIn (Graphene Industry – Challenges & Opportunities). Zaragoza, Spain, 3 December, 2015. Poster presentation.

Paula Ribao, María José Rivero, Inmaculada Ortiz. Influence of the Synthesis Method on the Photocatalytic activity of Graphene Oxide/Titanium Dioxide Composites. Fourth European Conference on Environmental Applications (EAAOP4). Athens, Greece, 21-24 October, 2015. Oral presentation.

Paula Ribao, María José Rivero, Inmaculada Ortiz. Enhanced photocatalytic degradation of organic compounds using graphene oxide/titanium dioxide (GO/TiO_2) composites. XXXV Bienal RSEQ. A Coruña, Spain, 19-23 July, 2015. Poster presentation.

Paula Ribao, María José Rivero, Inmaculada Ortiz. Synthesis of GO/TiO_2 composite through hydrothermal method for photocatalytic application. Imaginenano 2015 (Graphene 2015). Bilbao, Spain, 10-13 March, 2015. Poster presentation.

Paula Ribao, Sara Dominguez, María José Rivero, Inmaculada Ortiz. Influence of the inoculum in the respirometric biodegradability of oxidized waters. 13th Mediterranean Congress of Chemical Engineering. Barcelona, Spain, 30 September-3 October, 2014. Poster presentation.

ABOUT THE AUTHOR

Paula Ribao Martínez was born on 11th June 1990 in Ruiloba (Cantabria, Spain). In Septembre 2013 she completed the Chemical Engineering degree at the Universidad de Cantabria, during which she obtained a collaboration research grant from the Education, Culture and Sport Ministry, allowing her to begin her research work at the Chemical and Biomolecular Engineering Department. During the 2013 - 2014 course she studied a Master Degree in Chemical Engineering “Sustainable Production and Consumption” at the University of Cantabria. Best master's degree Project awarded by Superior Technical School of Industrial and Telecommunication Engineers of the University of Cantabria was achieved in 2015.

From 2014 she has been involved in the PhD program of Chemical, Energy and Process Engineering at University of Cantabria under the supervision of Dr. Maria José Rivero Martínez and Prof. Dr. Inmaculada Ortiz Uribe in the research group “Advanced Separation Processes (ASP)”. She has received a predoctoral contract for the training of doctors and a predoctoral mobility grant for the realization of short stays from the University of Cantabria. In 2017, under the framework of her PhD studies, she carried out a research stay for three months at the *Laboratório Nacional de Energia e Geologia* (Lisbon) under the supervision of Dr. Carmen Rangel. She is the author of 8 scientific articles in indexed journals and 19 contributions to international conferences.

Increasing demand of clean water resources and the growing global energy requirements have become an issue worldwide. Therefore, sustainable technologies to meet human demands are required. Heterogeneous photocatalysis, an advanced oxidation process, arises as a successfully solution due to its ability of integrating wastewater treatment and hydrogen production.

Until now, titanium dioxide (TiO_2) is one of the most promising photocatalyst however, some drawbacks hinder its wider commercial application. Therefore, although it is highly photoreactive and cost-effective, some challenges still need to be overcome: high recombination rate of charge carriers and, absence of activity under visible light.

This thesis aims at the design of TiO_2-based photocatalysts through chemical modifications by incorporation of graphene oxide and/or noble metals in the TiO_2 structure for water pollution remediation and hydrogen production.